



### 저작자표시-비영리-변경금지 2.0 대한민국

이용자는 아래의 조건을 따르는 경우에 한하여 자유롭게

- 이 저작물을 복제, 배포, 전송, 전시, 공연 및 방송할 수 있습니다.

다음과 같은 조건을 따라야 합니다:



저작자표시. 귀하는 원 저작자를 표시하여야 합니다.



비영리. 귀하는 이 저작물을 영리 목적으로 이용할 수 없습니다.



변경금지. 귀하는 이 저작물을 개작, 변형 또는 가공할 수 없습니다.

- 귀하는, 이 저작물의 재이용이나 배포의 경우, 이 저작물에 적용된 이용허락조건을 명확하게 나타내어야 합니다.
- 저작권자로부터 별도의 허가를 받으면 이러한 조건들은 적용되지 않습니다.

저작권법에 따른 이용자의 권리와 책임은 위의 내용에 의하여 영향을 받지 않습니다.

이것은 [이용허락규약\(Legal Code\)](#)을 이해하기 쉽게 요약한 것입니다.

[Disclaimer](#)



이학박사 학위논문

Vortex Dynamics in a Highly Oblate  
Bose-Einstein Condensate: Quantum  
Turbulence and Vortex Sheding

납작한 보즈-아인슈타인 응집체에서의 양자 소용돌이 동역학:  
양자 난류와 소용돌이 방출

2016년 2월

서울대학교 대학원  
물리 · 천문 학부  
권 우 진

Vortex Dynamics in a Highly Oblate Bose-Einstein  
Condensate: Quantum Turbulence and Vortex Shedding  
납작한 보즈-아인슈타인 응집체에서의 양자 소용돌이 동역학:  
양자 난류와 소용돌이 방출

지도교수 신 용 일  
이 논문을 이학박사 학위 논문으로 제출함

2015년 11월

서울대학교 대학원

물리 · 천문 학부

권 우 진

권우진의 박사 학위 논문을 인준함

2015년 11월

위 원 장	안 경 원	(인)
부위원장	신 용 일	(인)
위 원	제 원 호	(인)
위 원	정 현 석	(인)
위 원	문 종 철	(인)

**Vortex Dynamics in a Highly Oblate  
Bose-Einstein Condensate: Quantum  
Turbulence and Vortex Shedding**

by

**Woo Jin Kwon, B.S.**

**Dissertation**

Presented to the Faculty of the Graduate School of  
Seoul National University  
in Partial Fulfillment  
of the Requirements  
for the Degree of

**Doctor of Philosophy**

**Seoul National University**

February 2016

## Abstract

# Vortex Dynamics in a Highly Oblate Bose-Einstein Condensate: Quantum Turbulence and Vortex Shedding

**Woo Jin Kwon**  
Department of Physics and Astronomy  
The Graduate School  
Seoul National University

Quantized vortices which are one of elementary excitations in a superfluid have long been investigated in Bose condensed systems. Since the first observation of a vortex in a BEC in 1998, experimental researches on vortices have continued including formation of vortices, vortex lattice dynamics and superfluid turbulence, etc. Although many issues on vortices already have been investigated due to long history of studies on vortices, there still remain many interesting problems on quantized vortices in a Bose-Einstein condensate.

Quantum turbulence (superfluid turbulence) has been one of great issues in superfluid helium systems. In particular, vortex tangle and its decay dynamics which accompany vortex reconnections are still ongoing issues. Dilute gas of Bose condensed system is a good and new platform to study them. In this thesis, highly oblate BECs have been employed to investigate two dimensional (2D) quantum turbulence, generated by a fastly moving repulsive Gaussian beam, and its decay is interpreted with vortex pair annihilation which is 2D version of vortex reconnection. Our experimental results show that relaxation of superfluid turbulence is highly dependent on thermal part of the system.

And this lead us to investigate thermal friction on vortices in finite temperature BECs. Dissipative motion of a vortex in a superfluid is described by the interaction between vortex core and thermal component. This is the famous concepts of mutual friction and we measure dimensionless coefficient of mutual friction  $\alpha$  using thermal dissipative motion of corotating two vortices.

Finally, we study the problem of vortex shedding generated by a flow past a repulsive Gaussian beam. Systematic studies have long been missed on critical velocity  $v_c$  of a BEC superfluid and we present the detailed measurement on  $v_c$  for vortex shedding by changing height  $V_0$  and radius  $\sigma$  of the Gaussian obstacle.  $v_c$  shows minimum near  $V_0 \approx \mu$ , where  $\mu$  is the chemical potential of the BEC, and monotonically increases for decreasing  $\sigma$  for fixed  $V_0$  when  $V_0 \gg \mu$ . The results can be understood qualitatively by considering the soft boundary effect of the Gaussian beam. Moreover, we investigate the characteristics of vortex shedding depending on  $V_0$  and observe that penetrable beam ( $V_0 < \mu$ ) generates vortex dipoles in a periodic way while impenetrable beam ( $V_0 > \mu$ ) is much more prone to irregular vortex shedding. Using this periodic behavior of penetrable beam, we demonstrate a deterministic generation of a single vortex dipole which will enable us to do experiments on such as vortex pair-pair collisions.

**Keywords :** Bose-Einstein condensate, superfluid, quantized vortex, quantum turbulence, vortex pair annihilation, mutual friction, vortex shedding, critical velocity.

*Student number :* 2010-20357

# Contents

<b>Abstract</b>	<b>i</b>
<b>List of Figures</b>	<b>vi</b>
<b>Chapter 1 Introduction</b>	<b>1</b>
1.1 Ultracold Bose gas and vortex physics . . . . .	1
1.2 Brief reviews on Bose-Einstein condensates . . . . .	2
1.3 Vortices in a BEC . . . . .	4
1.3.1 Quantized vortex in a BEC . . . . .	4
1.3.2 Angular momentum of a vortex . . . . .	6
1.3.3 Interaction of two vortices . . . . .	7
1.4 Outline of the thesis . . . . .	9
<b>Chapter 2 Quantum turbulence in a BEC</b>	<b>12</b>
2.1 Introduction . . . . .	12
2.1.1 Decay of a vortex in a superfluid . . . . .	14
2.2 Experimental methods . . . . .	15
2.2.1 Generating turbulence in a BEC . . . . .	15
2.2.2 Vortex number counting . . . . .	17

2.3	Relaxation of Turbulence . . . . .	19
2.3.1	Nonexponential decay . . . . .	19
2.3.2	Vortex pair annihilation . . . . .	23
2.3.3	Decay rate measurements . . . . .	26
2.4	Summary and outlook . . . . .	32
<b>Chapter 3 Mutual friction on quantized vortices in a BEC</b>		<b>38</b>
3.1	Introduction . . . . .	38
3.1.1	Generation of a doubly charged vortex . . . . .	40
3.2	Experiments . . . . .	42
3.3	Theoretical Model . . . . .	47
3.3.1	Motion of vortices . . . . .	47
3.3.2	Dynamics of corotating vortices in a harmonic trap . . . . .	48
3.4	Determination of Mutual friction $\alpha$ . . . . .	52
3.5	Summary . . . . .	54
<b>Chapter 4 Critical velocity for vortex shedding in a BEC</b>		<b>61</b>
4.1	Introduction . . . . .	62
4.2	Experiment . . . . .	65
4.2.1	Calibration of Gaussian beam . . . . .	69
4.3	Results and Discussion . . . . .	71
4.4	Summary . . . . .	77
<b>Chapter 5 Periodic vortex shedding from a moving Gaussian obstacle</b>		<b>82</b>
5.1	Introduction . . . . .	83
5.2	Experiment . . . . .	85

5.3	Periodic vortex shedding . . . . .	86
5.3.1	Penetrable obstacle . . . . .	86
5.3.2	Impenetrable obstacle . . . . .	90
5.4	Deterministic generation of a single vortex dipole . . . . .	93
5.5	Demonstration of a vortex dipole-dipole collision . . . . .	98
5.6	Possibility of a self-annihilation of a single vortex dipole? . . . . .	99
5.7	Vortex dipoles vs clustered vortex street . . . . .	102
5.8	Summary and Outlook . . . . .	104
<b>Chapter 6</b>	<b>Conclusions and Outlooks</b>	<b>111</b>
<b>Appendix A</b>	<b>Li 교체 진공작업</b>	<b>114</b>
<b>Appendix B</b>	<b>Offset lock for <math>^6\text{Li}</math> imaging laser</b>	<b>116</b>
<b>Appendix C</b>	<b>Measuring trapping frequency with parametric resonance</b>	<b>118</b>
<b>초 록</b>		<b>120</b>

# List of Figures

1.1	Interaction energy of two vortices . . . . .	9
2.1	Generation of turbulent flow in a BEC . . . . .	16
2.2	Vortex number counting method for a large number of vortices .	18
2.3	Relaxation of turbulence in a BEC . . . . .	19
2.4	Nonexponential decay of vortex number . . . . .	21
2.5	Vortex pair annihilation . . . . .	23
2.6	Rotating BEC vs turbulent BEC . . . . .	24
2.7	Appearance frequency of crescent-shaped density dimple . . . .	25
2.8	Tempolar evolution of a vortex number . . . . .	28
2.9	Decay rate $\Gamma_2$ as a function of trap frequency and atom number	30
2.10	Local two-body decay rate . . . . .	31
3.1	Generation of a doubly charged vortex . . . . .	41
3.2	Corotating vortex pair in a Bose-Einstein condensate . . . .	44
3.3	Evolution of the corotating vortex pair in a trapped Bose-Einstein condensate . . . . .	45
3.4	Numerical simulation of the dissipative point-vortex model . .	51
3.5	Friction coefficient $\alpha$ as a function of temperature $T$ . . . .	53

4.1	Soft boundary of the optical obstacle formed by a repulsive Gaussian potential . . . . .	63
4.2	Vortex shedding in a highly oblate Bose-Einstein condensate . . . . .	67
4.3	Critical velocity and number of vortices as a function of velocity for various $V_0$ . . . . .	68
4.4	Gaussian beam calibration . . . . .	70
4.5	Normalized critical velocity $v_c/c_s$ versus the relative barrier height $V_0/\mu$ for various beam widths $\sigma/\xi$ . . . . .	72
4.6	$v_c/c_s$ versus $\sigma/\xi$ for fixed $V_0/\mu \approx 7$ . . . . .	75
5.1	Schematic of the experiment . . . . .	85
5.2	Periodic shedding of vortex dipoles from a moving penetrable obstacle . . . . .	87
5.3	Vortex dipole number $N_d$ vs sweep length $L$ . . . . .	89
5.4	Vortex shedding from a moving impenetrable obstacle . . . . .	90
5.5	Various patterns of vortex shedding from impenetrable and penetrable beams . . . . .	92
5.6	Formation process of a vortex dipole . . . . .	94
5.7	Dependence of the intervortex distance $d$ on various sweeping parameters of the penetrable obstacle . . . . .	96
5.8	Propagation of a vortex dipole . . . . .	97
5.9	Head-on collision of two vortex dipoles . . . . .	99
5.10	possibility of a self-annihilation from an orbiting vortex dipole .	101
5.11	Shedding patterns of vortex dipoles and von Kármán street . . . . .	103
5.12	Shedding patterns of turbulence in a BEC . . . . .	104
6.1	Question mark of vortices . . . . .	112

B.1 Offset lock scheme for ${}^6\text{Li}$ imaging laser . . . . .	117
C.1 Measurement of trapping frequency with parametric resonance .	119

# Chapter 1

## Introduction

### 1.1 Ultracold Bose gas and vortex physics

Since the first realization of a Bose-Einstein condensate (BEC) of dilute gas with alkali atoms in 1995 [1, 2], superfluidity of a BEC and its excitations have long been investigated. A BEC has been a nice platform to study physics of a quantized vortex, which is a quantum version vortex in a superfluid. Despite many efforts to understand superfluid dynamics related to quantized vortices, however, there still exist many vacant parts. Motivated by this, we started to do experiments on vortices in a BEC to reveal details of vortex shedding and decaying dynamics.

One big part of this work is vortex-antivortex annihilation, which is very probable in a BEC superfluid due to its compressibility. It is crucial in a BEC superfluid and makes situation very different from a classical fluid. A classical fluid does not show such interesting phenomenon, especially in two dimensional incompressible Euler fluid, due to enstrophy conservation, rather a vortex merges

with other vortices and an antivortex combines with other antivortices.

The very first motivation of this thesis starts from finding experimental evidences of vortex pair annihilation in a BEC. This leads us to find interesting decaying features of quantum turbulence and we observe several traces that are supposed to be related to vortex pair annihilations. Then, we investigate mutual friction on quantum vortices which is necessary to understand thermal relaxation of the quantum turbulence. Our interests are naturally expanded to creation dynamics of vortices by vortex shedding from a moving obstacle. Eventually, we are able to construct a method to generate a vortex dipole deterministically, which will provide us with a chance to investigate the vortex pair annihilation directly by collision of two vortex dipoles or self-annihilation of a single vortex pair.

This thesis will focus on superfluid turbulence, especially its decaying behavior in a BEC, and response of a BEC from a moving repulsive obstacle. Before getting in deep, it will be helpful to be familiar with concept of a BEC, which has superfluidity for interacting case. For the following, I would like to write down short introduction to typical concepts of a quantized vortex in a BEC. (Please refer any textbook like [3] for details.)

## 1.2 Brief reviews on Bose-Einstein condensates

When a temperature of dilute gas system becomes lower than a critical temperature  $T_c$  for Bose-Einstein condensation, there comes nonzero macroscopic wavefunction (order parameter)  $\psi(\mathbf{r})$ , which describes the states of condensed atoms.

Due to the diluteness of the system, where interatomic distance is much

larger than effective potential length scale, it is unnecessary to know the details of the interatomic potential and rather, it is convenient to introduce pseudopotential whose s-wave scattering length is same as the real one. (since atoms are in ultracold regime, scattering of two atoms can be described by a single parameter, i.e., s-wave scattering length  $a$ .) Such pseudopotential is given by

$$U_0 \delta(\mathbf{r}_i - \mathbf{r}_j), \quad U_0 = \frac{4\pi a \hbar^2}{m}. \quad (1.1)$$

and effective Hamiltonian is written as [3]

$$H = \sum_{i=1}^N \left[ -\frac{\hbar^2}{2m} \nabla_i^2 + V(\mathbf{r}_i) \right] + U_0 \sum_{i < j} \delta(\mathbf{r}_i - \mathbf{r}_j), \quad (1.2)$$

where  $V(\mathbf{r})$  is external potential of the system.

With such a contact potential Eq. 1.1, the condensate wave function  $\psi(\mathbf{r})$  can be described as

$$-\frac{\hbar^2}{2m} \nabla^2 \psi(\mathbf{r}) + V(\mathbf{r}) \psi(\mathbf{r}) + U_0 |\psi(\mathbf{r})|^2 \psi(\mathbf{r}) = \mu \psi(\mathbf{r}), \quad (1.3)$$

where  $\mu = \partial E / \partial N$  is chemical potential of the system and  $N$  is the number of the condensate. Eq. (1.3) is called stationary Gross-Pitaevskii equation (sometimes non-linear Schrödinger equation).

For the typical cases, kinetic energy is small compared to other energies and it is often neglected. This is called Thomas-Fermi approximation and  $\psi(\mathbf{r})$  is written as [3]

$$(V(\mathbf{r}) + U_0 |\psi(\mathbf{r})|^2) \psi(\mathbf{r}) = \mu \psi(\mathbf{r}). \quad (1.4)$$

and the condensate density  $n(\mathbf{r})$  is

$$n(\mathbf{r}) = |\psi(\mathbf{r})|^2 = (\mu - V(\mathbf{r})) / U_0. \quad (1.5)$$

For harmonic trap where  $V(\mathbf{r}) = 1/2m(\omega_x^2x^2 + \omega_y^2y^2 + \omega_z^2z^2)$ , one finds

$$\mu = \frac{15^{2/5}}{2} \left( \frac{Na}{\bar{a}} \right)^{2/5} \hbar\bar{\omega}, \quad (1.6)$$

where  $\bar{a} = \sqrt{\frac{\hbar}{m\bar{\omega}}}$  and  $\bar{\omega} = (\omega_x\omega_y\omega_z)^{1/3}$ .

## 1.3 Vortices in a BEC

### 1.3.1 Quantized vortex in a BEC

A quantized vortex is one of elementary excitations in a BEC. To understand its property, let us start with time-dependent Gross-Pitaevskii equation,

$$i\hbar \frac{\partial}{\partial t} \psi(\mathbf{r}) = -\frac{\hbar^2}{2m} \nabla^2 \psi(\mathbf{r}) + V(\mathbf{r})\psi(\mathbf{r}) + U_0|\psi(\mathbf{r})|^2\psi(\mathbf{r}). \quad (1.7)$$

Multiplying  $\psi^*$  to both sides of Eq. 1.7 yields,

$$i\hbar\psi^* \frac{\partial}{\partial t} \psi = -\frac{\hbar^2}{2m} \psi^* \nabla^2 \psi + V(\mathbf{r}) |\psi|^2 + U_0 |\psi|^4. \quad (1.8)$$

Subtracting the Eq. 1.8 from its complex conjugate gives,

$$\frac{\partial}{\partial t} |\psi|^2 + \frac{\hbar^2}{2mi} \nabla \cdot (\psi^* \nabla \psi - \psi \nabla \psi^*) = 0, \quad (1.9)$$

where the fluid velocity is written as follows,

$$\vec{v} = \frac{\hbar}{2mn} (\psi^* \nabla \psi - \psi \nabla \psi^*). \quad (1.10)$$

Therefore, Eq. 1.9 is simply the continuity equation of the condensate. Since  $\psi$  can be expressed in terms of its amplitude (density  $n$ ) and phase term such that  $\psi = \sqrt{n}e^{i\phi}$ , velocity can thus be expressed as

$$\vec{v} = \frac{\hbar}{m} \nabla \phi. \quad (1.11)$$

This tells us that vorticity vector  $\vec{\omega} = \nabla \times \vec{v}$  is zero due to the fact that curl of gradient is zero (actually it is delta function in this case). And single valuedness of wavefunction results in the fact that integration of  $\phi$  around closed contour should be a multiple of  $2\pi$ ,

$$\Delta\phi = \oint \nabla\phi \cdot d\vec{l} = 2\pi l, \quad (1.12)$$

where  $l$  is an integer. This is directly related to quantized circulation of a vortex where the circulation becomes

$$\Gamma = \oint \vec{v} \cdot d\vec{l} = \frac{\hbar}{m} l. \quad (1.13)$$

If we consider purely azimuthal flow around the condensate center, a velocity field becomes

$$v = \frac{l\hbar}{mr}, \quad (1.14)$$

which is the case when the vortex core is located at the center of the condensate. The field is exactly same as that of irrotational flow in classical fluid except the fact that the circulation of a vortex is quantized. This is a quantized vortex of charge  $l$  in a BEC. One should remind that the quantized vortex is directly connected to a BEC but not superfluidity, since discussions above purely come from BEC wavefunction which itself is not sufficient to show superfluidity. That is, even for the case of non-interacting BECs, quantized vortices can be produced.

Since the velocity diverges at the center of the vortex, density converges to zero at the center due to centrifugal force. Near the center, the kinetic term of the Eq. 1.3 is relatively large to interaction energy term. Far away from the vortex center, now the interaction energy term dominates. So it is common to relate vortex core length scale to healing length  $\xi$  of the condensate,

$$\frac{\hbar^2}{2m\xi^2} = nU_0 = \mu. \quad (1.15)$$

### 1.3.2 Angular momentum of a vortex

Let's consider a singly quantized vortex in a cylindrical trap, where the atomic density is uniform. The angular momentum (per unit length) of the system is given by

$$L = nm \int r^2 v_\theta dr d\theta, \quad (1.16)$$

where  $n$  represents constant density and  $v_\theta$  is azimuthal component of the velocity. The angular integration is

$$\int r v_\theta d\theta = \oint \vec{v} \cdot d\vec{l} = \Gamma, \quad (1.17)$$

which means that if the integral contour contains a vortex core, the value is  $\frac{\hbar}{m}$  and zero otherwise. When the vortex is located at a distance  $b$  from the center of the cylindrical trap of radius  $R$ ,  $L$  becomes

$$L = nh \int_b^R r dr = n\hbar\pi R^2 \left( 1 - \frac{b^2}{R^2} \right). \quad (1.18)$$

This tells us that the angular momentum of the system is given by the number of atoms outside the radius  $b$  each having angular momentum of  $\hbar$ . Angular momentum  $L$  is getting smaller as the vortex moves far away from the central axis. Thus, if a single vortex is in the condensate, its distance from the center cannot be changed, due to the conservation of angular momentum.

But, its possibility to moving out the condensate depends on the situation. When the temperature of the system is nonzero so that the thermal gas exists, thermal dissipation between superfluid and thermal component induces a decrease of angular momentum of the superfluid, which, as a result, increases an angular momentum of thermal component. In such nonzero temperature condensate, the vortex spirals out to the condensate boundary. (The experiments on such dissipation will be discussed in ch. 3)

It is noticeable that when there are many singly charged vortices in the condensate whose distances are  $b_i$  from the center, total angular momentum of the system is given by the sum of angular momentum of each vortex, i.e.,  $\sum L_i$  where each  $L_i$  is obtained from Eq. 1.18.

Even without dissipation so that the total angular momentum of the condensate itself should be conserved, a vortex can move towards the boundary of the condensate if there exist other vortices (including antivortices) in the condensate. In other words, the decrease of angular momentum due to vortices moving outwards can be compensated by an increase of angular momentum from vortices moving into the center of the condensate.

### 1.3.3 Interaction of two vortices

To understand a case of two vortices, both vortex-antivortex pair and two corotating vortices, let's first see the energy of a single vortex in a uniform condensate. Kinetic energy of a vortex can be directly calculated as

$$E_K = \int \frac{1}{2}mv^2 n(\vec{r}) dA = \frac{1}{2}mn \int_{\xi}^R \frac{l^2 \hbar^2}{m^2 r^2} 2\pi r dr = \frac{l^2 \hbar^2 n \pi}{m} \ln \frac{R}{\xi}, \quad (1.19)$$

where we assume uniform density  $n$  and the condensate radius  $R$  is much larger than  $\xi$ . Here, we neglect the kinetic energy of the vortex core. One finds that the energy is proportional to  $l^2$  which means that a highly charged vortex can possibly be dissociated into many singly quantized vortices.

Kinetic energy of two vortices of charge  $l_1$  and  $l_2$  whose intervortex dis-

tance is  $d$  can be calculated as follows (see Fig. 1.1)

$$\begin{aligned}
E_K &\propto \int_A (\vec{v}_1 + \vec{v}_2)^2 dA \propto \int_A (\nabla\phi_1 + \nabla\phi_2)^2 dA \\
&= E_1 + E_2 + 2 \int_A (\nabla\phi_1 \cdot \nabla\phi_2) dA \\
&= E_1 + E_2 + 2 \left( \int_A (\nabla \cdot (\phi_1 \nabla\phi_2)) dA - \int_A (\phi_1 \nabla^2 \phi_2) dA \right) \\
&= E_1 + E_2 + 2 \int_{\partial A} (\phi_1 \nabla\phi_2) \cdot \hat{n} dr \\
&= E_1 + E_2 + 2 \times (2\pi l_1) \int_d^R \nabla\phi_2 \cdot \hat{n} dr \\
&= E_1 + E_2 + 4\pi l_1 l_2 \ln\left(\frac{R}{d}\right). \tag{1.20}
\end{aligned}$$

I used integration by parts, divergence theorem, and the fact that  $\nabla^2\phi = 0$ .

This equation simply becomes

$$\begin{aligned}
E_K &= \frac{n\hbar^2}{2m} \left( E_1 + E_2 + 4\pi l_1 l_2 \ln\left(\frac{R}{d}\right) \right) \\
&= \frac{n\hbar^2\pi}{m} \left( (l_1 + l_2)^2 \ln\left(\frac{R}{\xi}\right) - 2l_1 l_2 \ln\left(\frac{d}{\xi}\right) \right). \tag{1.21}
\end{aligned}$$

Eq. 1.21 is just like that of two dimensional Coulomb gases, which means that two vortices can effectively interact with each other depending on its circulation signs and intervortex distance  $r$ , i.e., repulsive interaction for same signs and attractive interaction for different signs. This is very important results when there exists a dissipation in the system so that the energy of two nearby vortices decreases by becoming closer or further away depending on their interactions. Chapter. 3 treats two corotating vortices which have repulsive interactions.

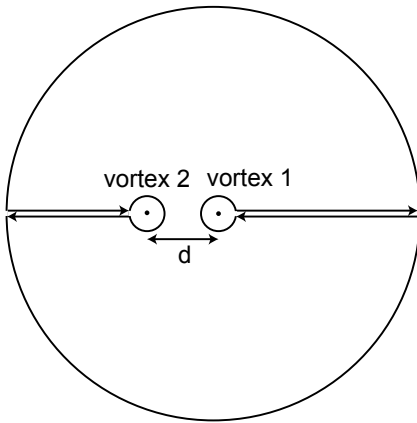


Figure 1.1: Contour used to calculate kinetic energy when intervortex distance is  $d$  and condensate radius is  $R$ .

## 1.4 Outline of the thesis

This thesis is organized as follows.<sup>1</sup> Ch.2 will describe our experiments on decaying turbulence under finite temperature which is interpreted with vortex pair annihilation mechanism. Nextly, in ch.3, two corotating vortices in a finite temperature BEC will be introduced and the experimental results will be discussed based on the mutual friction. The mutual friction between superfluid and thermal component is a fundamental element to understand decay of vortices so these two chapters are closely related.<sup>2</sup>

---

<sup>1</sup>At the early years of my Ph.D course, I went through many trials and errors to upgrade a machine to dual species system for generating both bosonic ( $^{23}\text{Na}$ ) and fermionic ( $^6\text{Li}$ ) gases. And finally I figure out that there exists systematic limits within our optically plugged magnetic trap scheme to produce ultracold  $^6\text{Li}$  gas, i.e., because of the power limit of plugging laser it was hard to sufficiently plug the hole of the magnetic trap. I had no choice but doing other experiments using bosonic gases. Thereafter, I started to investigate interesting phenomenon related to vortices. (Even after a new plugging laser (Verdi 10W) had arrived!) Major part of my Ph.D course (during 2013 ~ present) has been devoted to studies on vortex dynamics. And this thesis focuses on the studies on vortices.

<sup>2</sup>If the readers want to get informations on our experiment machine, please see J. Choi's thesis [4] or [5, 6].

Ch.4 and 5 will concentrate on dynamics of vortex shedding including critical velocity and characteristics of shedding depending on an obstacle beam. Especially in ch. 5, possibility of vortex pair-pair collision experiment and observing novel shedding patterns from impenetrable beam will also be demonstrated. Finally, summary and future outlooks on vortex shedding experiments will be discussed in ch.6.

# Bibliography

- [1] M. H. Anderson, J. R. Ensher, M. R. Matthews, C. E. Wieman, and E. A. Cornell, Science **269**, 198 (1995)
- [2] K. B. Davis, M. -O. Mewes, M. R. Andrews, N. J. van Druten, D. S. Dufree, D. M. Kurn, and W. Ketterle, Phys. Rev. Lett. **75**, 3969 (1995).
- [3] C. J. Pethick and H. Smith, *Bose-Einstein Condensation in Dilute Gases* (Cambridge University Press, Cambridge, England, 2008).
- [4] Jae-yoon Choi, *Thermal Phase Fluctuations in a Quasi-2D Bose-Einstein Condensate*. Ph.D thesis, Seoul National University, 2014. (can be downloaded from SNU library)
- [5] M. Heo, J. Choi, and Y. Shin, Physical Review A **83**, 013622 (2011).
- [6] J. Choi, M. Heo, and Y. Shin, Journal of the Korean Physical Society **59**, 211 (2011).

# Chapter 2

## Quantum turbulence in a BEC

This chapter describes our experiments on quantum turbulence, especially on decay of the turbulence in a BEC. The experimental results and related data are published in the following paper.

- W. J. Kwon, G. Moon, J. Choi, S. W. Seo, and Y. Shin, “*Relaxation of superfluid turbulence in highly oblate Bose-Einstein Condensates*”, Physical Review A **90**, 063627 (2014).

### 2.1 Introduction

Turbulence is a quite familiar phenomenon to many people because we can feel it intuitively when we take an airplane or even when we play a football. The definition of turbulence in physics, however, is not that easy and perhaps it would be more appropriate to say that the meaning of the turbulence cannot be definitely defined. Loosely speaking, turbulence indicates an irregular and chaotic vortical flow. One of characteristic features of turbulence is that it con-

tains large ranges of eddies. It is highly nonlinear and unpredictable so that the many theoretical studies on turbulence focus on its statistical properties. In this thesis, the meaning of turbulence is not much strict and mostly indicates an irregular motion of vortical flow.

Quantum turbulence (superfluid turbulence) is a quantum analogue of classical turbulence, where the biggest difference lies on quantization of vortices. This is a part of nonequilibrium quantum physics which is very fundamental but mostly unexplored yet. Within the BEC community, studies on quantum turbulence have just started and mainly focused on theoretical approaches. The most striking phenomenon in quantum turbulence is about vortex reconnection in three dimensional (3D) quantum fluids which makes the fluid very tangled with vortex lines. How will the quantum many body system remove the topological objects like vortices as they become to equilibrium states? Our work will be an example experiment on this issue, in a two dimensional (2D) quantum turbulence.

In a superfluid, quantized vortices are topological, point-like objects and they can be created and also annihilated as a pair of vortices of opposite circulation. Vortex-antivortex pairs play essential roles in 2D superfluid phenomena such as the Berezinskii-Kosterlitz-Thouless transition [1, 2], phase transition dynamics [3], and superfluid turbulence [4, 5]. Recently, controlled experimental studies of vortex dipole dynamics have been enabled in atomic Bose-Einstein condensate (BEC) systems [6, 7] and thermal activation of vortex pairs has been observed in quasi-2D Bose gases [8, 9]. However, the annihilation of a vortex-antivortex pair has not been clearly observed yet.

### 2.1.1 Decay of a vortex in a superfluid

It is important to note that compressibility of a superfluid, e.g. BEC, takes major roles for opening a new channel for a vortex to die by exchanging its energy into acoustic energy, i.e., sound waves. That is, vortex-antivortex pair can be annihilated by radiating sounds. Moreover, reverse process, i.e., transformation of interacting sounds into a vortex pair, is also possible. In an incompressible fluid, such as classical Euler fluid, however, vortex dynamics should be treated differently from that of a BEC due to lack of compressibility.

Vortex pair annihilation is of particular importance in 2D superfluid turbulence. In 2D turbulence of a classical hydrodynamic fluid (incompressible and inviscid case), the kinetic energy of the system flows toward large length scales due to the conservation of enstrophy which is integral of squared vorticity [10]. This is known as the inverse energy cascade and manifests itself in generating large-scale flow structures from small-scale forcing. This phenomenon is qualitatively different from three-dimensional (3D) turbulence where energy is typically dissipated into small length scales. An interesting question is whether the inverse cascade can occur in an atomic BEC. Since the enstrophy, proportional to the total number of quantized vortices in quantum turbulence, is not conserved in a compressible 2D superfluid due to the vortex-antivortex annihilation, there has been a theoretical controversy on this issue [11–20]. Recently, Neely *et al.* [21] reported an experimental and numerical study to show that there are conditions for which 2D turbulence in a BEC can dissipatively evolve into large-scale flow.

In this chapter, we investigate thermal relaxation of turbulent superflow in highly oblate BECs. By sweeping the center region of a trapped condensate with a repulsive optical potential, we generate turbulent flow with a spatially

disordered vortex distribution. We measure the temporal evolution of the vortex number and observe nonexponential decay behavior in the relaxation, which we attribute to the vortex pair annihilation. The vortex-antivortex collisions in the condensate are identified with crescent-shaped, coalesced vortex cores. We characterize the nonexponential decay of the vortex number with one-body and two-body decay rates, and find in our measurements that the local two-body decay rate is closely proportional to  $T^2/\mu$ , where  $T$  is the temperature and  $\mu$  is the chemical potential of the sample. Our results on the decay rates provide quantitative information on the thermal dissipation in 2D quantum turbulence, in particular, with finite compressibility.

## 2.2 Experimental methods

### 2.2.1 Generating turbulence in a BEC

We prepare a highly oblate BEC of  $^{23}\text{Na}$  atoms in the  $|F = 1, m_F = -1\rangle$  state in a harmonic trap, where the axial and radial confinements are provided by optical and magnetic trapping potentials, respectively. The magnetic potential is generated from an axially symmetric, magnetic quadrupole field. The trapping frequencies are  $\omega_{r,z} = 2\pi \times (15, 350)$  Hz. For a condensate of  $N_0 = 1.8 \times 10^6$  atoms, the chemical potential is  $\mu \approx k_B \times 60$  nK and the radial Thomas-Fermi (TF) radius is  $R = \sqrt{2\mu/m\omega_r^2} \approx 70$   $\mu\text{m}$ , where  $m$  is the atomic mass. Because of the large aspect ratio of the condensate,  $\omega_z/\omega_r > 20$ , the vortex line excitations are highly suppressed [22, 23] and we expect that the vortex dynamics in our system is 2D. Note that  $\mu > 3\hbar\omega_z$  and the condensate is thermodynamically 3D.

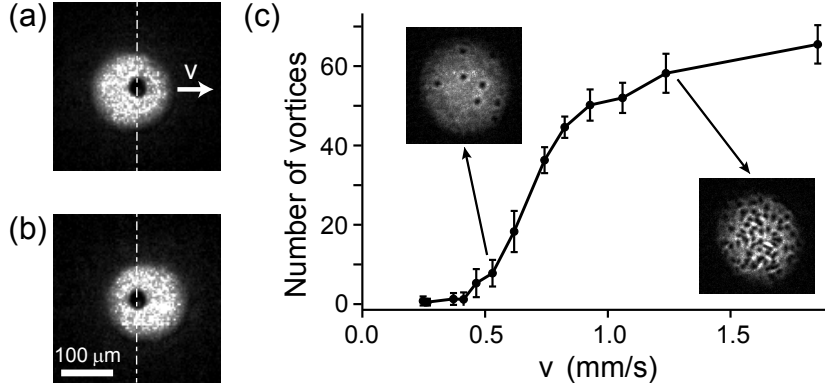


Figure 2.1: Generation of turbulent flow in a BEC. A repulsive laser beam penetrates through the condensate and sweeps its center region by horizontally translating the trapped condensate by  $37 \mu\text{m}$ . Images of the trapped condensate (a) before and (b) after the translation. (c) Number of the vortices in the perturbed condensate as a function of the translation speed  $v$ . The speed of sound is estimated to be  $c \approx 4.6 \text{ mm/s}$  at the center of the condensate

To generate turbulent flow in the condensate, we employ a repulsive Gaussian laser beam as a stirring obstacle<sup>1</sup>. Having the laser beam axially penetrating through the condensate, we translate the condensate in a transverse direction by moving the magnetic trap center by  $37 \mu\text{m}$  for 30 ms (Fig. 1), and adiabatically turn off the laser beam for 0.4 s. Here the laser beam, fixed in the lab frame, sweeps the center region of the condensate. The Gaussian beam waist is  $15 \mu\text{m}$  and the barrier height is about  $15\mu$ . The translation speed corresponds to  $\sim 0.3c$ , where  $c = \sqrt{\mu/m}$  is the speed of sound. We detect vortices in the turbulent flow by taking an absorption image after 24 ms time-of-flight. With this procedure, we could generate over 60 vortices in our coldest sample without inducing noticeable shape oscillations of the condensate. The critical

---

<sup>1</sup>One should be aware that even a HEPA filter on top of the machine table, which continuously generates wind on the system, extremely affects the generation of vortices. It should be turned off to obtain data of better quality.

velocity for the vortex nucleation was measured to be  $\approx 0.1c$  [Fig. 2.1].

Since we induce linear motion of a BEC, dipole oscillation is inevitable for this method (a reason for translating the condensate with magnetic quadrupole trap rather than moving the Gaussian beam itself is that we didn't have a piezodriven mirror at that time). Due to its oscillating motion, vortex dipoles are continuously generated after the complete translation of the condensate which is good for making a BEC full of vortices. The production of vortices are kept going when green beam power is ramped down. The dipole motion is seemingly very small and terminated soon after completely turning off the beam whose energy should be dissipated via producing vortex dipoles.

### 2.2.2 Vortex number counting

To measure the number of vortices in turbulent sample, we use automated counting method (Fig. 2.2). We make a blurred image by applying boxcar smoothing to original absorption image, where the box width is set to be  $30 \mu\text{m}$ , comparable to the vortex core diameter. And we divide the raw absorption image by its blurred image and then convert it into a binary image for a certain threshold value. With this imaging process, the density-depleted vortex cores in the absorption image are transformed into particles in the binary image. All these process are done by “Igor Pro” program which provides a “ImageAnalyzeParticles” command.

Since each particle has a different area depending on the number of vortices it contains, we obtain histogram of the particle area size. The histograms show a mutiple peak structure and we assign a vortex number to each particle according to its area size. We set the vortex number transition lines (dashed

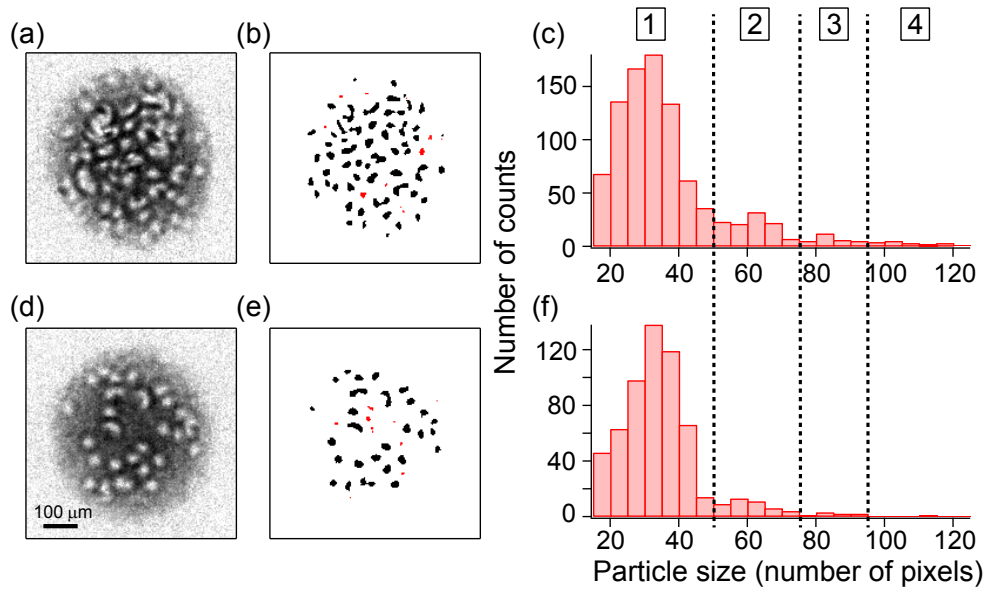


Figure 2.2: Automated vortex number counting method for a large number of vortices in a turbulent BEC. (a) Absorption image of the condensate after expansion. (b) A binary image obtained from (a) and its blurred version (see the text). Black particles correspond to the vortex cores and red particles, having area sizes less than 15 pixels, are artifacts due to image defects. (c) Histogram of the particle area size from 24 image data. We set the vortex number transition lines (dashed lines) in the middle of the peaks. (d)–(f) display another example set of the image analysis, where the condensate contains about 30 vortices.

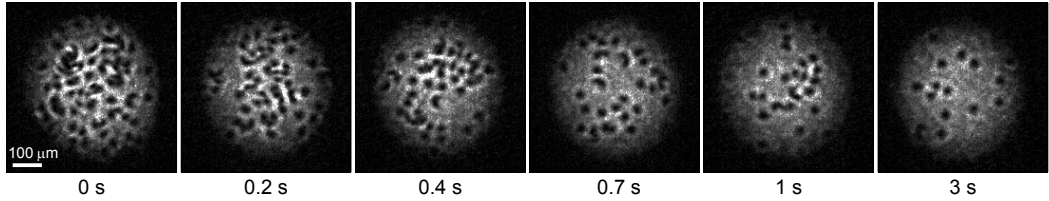


Figure 2.3: Relaxation of turbulent superflow in a highly oblate BEC. Examples of images for various relaxation times, where the atom number of the condensate  $N_0 \approx 1.8 \times 10^6$  and the condensate fraction  $\eta \approx 0.8$ .

lines) in the middle of the peaks(Fig. 2.2(d)). Most of the particles having an area less than 15 pixels are due to image defects and ignored in our counting.

Due to the fact that healing length  $\xi$  is a function of the density which makes vortex size dependent on the radial position, it is a bit hard to obtain accurate vortex number. Most ambiguities in the counting come from the boundary region of the condensate and some unexpected image defects, but are not significant. It is worthwhile to note that small different setting of each vortex number transition line does not affect much to average number of vortices when there's a large number of vortices. In comparison with hand counting, we confirmed that this method gives a consistent result within  $< 10\%$  ( $\sim 5$  vortices). However, when the total vortex number is less than 30, we counted the vortex number by hand in our data analysis which gives smaller error.

## 2.3 Relaxation of Turbulence

### 2.3.1 Nonexponential decay

Figure 2.3 shows some representative images of various hold times. It turns out that there are not much collective motions or deformations in the condensate.

The turbulent condensate shows spatially disordered distributions of vortices. In the early phase of the evolution, some features in the condensate seem to be suggestive of vortex clustering, but we observed no evidence in the spatial analysis of the vortex distributions using Ripley's  $K$ -function [24]. We find that turbulent condensate eventually relaxes into a stationary state as the vortex number decreases in the harmonically trapped system.

We observe nonexponential decay behavior of the vortex number in the relaxation 2.4, where the decay rate is faster for higher vortex number. There are only two ways for a quantum vortex to disappear from a condensate of finite spatial extent: drifting out of the condensate boundary or being annihilated as a vortex-antivortex pair. Since our turbulence generation method imparts no angular momentum to the condensate, the initial turbulent condensate would have equal numbers of vortices for clockwise and counterclockwise circulations, and both of the drifting-out and the pair annihilation processes must be involved in its relaxation dynamics. Since the pair annihilation is intrinsically a two-vortex process, it might be a reason for the nonexponential decay of the vortex number.

To examine the details of the nonexponential behavior of  $N_v$ , we directly obtain the decay rate  $-dN_v/dt$  as a function of mean vortex number (Fig. 2.4). In the log-log plot, it is clearly seen that the dependence of the decay rate on  $N_v$  cannot be captured by a single power-law relation over the whole range of our measurements. The power-law fits for the low-vortex-number ( $N_v < 10$ ) data and the high -vortex-number ( $N_v > 10$ ) data give the exponents of 1.29(17) and 1.77(20), respectively.

Partly motivated by the measured values of the exponents, we suggest a

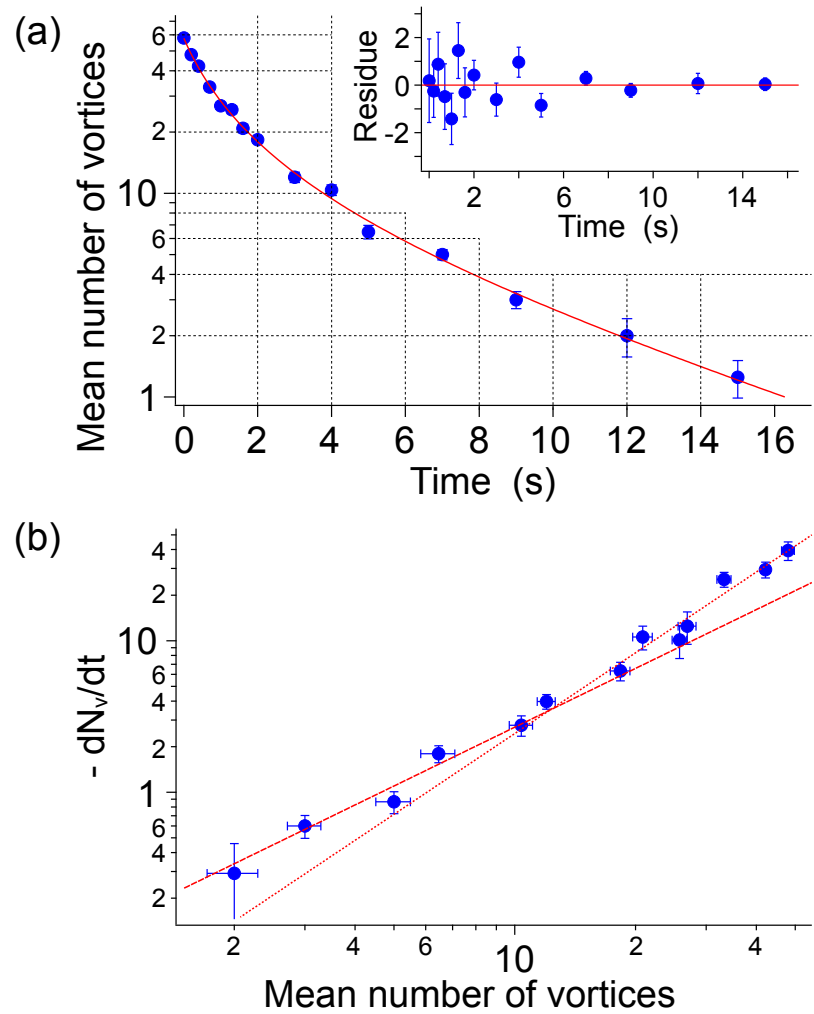


Figure 2.4: Nonexponential decay of superfluid turbulence. (a) Mean number of vortices versus time. Insets shows residue of fitting curve using Eq (1). (b) The log-log plot of decay rate  $-dN_v/dt$  as a function of mean number of vortices. Power law fittings to  $N_v < 10$  region and  $N_v > 10$  region are clearly different. Power law fits give exponents of 1.29(17) and 1.77(20), respectively.  $N_0 \approx 1.8 \times 10^6$  and  $\eta \approx 0.8$ . Each point consists of at least 12 same experimental realizations.

phenomenological rate equation for  $N_v$  as

$$\frac{dN_v}{dt} = -\Gamma_1 N_v - \Gamma_2 N_v^2, \quad (2.1)$$

This expression is widely used for loss of particles, such as kinetic gas theory where the first term is relevant to decay due to the background and the second term is responsible for collisional process with another particle of same kind. Note that, when the two particles of same kind or different kind collide, the number of collisional events is proportional to  $N \times (N - 1)/2$  or  $N_1 \times N_2$ , respectively, where  $N_1$  and  $N_2$  represents the number of two different particles. Here, since decay due to collision is only possible for ‘vortex’ and ‘antivortex’ collision, the latter is appropriate.

More specifically, we assume that the number of ‘vortex’  $N_{vor}$  and ‘antivortex’  $N_{anti}$  follow

$$\frac{dN_{vor}}{dt} = -\Gamma_1 N_{vor} - \Gamma_2 N_{vor} \times N_{anti}, \quad (2.2)$$

$$\frac{dN_{anti}}{dt} = -\Gamma_1 N_{anti} - \Gamma_2 N_{vor} \times N_{anti}. \quad (2.3)$$

Summing these two equations gives Eq. 2.1 when  $N_{vor} = N_{anti} = N_v/2$ .

We observe that the measured decay curve of  $N_v$  is remarkably well described with the rate equation. The residue of the experiment data from the fitting line of the rate equation is smaller than 2 vortices [Fig. 2.4(a) inset]. A simple consideration based on the kinetic gas theory suggests that the one-body and two-body decay rates,  $\Gamma_1$  and  $\Gamma_2$ , might be mainly determined by the drifting-out process and the pair annihilation process, respectively. However, we cannot exclude many-vortex effects on the drifting-out process, which would possibly affect the two-body decay rate  $\Gamma_2$ . In this work, we employ the two decay rates,  $\Gamma_1$  and  $\Gamma_2$ , to characterize the relaxation of the turbulent condensate.

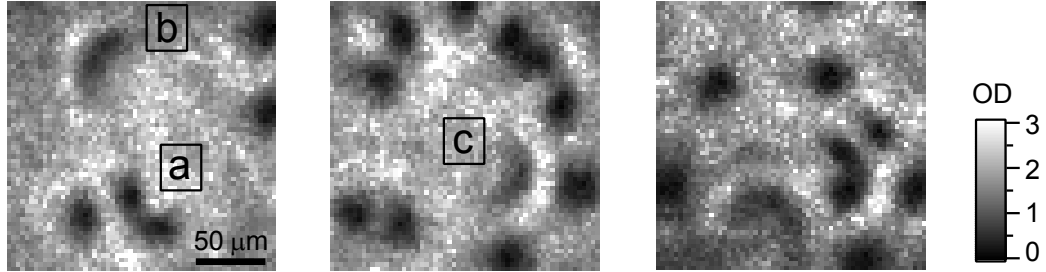


Figure 2.5: Vortex pair annihilation in the turbulent superflow. Density-depleted regions with a crescent shape are observed in the turbulent condensates. In a vortex-antivortex collision event, two vortex cores can coalesce (a), evolve into a dark soliton (b), and disappear as atoms fill up the density-depleted region (c). The bending structure results from the linear momentum of the vortex dipole.

### 2.3.2 Vortex pair annihilation

Vortex pair annihilation occurs when two vortices of opposite circulation collide, converting their energy into sound waves in the superfluid. Numerical studies showed that a dark or gray soliton of a crescent shape is formed via coalescing the vortex cores in the collision and it can dissipatively evolve into a shock wave [4, 25, 26]. Indeed, we observe crescent-shaped density-depleted regions in the condensate (Fig. 2.5), revealing the vortex-antivortex collision events in the turbulent flow. We note that such a feature was not observed in rotating condensates, in which most of the vortices have same circulation [27, 28]. The bending structure can be accounted for by the linear momentum of the vortex dipole which is perpendicular to the vortex dipole direction. Some of the coalesced vortex cores appear with significantly reduced visibility [Fig. 2.5(c)], possibly indicating that they are being annihilated.

We emphasize that such a crescent-shaped vortex core was not observed in rotating, turbulent condensates [27, 28] (Fig. 2.6). In this case, vortices were

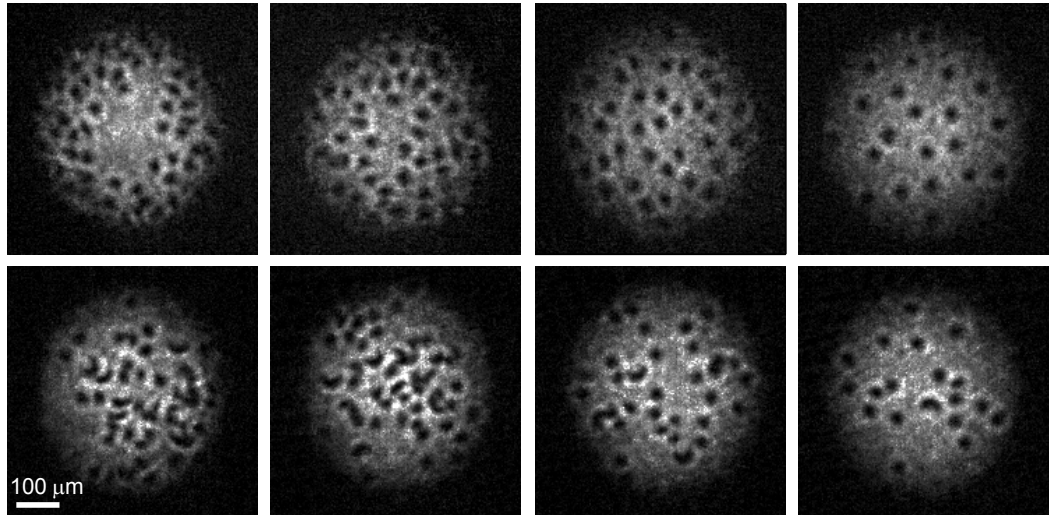


Figure 2.6: The upper row shows images of rotating Bose-Einstein condensates containing vortices of same circulation. Different from the main experiment, the vortex generation was carried out by circulating a condensate in an anharmonic magnetic trapping potential [27, 28]. The trap geometry and the imaging procedure were identical to those in the main experiment. No crescent-shaped vortex core is observed in the rotating condensates. In the lower row, images of turbulent condensates similar to those in Fig. 2.3 are displayed for comparison, where turbulence were generated by the laser-beam sweeping method (Fig. 2.1).

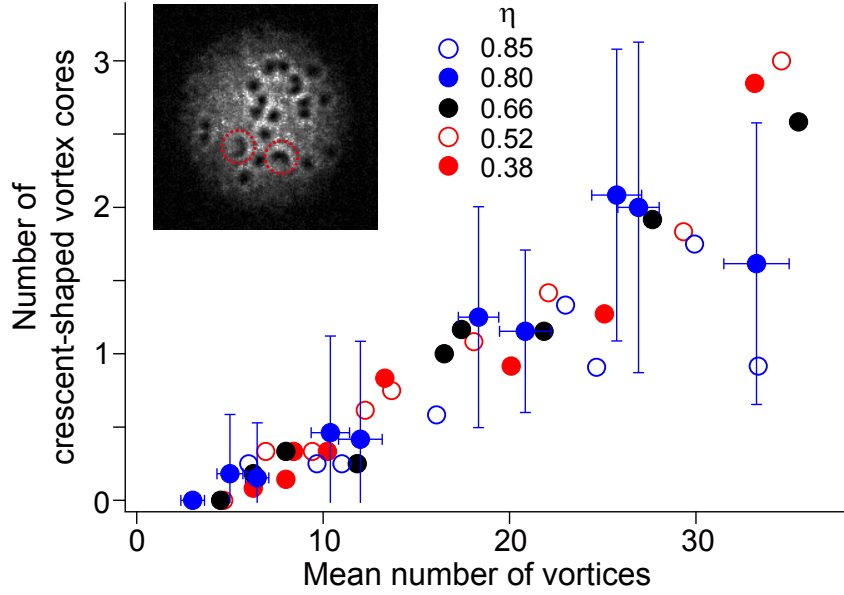


Figure 2.7: The number of crescent-shaped vortex cores versus the total vortex number  $N_v$  in a turbulent condensate. Each measurement point consists of at least 12 realizations of the same experiment. The inset shows an image of a turbulent condensate with two crescent-shaped vortex cores (red dashed circles).

generated by circularly shaking the magnetic trapping potential, where most of the vortices have same circulation. Here, anharmonic trapping potential transfers the external angular momentum to internal angular momentum, i.e. vortices. The trap geometry and the imaging procedure were identical to those in this work, thus excluding the possibility of imaging artifacts such as vortex line tilting. The crescent-shaped density dimple obviously comes from a vortex-antivortex pair.

The appearance frequency of the crescent-shaped density dimple is found to be almost linearly proportional to the total vortex number  $N_v$  and insensitive to the sample temperature (Fig. 2.7). At high vortex density  $n_v$ , a 2D turbulent superfluid can be considered as a gas of vortex-antivortex pairs [16, 17]. For a

vortex pair of size  $d$ , the collisional cross section  $\sigma \sim d$  and the linear velocity  $v \sim \hbar/md$ , giving the vortex collision rate as  $\gamma_c = \sigma v n_v / 2 \sim (\hbar/2m)n_v$ . This estimation provides a qualitative explanation of the observed  $N_v$  dependence of the appearance frequency of the crescent-shaped density dimple. We note that the numerical results in Ref. [16, 17] for a homogeneous system showed that  $\gamma_c$  has different power-law dependence on  $n_v$  at low vortex density,  $n_v \xi^2 < 3 \times 10^{-3}$  ( $\xi = \hbar/\sqrt{2m\mu}$  is the vortex core size). The vortex density of our sample is  $n_v \xi^2 < 10^{-3}$  with  $n_v = N_v/(\pi R^2)$ , but direct comparison of our observation to the prediction is limited due to the sample inhomogeneity.

It is important to note that we cannot conclude that such vortex pair collision events will immediately lead to pair annihilation events. First, a chance to find density dimples of light gray (Fig. 2.5 (c)). Second, a tightly bound pair, having a high linear momentum, would have a chance to cross the condensate to the boundary region and the pair might have a chance to move out of the condensate, rather than being annihilated. Nonetheless, as annihilation events itself are intrinsically accompanied by collisions, annihilation events would be proportional to the appearance frequency of the crescent-shaped vortices.

### 2.3.3 Decay rate measurements

The local vortex dynamics in a homogeneous system is governed by the temperature  $T$  and the chemical potential  $\mu$  of the system: at finite temperature, a vortex experiences a friction force caused by collisional exchange of atoms between the condensate and the thermal cloud [29–31], and the chemical potential determines the vortex core size  $\xi \propto \mu^{-1/2}$ , providing a characteristic length scale in the vortex dynamics. In this subsection, we present the measurement results

of the decay rates of the vortex number for various sample conditions.

## Temperature

We first investigate the temperature dependence of the decay rates. In order to reduce the effects from the variation of  $\mu$ , which determines the radial extent of the condensate,  $R$ , as well as the vortex core size  $\xi$ , the atom number of the condensate,  $N_0 = \eta N$ , is kept to be almost constant [Fig. 2.8(a) inset], where  $\eta$  is the condensate fraction and  $N$  is the total atom number. In the Thomas-Fermi approximation,  $\mu = (15N_0a/\bar{a})^{2/5}\hbar\bar{\omega}/2 = \frac{1}{2}m\omega_r^2R^2$  with  $a$  being the scattering length of atoms,  $\bar{a} = \sqrt{\hbar/m\bar{\omega}}$ , and  $\bar{\omega} = \omega_r^{2/3}\omega_z^{1/3}$ .  $N$  and  $\eta$  are measured right after turning off the repulsive laser beam. The temperature is estimated from  $T = T_c(1 - \eta)^{1/3}$  and  $k_B T_c = 0.94\hbar\bar{\omega}N^{1/3}$ .<sup>2</sup> During 15 s hold time, the condensate fraction  $\eta$  was observed to decrease less than 10%, showing that there is no significant heating in the relaxation. The lifetime of the sample in the trap was over 60 s.

The measurement results are displayed in Fig. 2.8. Both of the decay rates monotonically increase as the temperature is increased [Fig. 2.8(b) and 2.8(c)], demonstrating the thermal nature of the relaxation dynamics. It is noticeable that the two-body decay rate,  $\Gamma_2$ , shows a faster response to the temperature than the one-body decay rate,  $\Gamma_1$ , and this seems to imply that the physical mechanisms determining each decay rate are different. The power-law fits

---

<sup>2</sup>In my experiences, condensate fraction itself is better parameter to extract temperature from an image rather than direct Gaussian fitting on the thermal wings because the estimated temperature varies depending on the ranges of the wings. And in this experiment, imaging sequence is not simple time-of-flight so we use condensate fraction of each image to obtain temperature of the sample. Here we simply assume ideal gas in harmonic trap, but more precise temperature can be estimated by using semi-ideal gas relation. We use the method in next chapter and find out that it gives roughly 10% lower temperature in our experimental ranges. References can be found in ch. 3.

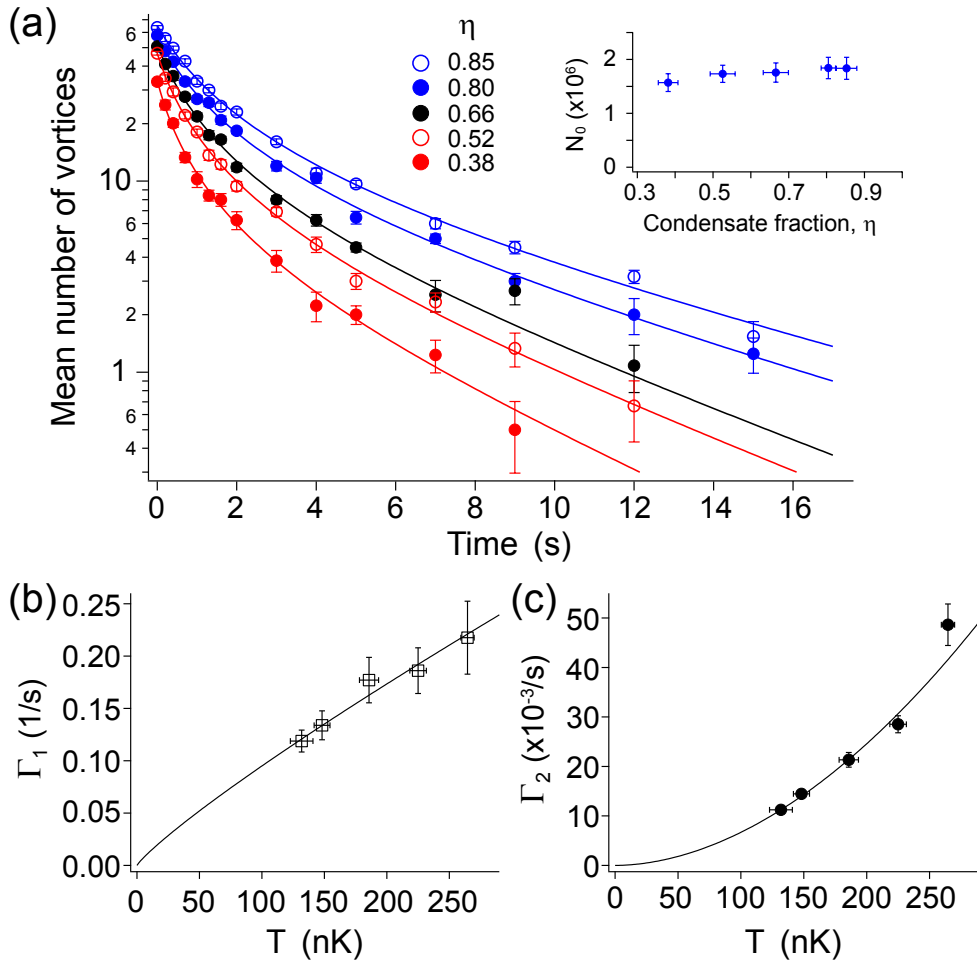


Figure 2.8: Temporal evolution of the vortex number. (a) Decay curves obtained for various condensate fractions  $\eta$ . Solid lines are fitting curves from the rate equation in Eq (1). The inset shows the atom number of the condensate,  $N_0$ , for each  $\eta$ . The data points for  $\eta = 0.80$  are identical to those in Fig. 2.4(a). Decay rates (b)  $\Gamma_1$  and (c)  $\Gamma_2$  as a function of the sample temperature  $T$ . Solid lines are power-law fits to the data with exponents of 0.87(20) and 1.88(12) for  $\Gamma_1$  and  $\Gamma_2$ , respectively.

to  $\Gamma_1(T)$  and  $\Gamma_2(T)$  give the exponents of 0.87(20) and 1.88(12), respectively, showing almost linear and quadratic dependence on the temperature. Here, we assume that the decay rates vanish at  $T = 0$ . The turbulent condensate may dynamically relax even at  $T = 0$ , i.e. without thermal atoms, but in the temperature range of our measurements,  $k_B T / \mu > 2$ , we presume that thermal dissipation effects primarily govern the decay dynamics.

The one-body decay rate  $\Gamma_1$  is predominantly determined from the decay behavior at low  $N_v$  which is mainly driven by the vortex drifting-out process. Thus, we might regard  $\Gamma_1$  as the thermal damping rate of a trapped BEC containing vortices, in particular, with zero net vorticity. In previous theoretical studies on nonequilibrium dynamics of trapped BECs, linear  $T$  dependence of the thermal damping rate was anticipated for low-energy excitations [32] and vortex lattice formation [33, 34]. However, its applicability to our measurements will require further theoretical work.

## Chemical potential

The vortex core size  $\xi \propto \mu^{-1/2}$  not only provides a characteristic length scale in the vortex dynamics but also defines the lower bound for the separation of two distinguishable vortex cores. The two-body decay rate  $\Gamma_2$  is associated with many-vortex effects including the vortex pair annihilation process and thus, it would be significantly affected by a change of the chemical potential.

To investigate the  $\mu$  dependence of  $\Gamma_2$ , we make two additional sets of measurements of  $\Gamma_2$  for the variations of the trapping frequency  $\omega_r$  and the total atom number  $N$ , respectively<sup>3</sup>. In each measurement set, the condensate frac-

---

<sup>3</sup>It is worthy to note that accurate measurement of  $\mu$  dependence of  $\Gamma_1$  is harder than that of  $\Gamma_2$  in our experimental setup. As there exists runaway cooling due to low trapping

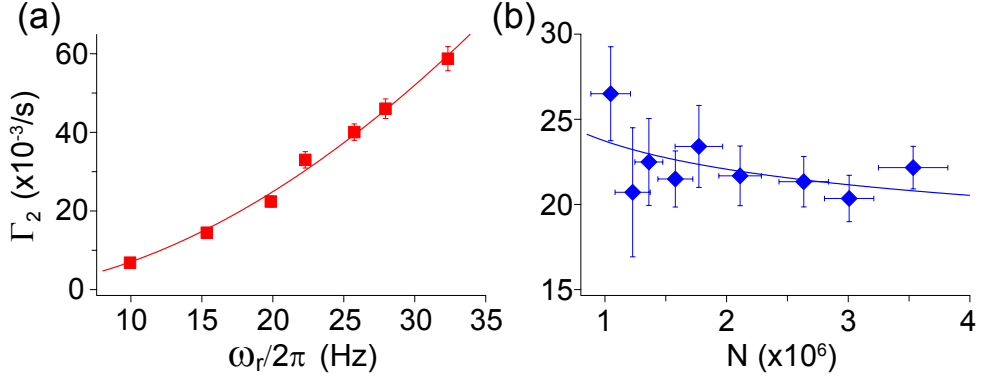


Figure 2.9: Decay rate  $\Gamma_2$  as a function of (a) the radial trapping frequency  $\omega_r$  ( $\eta \approx 0.80$  and  $N \approx 2.4 \times 10^6$ ) and (b) the total atom number  $N$  ( $\eta \approx 0.63$  and  $\omega_r/2\pi = 15$  Hz). The power-law fits (solid lines) give the exponents of (a) 1.82(9) and (b) -0.10(6) for  $\omega_r$  and  $N$ , respectively.

tion  $\eta$  is controlled to be fixed within a few %. For varying  $\omega_r$ , we adiabatically ramp the magnetic trapping potential during the repulsive laser beam being turned off. From the mean-field relations,  $T \propto (\omega_r^2 N)^{1/3}$  and  $\mu \propto (\omega_r^2 N)^{2/5}$  for a fixed  $\eta$ . The change in  $\mu$  entails a change in the spatial extent of the condensate as  $\mu = \frac{1}{2}m\omega_r^2 R^2$ . To decouple this effect, we define a local two-body decay rate as  $\gamma_2 \equiv (\pi R^2)\Gamma_2$ , crudely neglecting the details of the sample inhomogeneity. If  $\gamma_2$  is proportional to  $T^\alpha \mu^\beta$ , then we would have  $\Gamma_2 \propto \omega_r^{2+2\kappa/3} N^{\kappa/3}$ , where  $\kappa = \alpha + \frac{6}{5}(\beta - 1)$ .

Figure 2.9 shows the decay rate  $\Gamma_2$  as functions of  $\omega_r$  and  $N$ . The power-law fits to the data gives  $\Gamma_2 \propto \omega_r^{1.82(9)} N^{-0.10(6)}$  and the obtained exponents for  $\omega_r$  and  $N$  correspond to  $\kappa = -0.27(14)$  and  $-0.30(18)$ , respectively. It is remarkable to observe that the two measurement sets give a consistent result.

---

depth of the optical trap which is dramatically affected by condition of magnetic trap, long time dynamics of the condensate can be sensitive to such unexpected cooling.  $\Gamma_1$  could be influenced by it seriously since it is mainly determined from long time tail of nonexponential decay curve. Also, we find that  $\Gamma_1$  is a little more sensitive to how we choose the fitting range while  $\Gamma_2$  is not.

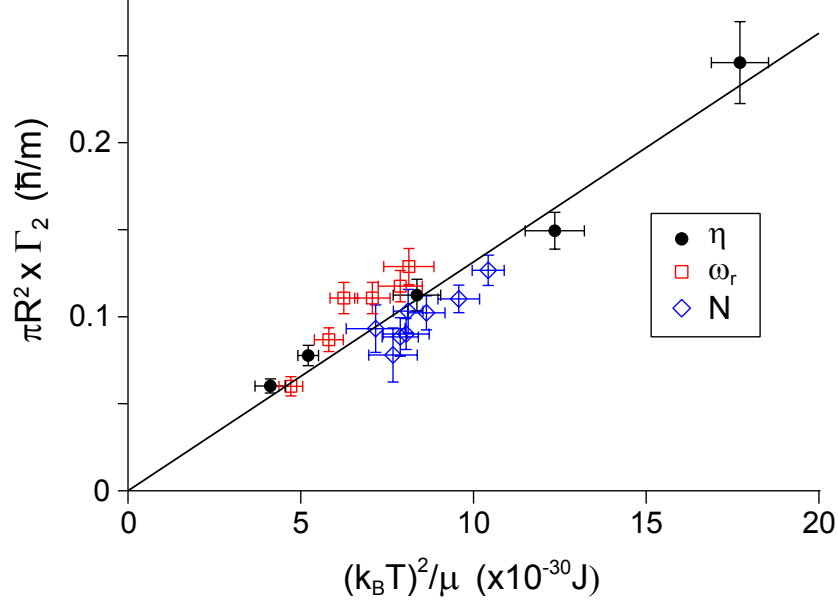


Figure 2.10: Local two-body decay rate  $\gamma_2 = (\pi R^2) \Gamma_2$  versus  $(k_B T)^2 / \mu$ . The solid line denotes a linear fit to the data. Black solid circles, red open squares and blue open diamonds correspond to the  $\Gamma_2$  data points in Fig. 2.8(c), Fig. 2.9(a), and Fig. 2.9(b), respectively.

With the previous result  $\alpha \approx 1.9$ ,  $\kappa \approx -0.3$  suggests  $\beta \approx -0.8$ . In Fig 2.10, we plot all the  $\Gamma_2$  measurements in the plane of  $\gamma_2$  and  $(k_B T)^2 / \mu$  and see that they collapse fairly well in a line.

Our analysis shows that the local two-body decay rate is a useful quantity for characterizing the relaxation of our system. An important but still open question is what is the exact physical mechanism determining  $\gamma_2$  in the relaxation dynamics. Let us consider the case where the two-body decay term in the rate equation purely originates from the vortex pair annihilation, assuming the vortex collision rate  $\gamma_c = (\hbar/2m)n_v$  as discussed for the system at high  $n_v$ . From the relation  $\Gamma_2 N_v = 2p_a \gamma_c$ , where  $p_a$  is the annihilation probability for a vortex-antivortex collision event, the decay rate  $\gamma_2$  would be expressed as

$\gamma_2 = (\hbar/m)p_a$ . Here, the observation of  $\gamma_2 \propto T^2/\mu$  has an interesting implication that the dimensionless quantity  $p_a$  is not determined as a function of the reduced temperature  $\tilde{T} = k_B T/\mu$ . This means that the vortex pair annihilation dynamics in our system cannot be explained with a pure 2D model which intrinsically preserves  $\tilde{T}$ -scaling behavior. The vortex line excitations, although their thermal excitations are suppressed, might play a role in the annihilation dynamics. Or the inhomogeneity of the trapped sample might be involved in a more intricate manner.

## 2.4 Summary and outlook

In summary, we have investigated thermal relaxation of superfluid turbulence in highly oblate Bose-Einstein condensates and presented possible evidences on the vortex-antivortex annihilation. We have characterized the relaxation of the turbulent condensate with the one-body and two-body decay rates of the vortex number. Our measurement results on the decay rates should provide a quantitative test on finite-temperature theories for vortex dynamics [29–31].

After publication of our work, there have been many theoretical studies focused on decaying superfluid turbulence in a homogeneous [35, 36] or trapped sample [37–39]. Stagg *et al.* [37] simulate the experiments using dissipative GPE and shows excellent agreement with our results. They were also able to count the number of vortex decayed due to pair annihilation or drifting out the condensate. Indeed they found that the pair annihilation events are highly probable and, when  $T = 0$ , the only possible decaying mechanism was pair annihilation which was well captured by our suggested rate equation, i.e., two-body term.

Nonetheless, there exist some numerical results [38, 39] that the decaying

number of vortices in 2D trapped quantum turbulence does not seem to follow two-body rate but rather four-body rate, which is different from our experimental results where the vortices decay slower than four-body rate. Moreover, it is very surprising that even the same four-body decaying rate can be interpreted differently depending on numerical simulation of each group [38, 39]. Where do those discrepancies come from? Perhaps exact and full experimental situation whose disordered vortices are generated by an oscillating condensate with respect to an obstacle beam, accompanying many sound waves as well as vortices [37] might have strong impact on decay of turbulence. Further investigations, both experimental and theoretical, will be necessary to more deeply understand decay of quantum turbulence in trapped BECs.

# Bibliography

- [1] V. L. Berezinskii, Sov. Phys. JETP. **34**, 610 (1972).
- [2] J. M. Kosterlitz and D. J. Thouless, J. Phys. C **6**, 1181 (1973); J. M. Kosterlitz *ibid* **7**, 1046 (1974).
- [3] W. H. Zurek, Nature (London) **317**, 505 (1985).
- [4] S. Nazarenko, and M. Onorato, J. Low Temp. Phys. **146**, 31 (2007).
- [5] M. Tsubota, M. Kobayashi, and H. Takeuchi, Phys. Rep. **522**, 191 (2013).
- [6] T. W. Neely, E. C. Samson, A. S. Bradley, M. J. Davis, and B. P. Anderson, Phys. Rev. Lett. **104**, 160401 (2010).
- [7] D. V. Freilich, D. M. Bianchi, A. M. Kaufman, T. K. Langin, and D. S. Hall, Science **329**, 1182 (2010).
- [8] Z. Hadzibabic, P. Krüger, M. Cheneau, B. Battelier, and J. Dalibard, Nature (London) **441**, 1118 (2006).
- [9] J. Choi, S. W. Seo, and Y. Shin, Phys. Rev. Lett. **110**, 175302 (2013).
- [10] R. H. Kraichnan and D. Montgomery, Rep. Prog. Phys. **43**, 547 (1980).

- [11] T.-L. Horng, C.-H. Hsueh, S.-W. Su, Y.-M. Kao, and S.-C. Gou, Phys. Rev. A **80**, 023618 (2009).
- [12] R. Numasato, and M. Tsubota, J. Low Temp. Phys. **158**, 415 (2010).
- [13] R. Numasato, M. Tsubota, and V. S. L'vov, Phys. Rev. A **81**, 063630 (2010).
- [14] B. Nowak, D. Sexty, and T. Gasenzer, Phys. Rev. B **84**, 020506(R) (2011).
- [15] B. Nowak, J. Schole, D. Sexty, and T. Gasenzer, Phys. Rev. A **85**, 043627 (2012).
- [16] T. Kusumura, M. Tsubota, and H. Takeuchi, J. Phys.: Conf. Ser. **400**, 012038 (2012).
- [17] J. Schole, B. Nowak, and T. Gasenzer, Phys. Rev. A **86**, 013624 (2012).
- [18] M. T. Reeves, B. P. Anderson, and A. S. Bradley, Phys. Rev. A **86**, 053621 (2012).
- [19] M. T. Reeves, T. P. Billam, B. P. Anderson, and A. S. Bradley, Phys. Rev. Lett. **110**, 104501 (2013).
- [20] P. M. Chesler, H. Liu, and A. Adams, Science **341**, 368 (2013).
- [21] T. W. Neely, A. S. Bradley, E. C. Samson, S. J. Rooney, E. M. Wright, K. J. H. Law, R. Carretero-González, P. G. Kevrekidis, M. J. Davis, and B. P. Anderson, Phys. Rev. Lett. **111**, 235301 (2013).
- [22] B. Jackson, N. P. Proukakis, C. F. Barenghi, and E. Zaremba, Phys. Rev. A **79**, 053615 (2009).

- [23] S. J. Rooney, P. B. Blakie, B. P. Anderson, and A. S. Bradley, Phys. Rev. A **84**, 023637 (2011).
- [24] A. C. White, C. F. Barenghi, and N. P. Proukakis, Phys. Rev. A **86**, 013635 (2012).
- [25] C. Rorai, K. R. Sreenivasan, and M. E. Fisher, Phys. Rev. B **88**, 134522 (2013).
- [26] S. Prabhakar, R. P. Singh, S. Gautam, and D. Angom, J. Phys. B: At. Mol. Opt. Phys. **46**, 125302 (2013).
- [27] J. Choi, S. Kang, S. W. Seo, W. J. Kwon, and Y. Shin, Phys. Rev. Lett. **111**, 245301 (2013).
- [28] S. Kang, J. Choi, S. W. Seo, W. J. kwon, and Y. Shin, Phys. Rev. A **91**, 013603 (2015).
- [29] H. E. Hall and W. F. Vinen, Proc. R. Soc. A **238**, 204 (1956).
- [30] M. Kobayashi and M. Tsubota, Phys. Rev. Lett. **97**, 145301 (2006).
- [31] N. G. Berloff and A. J. Youd, Phys. Rev. Lett. **99**, 145301 (2007).
- [32] P. O. Fedichev, G. V. Shlyapnikov, and J. T. M. Walraven, Phys. Rev. Lett. **80**, 2269 (1998).
- [33] A. A. Penckwitt, R. J. Ballagh, and C. W. Gardiner, Phys. Rev. Lett. **89**, 260402 (2002).
- [34] K. Kasamatsu, M. Tsubota, and M. Ueda, Phys. Rev. A **67**, 033610 (2003).
- [35] P. M. Chesler, A Lucas, arXiv:1411.2610 (2014).

- [36] Y. Du, C. Niu, Y. Tian, and H. Zhang, arXiv:1412.8417 (2014).
- [37] G. W. Stagg, A. J. Allen, N. G. Parker, and C. F. Barenghi, Phys. Rev. A **91**, 013612 (2015).
- [38] A. Cidrim, F. E. A. dos Santos, L. Galantucci, V. S. Bagnato, and C. F. Barenghi, arXiv:1507.03135 (2015).
- [39] A. J. Groszek, T. P. Simula, D. M. Paganin and K. Helmerson, arXiv:1511.06552 (2015).

# Chapter 3

## Mutual friction on quantized vortices in a BEC

This chapter concentrates on our experiments for measuring mutual friction coefficient  $\alpha$  which comes from friction between normal and superfluid components, using two co-rotating vortices at finite temperature BECs. The following paper contains the relevant experimental results and data.

- G. Moon\*, W. J. Kwon\*, H. Lee, and Y. Shin, “*Thermal friction on quantum vortices in a Bose-Einstein Condensate*”, Physical Review A **92**, 051601(R) (2015).

### 3.1 Introduction

At finite temperature a superfluid coexists with thermal excitations of the system and dissipation can occur in the superfluid dynamics via the interactions with the thermal component. In the framework of the two-fluid model, the

thermal dissipation was conceptualized as mutual friction between inviscid superfluid and viscous normal fluid, arising from the relative velocity of the two fluids in a nonequilibrium condition [1–3]. This concept has been successfully applied in the superfluid helium research [4, 5], in particular, enabling to phenomenologically describe the dissipative motion of quantized vortices in quantum turbulence [6, 7]. However, microscopic and quantitative understanding of the mutual friction on the vortex motion has not been completely established yet.

Atomic Bose-Einstein condensates (BECs), being a theoretically tractable superfluid system, provide an ideal setting for the microscopic study of dissipative vortex dynamics [8–10]. In previous BEC experiments, thermal damping of vortex states was investigated with rotating or turbulent condensates [11–14] but its direct comparison to theories was limited due to the complexity and uncertainty of the prepared vortex states. It is noted that even for the simple case where an axis-symmetric oblate BEC contains a single quantum vortex, the damping rate of the vortex state and its temperature dependence were predicted differently by many different theoretical approaches [15–24]. Because the thermal dissipation effect is generally small in typical sample conditions, its quantitative study requires to probe long-time dynamics of a precisely prepared vortex state. Recently, new experimental methods for vortex generation [25–27] and imaging [28–30] were demonstrated, opening up more controlled studies on few-vortex dynamics in BECs.

Here, we investigate the thermal dissipation in the vortex dynamics by measuring the long-time evolution of a corotating vortex pair in a highly oblate Bose-Einstein condensate. The corotating vortex pair is generated from the dissociation of a doubly charge vortex that is created at the center of con-

densate with a topological phase imprinting method [31–35]. When the two vortices undergo rapid pair orbiting motion, the dissipation effect is unambiguously revealed in the pair separation. The intervortex distance of the vortex pair monotonically increases over time and furthermore, it is observed that the pair separating rate is enhanced at higher temperatures, demonstrating the thermal nature of the dissipation. We describe the observed evolution of the pair separation with a point vortex model including longitudinal friction on the vortex motion and our measurement results show that the friction coefficient grows faster than linearly with the temperature. This work provides a clear set of experimental data for a quantitative test of microscopic theories of dissipative vortex dynamics.

### 3.1.1 Generation of a doubly charged vortex

Let's consider the situation where all spins are aligned along +z axis as in Fig. 3.1 (dotted arrows), where the center of the quadrupole magnetic trap is far above condensate (actually, since  $^{23}\text{Na}$  are in  $m_F = -1$  spin states, they are heading -z axis when the direction of the magnetic field is towards +z direction. But it is not important here.). By slowly moving the center of the magnetic trap towards -z direction such that it is finally far below the condensate, we can change adiabatically the directions of the spins to -z direction (solid arrows). The important thing is that the rotating process of each spin depends on the positions of the spins. Spins of atoms at the left side (labeled as 1) and the right side (labeled as 2) rotate in an opposite direction as in right picture of Fig. 3.1. This position dependent spin rotation generates phase difference in the wave function of the BEC.

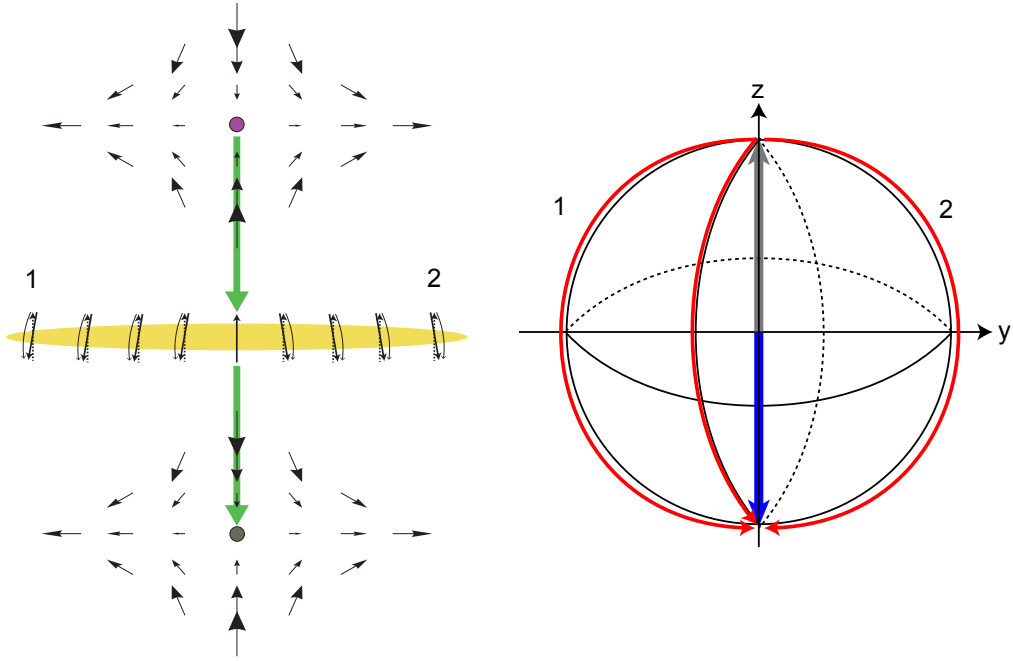


Figure 3.1: Generation of a doubly charged vortex using adiabatic spin rotation method. Magnetic quadrupole trap center is initially far above the condensate and it adiabatically penetrates the condensate (yellow). Spin initially heading upwards (dotted arrows) changes its direction (solid arrows) during the procedure. The right image describes that the different spin rotation direction (label 1 and 2) is directly connected to the geometrical phase accumulation due to Berry's phase. The corresponding spin positions are indicated in the left schematics.

To put it concretely, let's calculate the induced phase difference due to this spin rotation. Angular momentum operators of spin-1 states are given as

$$F_x = \frac{\hbar}{\sqrt{2}} \begin{pmatrix} 0 & 1 & 0 \\ 1 & 0 & 1 \\ 0 & 1 & 0 \end{pmatrix}, \quad F_y = \frac{i\hbar}{\sqrt{2}} \begin{pmatrix} 0 & -1 & 0 \\ 1 & 0 & -1 \\ 0 & 1 & 0 \end{pmatrix}, \quad F_z = \hbar \begin{pmatrix} 1 & 0 & 0 \\ 0 & 0 & 0 \\ 0 & 0 & -1 \end{pmatrix}. \quad (3.1)$$

The rotation operator  $D^1 = e^{-i\theta\hat{\mathbf{n}}\cdot\mathbf{F}/\hbar}$ , which rotates a vector by  $\theta$  in  $\hat{\mathbf{n}} = \hat{\mathbf{x}}\cos\phi + \hat{\mathbf{y}}\sin\phi$  direction, where  $\phi$  is an angle between  $\hat{\mathbf{n}}$  and x-axis, can

be obtained from the following relation (see any quantum mechanics textbook, e.g. Gottfried p. 126)

$$D^1 = 1 - iF_n \sin \theta - F_n^2(1 - \cos \theta). \quad (3.2)$$

Note that above relation is only appropriate for spin-1 case. Inserting  $F_n = F_x \cos \phi + F_y \sin \phi$  to the above equation, Eq. 3.2 reduces to

$$D^1 = \begin{pmatrix} \cos^2 \frac{\theta}{2} & \frac{-i}{\sqrt{2}} \sin \theta e^{-i\phi} & -\sin^2 \frac{\theta}{2} e^{-i2\phi} \\ \frac{-i}{\sqrt{2}} \sin \theta e^{+i\phi} & \cos \theta & \frac{-i}{\sqrt{2}} \sin \theta e^{-i\phi} \\ -\sin^2 \frac{\theta}{2} e^{+i2\phi} & \frac{-i}{\sqrt{2}} \sin \theta e^{+i\phi} & \cos^2 \frac{\theta}{2} \end{pmatrix}. \quad (3.3)$$

For  $\theta = \pi$ , which corresponds to the case where the direction of spin changes downwards after the rotation, there comes up phase factor  $e^{-i2\phi}$ . Due to this  $2\phi$ , where  $\phi$  ranges from 0 to  $2\pi$ , a doubly charged vortex is formed at the center of the condensate.

It can also be understood as an accumulation of phase due to Berry's phase. The phase difference between route 1 and route 2 in Fig. 3.1 is simply related to the solid angle covered by the two routes, which is  $2\pi$  in this case. (Generally, the result is  $-s\Omega$ , where  $s$  is spin and  $\Omega$  is solid angle. See any quantum mechanics textbook.)

## 3.2 Experiments

The experimental apparatus was described in our previous work [36,37]. We first generate a Bose-Einstein condensate of  $^{23}\text{Na}$  atoms in the  $|F = 1, m_F = -1\rangle$  state in a pancake-shaped optical dipole trap and we apply a magnetic quadrupole field  $\mathbf{B} = B_q(x\hat{x} + y\hat{y} - 2z\hat{z})/2 + B_z\hat{z}$ , where the symmetric axis of the magnetic

field is aligned to that of the optical trap. Including the Zeeman energy and the gravitational energy, the external potential for atoms is described as

$$\begin{aligned} V(x, y, z) = & \frac{m}{2}(\omega_x^2 x^2 + \omega_y^2 y^2 + \omega_z^2 z^2) \\ & + \frac{\mu_B B_q}{2} \sqrt{\frac{x^2 + y^2}{4} + (z - z_m)^2 + mgz}, \end{aligned} \quad (3.4)$$

where  $m$  is the atomic mass,  $(\omega_x, \omega_y, \omega_z) = 2\pi \times (5.7, 7.1, 690)$  Hz are the trapping frequencies of the optical potential,  $\mu_B$  is the Bohr magneton,  $z_m = B_z/B_q$  is the axial position of the zero-field point of the magnetic field, and  $g$  is the gravitational acceleration. Initially,  $B_q = 7.6$  G/cm and  $z_m = 130$   $\mu\text{m}$ .

Using a topological phase imprinting method [32, 33], we create a doubly charged vortex state. We linearly decrease the bias field  $B_z$  for 100 ms to move the zero-field point to  $z_m = -280$   $\mu\text{m}$ . While the zero-field point penetrates through the condensate, the atomic spin of the condensate adiabatically follows the local magnetic field. In this spin rotation process, the condensate acquires  $4\pi$  superfluid phase winding around its center due to the geometric Berry phase [31, 38]. After the field ramp, we decrease the field gradient  $B_q$  to 4.6 G/cm for 100 ms and simultaneously change  $B_z$  to make  $z_m = -100$   $\mu\text{m}$ . This field adjustment is to weaken the downward magnetic force. Otherwise, the magnetic force, together with the gravitational force, would significantly reduce the trap depth, leading to undesired evaporation cooling of the sample.

After the sample preparation, the transverse trapping frequency of the hybrid trap is  $\omega_r = \sqrt{\frac{\mu_B B_q}{8m|z_m|} + \omega_{x,y}^2} \approx 2\pi \times 19.7$  Hz, giving  $\omega_z/\omega_r \approx 35$ . The highly oblate geometry strongly suppresses vortex line excitations [39] and vortex dynamics in the condensate is effectively 2D. The transverse trapping potential is slightly anisotropic due to the weak elliptical optical potential and  $|\omega_x^2 - \omega_y^2|/(2\omega_r^2) \approx 0.02$ . The condensate contains  $N_0 \approx 3.4 \times 10^6$  atoms

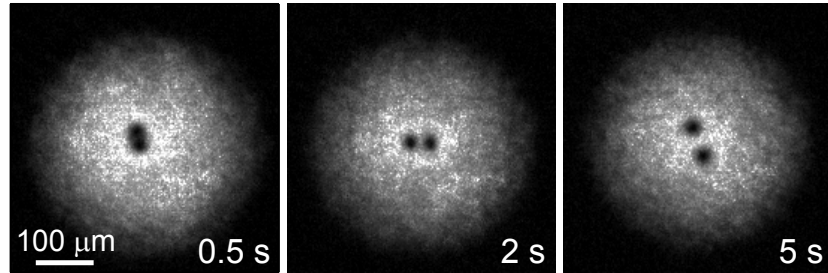


Figure 3.2: Corotating vortex pair in a Bose-Einstein condensate. Images of the condensate at various hold times after creating a doubly charged vortex. The doubly charge vortex splits into two singly charged vortices and the separation of the vortex pair increases, revealing the dissipation in the vortex dynamics.

and its radial extent is measured to be  $R \approx 76 \mu\text{m}$ . The healing length is  $\xi = \hbar/\sqrt{2m\mu} \approx 0.3 \mu\text{m}$  at the condensate center, where the chemical potential  $\mu = m\omega_r^2 R^2/2 \approx k_B \times 120 \text{ nK}$ . The sample temperature  $T$  is determined from the condensate fraction  $N_0/N$ , using the semi-ideal two-gas model [40,41]<sup>1</sup>, where  $N$  is the total atom number of the sample.

Vortices are detected by taking a time-of-flight absorption image of the condensate. In releasing the trapping potential, we first turn off the magnetic field and then release the optical potential, which was helpful to improve the visibility of the vortex core [14, 27]. In the imaging, the radial extent of the condensate increases by a factor of  $M = 1.95$  and the FWHM of the density-depleted core of a singly charged vortex is about  $10 \mu\text{m}$  in the center region of the condensate.

The doubly charged vortex splits into a pair of vortices [33, 34] and the two vortices becomes spatially resolved at hold time  $t \approx 0.5 \text{ s}$  after the phase imprinting (Fig. 3.2). We observe that the separation of the vortex pair increases over time, which reveals that dissipation occurs in the vortex dynamics. The

---

<sup>1</sup>We use Eq. 12 in ref. [40]

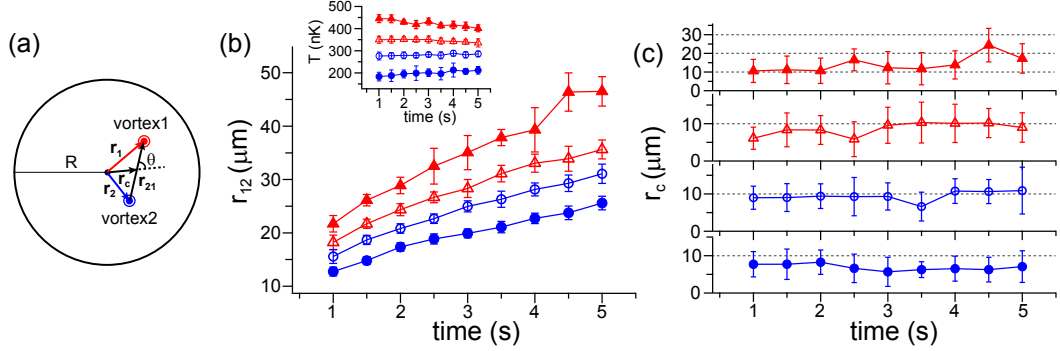


Figure 3.3: Evolution of the corotating vortex pair in a trapped Bose-Einstein condensate. (a) The vortex state is characterized with the separation distance  $r_{12}$  of the two vortices and the radial position  $r_c$  of the vortex pair center.  $R$  denotes the radius of the trapped condensate. Temporal evolutions of (b)  $r_{12}$  and (c)  $r_c$  for various sample temperatures. The atom number of the condensate was  $N_0 \approx 3.4 \times 10^6$  and  $R \approx 76 \mu\text{m}$ . The inset in (b) shows the variation of the sample temperature  $T$  during the evolution (Condensate fraction corresponding to each condition is 0.45, 0.59, 0.70, and 0.85.). Each data point was obtained by ten measurements of the same experiment and its error bar indicate the standard deviations of the measurements.

phase imprinting process causes breathing mode oscillations of the condensate because of the change of the transverse magnetic confinement. In this work, we restrict our study to the time period of  $t > 1$  s when the breathing mode excitations are sufficiently damped out [42].

We characterize the long-time, dissipative evolution of the corotating vortex pair with two configuration parameters: the intervortex distance  $r_{12} = |\mathbf{r}_2 - \mathbf{r}_1|$  and the radial position of the center of the vortex pair  $r_c = |\mathbf{r}_2 + \mathbf{r}_1|/2$  [Fig. 3.3(a)]. Assuming that the relative positions of the vortices is preserved in the condensate during the expansion in the imaging, we obtain the in-situ values of  $r_{12}$  and  $r_c$  by dividing the measured values from the image by the expansion factor  $M$ . Temporal evolutions of  $r_{12}$  and  $r_c$  for various sample temperature are displayed in Fig. 3.3(b) and (c), respectively. Note that in the

measurements, we controlled the sample temperature in the measurements by adjusting the total atom number  $N$  in such a way to maintain the condensate atom number  $N_0$ , thus preserving the spatial extent of the condensate.

It is observed that the increasing rate of the intervortex distance  $r_{12}$  as well as its initial value at  $t = 1$  s becomes higher at higher temperatures. This clearly demonstrates the thermal nature of the dissipation in the vortex dynamics. When the two vortices orbit around each other, it is known that energy dissipation dynamically occurs via sound emission from the accelerating vortices [46–49]. For  $r_{12} > 10 \mu\text{m}$  the wavelength of generated sound wave would be  $\lambda \sim 2\pi c_s/\omega_p \geq 1 \text{ mm}$ , where  $c_s = \sqrt{\mu/m}$  is the speed of sound. This value is much larger than the spatial size of the condensate and thus, we expect that the dissipation effect due to the sound emission is negligible in our measurements [45].

One remarkable feature in the measurement results is that fluctuations of the intervortex distance  $r_{12}$  are noticeably small although the pair center position  $r_c$  scatters in a relatively large area. This implies that the splitting process of the doubly quantized vortex was quite deterministic and furthermore, the subsequent separating dynamics of the vortex pair is not significantly affected by the pair center position. This is the crucial feature of our experiment, which allows the investigation of the long-time vortex dynamics in spite of technical imperfections in the initial state preparation.

## 3.3 Theoretical Model

### 3.3.1 Motion of vortices

Helmholtz vortex theorems in classical fluids say that “Vortex lines move with the fluid.” That is to say, a motion of a vortex is given by the fluid velocity in the vicinity of the vortex core (a familiar example is a vortex ring that self propels). This fact is still true for the quantum fluids. For example, a vortex dipole whose distance is  $d$  self propels and the speed is given by  $\hbar/md$ . It should be noted that this simple explanation on the motion of vortices are only appropriate when the density of the superfluid is constant.

Another way to treat the motion of the vortex is using the force acting the vortex core [50]. Without any dissipation and density gradient, Magnus force is the only force acting on the vortex and it is given by  $\mathbf{F}_M = \rho_s \mathbf{k} \times (\mathbf{v}_L - \mathbf{v}_s)$ , where  $\rho_s$  is the density of the superfluid,  $\mathbf{k}$  is vorticity vector, and  $\mathbf{v}_L$  and  $\mathbf{v}_s$  is velocity of a vortex and a superfluid, respectively. Since we can treat the vortex core as massless [50], total forces acting on a vortex core should vanish, i.e.  $\mathbf{F}_{\text{total}} = \mathbf{F}_M = 0$  so that  $\mathbf{v}_L = \mathbf{v}_s$ . This exactly means that the vortex moves with the fluid and its velocity is given by the background fluid velocity. For the vortex dipole,  $\mathbf{v}_s$  at the vortex is given by the other antivortex located at the distance  $d$  from it and their velocity vectors are same. For the case of two corotating vortices, however, velocity vectors of two vortices are exactly opposite so that they orbit around each other.

When  $\rho_s$  is not homogeneous over the space, there can be another force acting on a vortex due to density gradient, which originates from the fact that the energy of the vortex is proportional to  $\rho_s$ . This force  $\mathbf{F}_g \propto -\nabla \rho_s$  and  $\mathbf{F}_M$  balance to zero, i.e.,  $\mathbf{F}_M + \mathbf{F}_g = 0$ . This leads to  $\mathbf{v}_L \neq \mathbf{v}_s$ , where there exists an

additional velocity term perpendicular  $\nabla\rho_s$  (i.e.,  $\mathbf{k} \times \nabla\rho_s$ ).

For the case of finite temperature BECs, a frictional force  $\mathbf{F}_d$  is exerted on a quantized vortices and it balances with  $\mathbf{F}_M$ . It will be discussed below.

### 3.3.2 Dynamics of corotating vortices in a harmonic trap

The non-dissipative dynamics of a corotating vortex pair in a harmonic potential was investigated in recent experiments [30] and it was shown that the vortex motion is well described by a point vortex model [43, 44]. In a trapped condensate, the velocity of the  $i$ th vortex ( $i, j = 1, 2$ ) is given by

$$\mathbf{v}_i^0 = \Omega(r_i)(\hat{\mathbf{z}} \times \mathbf{r}_i) + \frac{b}{2mr_{ji}^2}(\hat{\mathbf{z}} \times \mathbf{r}_{ji}), \quad (3.5)$$

where  $\mathbf{r}_i$  is the vortex position with respect to the condensate center and  $\mathbf{r}_{ji} = \mathbf{r}_i - \mathbf{r}_j$ . It should be noted that this equation is a little different from the case of vortices trapped in a disk trap. In a disk trap, when there's a single vortex located off-center, whose position is  $\mathbf{r}$  in the trap, its precession frequency around the trap center is produced by a velocity field of an image antivortex outside the trap, located at  $(R/r)^2\mathbf{r}$ , where  $R$  is a radius of the disk. So the precession frequency  $\Omega = v/r$  is given by  $\hbar/m(R^2 - r^2)$ . The direction of precession is same as the circulation of the vortex in the trap, i.e., an anticlockwise vortex precesses in anticlockwise direction.

The boundary condition for any fluid is given by continuity equation  $\rho_s \mathbf{v}_n = 0$ , where  $\mathbf{v}_n$  is normal component of the velocity field. This condition with constant density of the fluid (regardless of super or classical) leads to  $\mathbf{v}_n = 0$ . And this boundary condition can be satisfied by locating an imaginary vortex outside the disk as mentioned above. For the case of harmonically trapped condensate, however, such boundary condition is automatically satisfied since

$\rho_s = 0$ , and the vortex motion is explained without any image vortex. The above Eq. (3.5) should be understood in this way and the details are explained in a review paper of Fetter [45].

The first term of Eq. (3.5) corresponds to the precession around the trap center due to the axisymmetric, inhomogeneous density distribution of the condensate. For a pancake-shaped condensate,  $\Omega(r) = \Omega_0/(1 - r^2/R^2)$  with  $\Omega_0 = \frac{3\hbar}{2mR^2} \ln(\frac{R}{\xi})$  [45]. The second term is the superfluid flow field generated by the other vortex, which drives the vortex pair to orbit around each other. The parameter  $b$  is the modification factor of the interaction strength between the vortices with respect to the homogeneous case and  $b = 1.35$  for two vortices in a harmonic trap [43]. In the symmetric case with  $\mathbf{r}_1 = -\mathbf{r}_2$ , the vortex pair undergoes a circular orbiting motion whose angular frequency is  $\omega_p = \Omega(\frac{r_{12}}{2}) + b\hbar/(mr_{12}^2)$ .

To elucidate the characteristics of the observed dissipative dynamics of the vortex pair, we perform a numerical study based on the point vortex model in Eq. (3.5) by including longitudinal friction on the vortex motion [18, 19, 24, 49]. The friction is presumed to be proportional to the relative velocity of the superfluid to the thermal component of the system [1, 3]. More specifically, a frictional force  $\mathbf{F}_d$  is given by (for 2D case)

$$\mathbf{F}_d = m\rho_s \alpha \mathbf{k} \times [\hat{\mathbf{k}} \times (\mathbf{v}_s - \mathbf{v}_n)] + m\rho_s \alpha' \hat{\mathbf{k}} \times (\mathbf{v}_s - \mathbf{v}_n), \quad (3.6)$$

where  $\hat{\mathbf{k}}$  is a unit vector along vorticity vector,  $\alpha$  and  $\alpha'$  are longitudinal and transverse mutual friction coefficient (both dimensionless), respectively. Here, we assume small  $\alpha'$  and ignore the second term of Eq. 3.6, which is a common first order approximation. Here we assume a stationary thermal cloud, i.e.,  $\mathbf{v}_n = 0$ . Note that our vortex creation method is not effective to the thermal cloud

and the slight anisotropy of the transverse trapping potential would help lock the thermal cloud to the trap [20].

The friction force is balanced with a Magnus force that arises from a velocity change in the vortex motion so that

$$\mathbf{F}_d + \mathbf{F}_M = m\rho_s\alpha\mathbf{k} \times [\hat{\mathbf{k}} \times (\mathbf{v}_s - \mathbf{v}_n)] + m\rho_s\mathbf{k} \times (\mathbf{v}_L - \mathbf{v}_s) = 0, \quad (3.7)$$

and the resultant motion of the vortex is given by ( $\hat{\mathbf{k}} = \hat{\mathbf{z}}$  case)

$$\mathbf{v}_i = \mathbf{v}_i^0 - \alpha\hat{\mathbf{z}} \times \mathbf{v}_i^0, \quad (3.8)$$

Because the local density of the thermal component varies over the trapped sample,  $\alpha$  should be position-dependent but we ignore it in the current model.

Figure 3.4 shows numerical simulation results of the dissipative point vortex model for our experimental parameters and with  $\alpha = 0.02$ . In the case with  $r_c = 0$ , the two vortices show symmetric trajectories spiraling out of the condensate [Fig. 3.4(a)]. When the two vortices becomes asymmetric with  $r_c \neq 0$ , their trajectories appear complicated [Fig. 3.4(b) and (c)] but both of  $r_{12}$  and  $r_c$  show simple growth behavior with small oscillations [Fig. 3.4(d) and (e)], indicating that they essentially follows epicyclic trajectories, i.e., a rapid pair orbiting motion superposed upon a slow precession of the pair center. Apart from the small oscillations, the evolution of  $r_{12}$  is almost identical to that in the symmetric case with  $r_c = 0$  regardless of the variation of  $r_c$  [Fig. 3.4(d)]. This seems to explain the experimental observation of small fluctuations in  $r_{12}$  despite relatively large scattering of  $r_c$ .

The oscillations of  $r_{12}$  and  $r_c$  originates from the radial dependence of the precession frequency  $\Omega(r)$ , i.e.,  $\Omega(r_1) \neq \Omega(r_2)$ . When the two vortices are located near the condensate center, i.e.,  $r_i \ll R$ , the precession frequency  $\Omega \approx \Omega_0$ ,

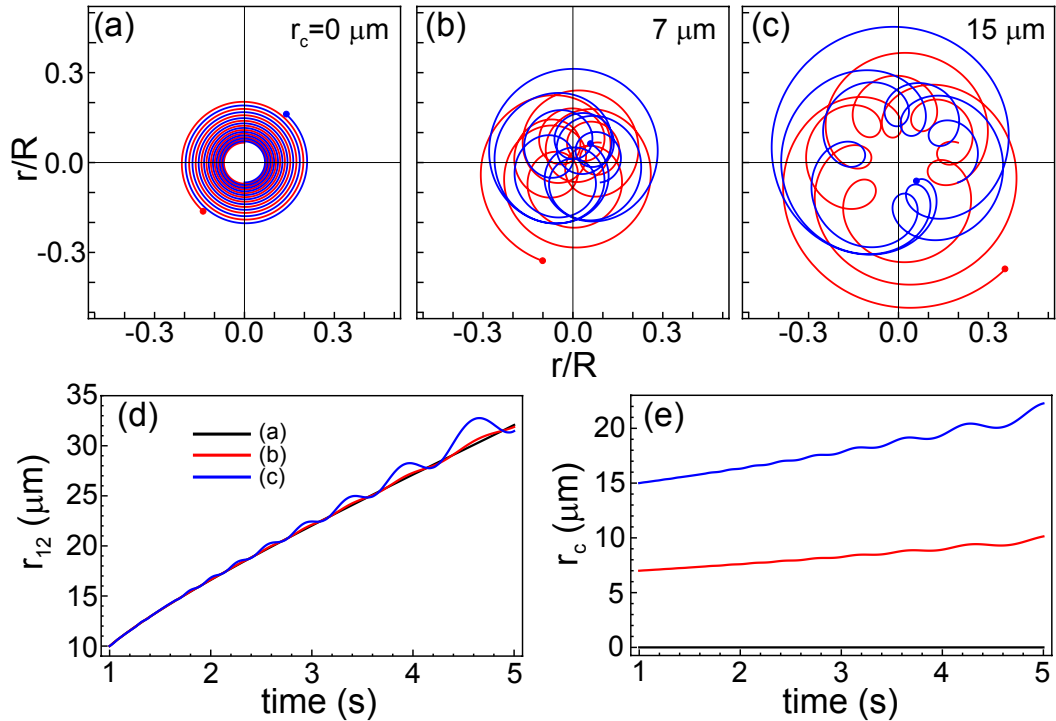


Figure 3.4: Numerical simulation of the dissipative point-vortex model. (a)-(c) Trajectories of the two vortices for various initial conditions at  $t = 1 \text{ s}$ :  $r_{12} = 10 \mu\text{m}$ ,  $\theta = \pi/2$ , and  $r_c = 0 \mu\text{m}$ ,  $7 \mu\text{m}$ ,  $15 \mu\text{m}$  in (a),(b), and (c), respectively. The friction coefficient  $\alpha = 0.02$ ,  $R = 76 \mu\text{m}$ , and  $\Omega_0/2\pi = 0.64 \text{ Hz}$ . Evolutions of  $r_{12}$  (d) and  $r_c$  (e) for the vortex trajectories in (a)-(c).

rendering the motions of  $r_{12}$  and  $r_c$  effectively decoupled as

$$\frac{d\mathbf{r}_{12}}{dt} = \omega_{p0} [\alpha + \hat{\mathbf{z}} \times] \mathbf{r}_{12} \quad (3.9)$$

$$\frac{d\mathbf{r}_c}{dt} = \Omega_0 [\alpha + \hat{\mathbf{z}} \times] \mathbf{r}_c, \quad (3.10)$$

where  $\omega_{p0} = \Omega_0 + b\hbar/(mr_{12}^2)$ . This means that in the center region limit the friction coefficient can be reliably determined from the evolution of the pair separation  $r_{12}$ .

### 3.4 Determination of Mutual friction $\alpha$

Motivated by this finding, we determine the friction coefficient  $\alpha$  by fitting the evolution curve of  $r_{12}(t)$  obtained from Eq. (3.9) to our experiment data (Fig. 3.5). Analytical form of  $r_{12}(t)$  can be obtained by solving the following equation

$$\dot{r}_{12} = \frac{d\mathbf{r}_{12}}{dt} \cdot \hat{\mathbf{r}}_{12} = \omega_{p0}\alpha r_{12} = \alpha [\Omega_0 r_{12} + b\hbar/(mr_{12})], \quad (3.11)$$

which gives a solution of  $r_{12}(t) = \frac{\sqrt{-b\hbar/m + e^{2\Omega_0(t\alpha+c)}}}{\sqrt{\Omega_0}}$ . Our analysis was restricted to the data points in the range of  $20 \mu\text{m} < r_{12} < 33 \mu\text{m}$ , where  $r_c$  is less than  $20 \mu\text{m}$  and so  $r_i/R \leq 0.4$ , marginally satisfying the center-region approximation. The resultant value of  $\alpha$  increases from 0.01 to 0.03 for the temperature range of  $200 \text{ nK} < T < 450 \text{ nK}$ . We see that the increasing rate of  $\alpha$  becomes faster at high  $T$ . This seems to support the recent numerical results of Berloff and Youd [9], and Jackson et al. [19], where quadratic  $T$ -dependence was predicted in contrast to the linear  $T$ -dependence typically predicted in the low-temperature limit [15, 17, 51]. Moreover, we try to fit the data with power-law function and the best power law fitting to the data tells us that exponent is 1.5(2), assuming

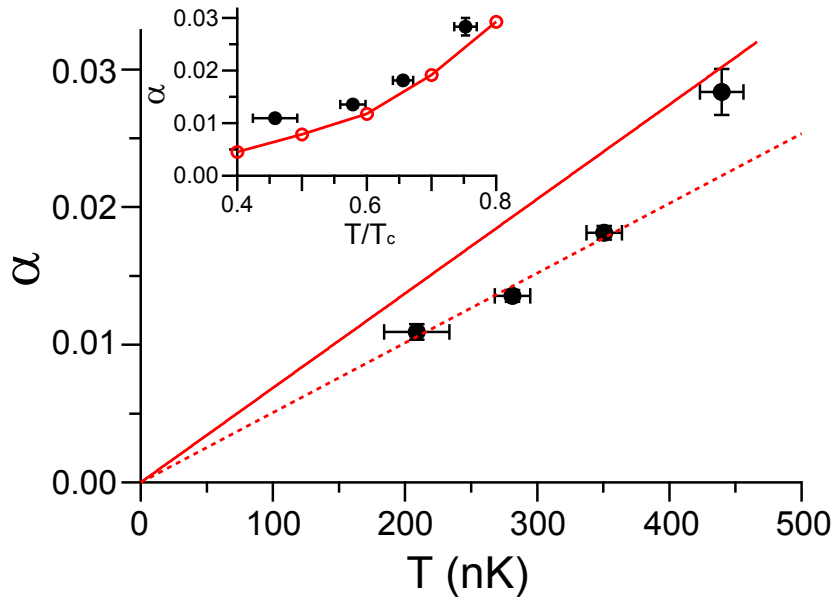


Figure 3.5: Friction coefficient  $\alpha$  as a function of the temperature  $T$ .  $\alpha$  was determined using Eq. 3.11 from the experimental data in the restricted region of  $20 \mu\text{m} < r_{12} < 33 \mu\text{m}$ . The dashed line is a linear fit to the three lowest- $T$  data points with  $\alpha = 0$  at  $T = 0$ . The inset shows the same data as a function of the relative temperature  $T/T_c$ , where  $T_c$  is the critical temperature of the sample. The open diamonds are the theoretical predictions from Jackson et al. [19].

$\alpha = 0$  at  $T=0$  nK. I'd like to warn that the exponent value should not be taken seriously because there are only 4 data points and we don't even know  $\alpha$  is exactly zero at  $T=0$  nK in our experimental conditions where the small dissipative motion can be produced due to anisotropy of the system, where the rotational symmetry is broken. The value of  $\alpha$  itself is more important here.

Remarkably, when we plot  $\alpha$  as a function of the relative temperature  $T/T_c$ , where  $T_c$  is the critical temperature of the sample, we find our result in quite good quantitative agreement with the theoretical prediction of Jackson et al. [19] (Fig. 3.5 inset). The slight upward deviation of the data might be attributed to the dissipation due to the sound emission as well as the trap

anisotropy [17, 20, 46]. However, it should be mentioned that our analysis neglects possible temperature dependence of the  $b$  parameter and the precession frequency  $\Omega$ . It was indeed shown that the precession frequency  $\Omega$  has positive temperature dependence [19, 22, 52, 53], which would lead to overestimation of  $\alpha$  in our analysis. The temperature dependence of  $b$  and  $\Omega$  is also intricately related with the transverse friction that is not considered in our point vortex model [8, 9, 18, 19]. Further elaborated analysis including these effects as well as the realistic experimental condition would solidify the quantitative interpretation of our measurement results.

### 3.5 Summary

The mutual friction acting on a quantized vortex due to interaction between thermal and superfluid component is very important in superfluid turbulence community which is one of ongoing issues. We have investigated the thermal dissipation in the dynamics of a corotating vortex pair in a trapped Bose-Einstein condensate. Based on the dissipative point vortex model, we determined the mutual friction coefficient  $\alpha$  from the temporal evolution of the intervortex distance of the vortex pair and investigated its temperature dependence. We expect that the quantitative information on the thermal dissipation will give direct insight into the results of our previous experiment in ch. 2 [14] where the relaxation of superfluid turbulence was investigated in terms of the decay rate of the vortex number of turbulent BECs. The relation between  $\alpha$  and decay of vortices, such as a vortex-antivortex pair annihilation process, is remained as an interesting question on 2D quantum turbulence.

# Bibliography

- [1] H. E. Hall and W. F. Vinen, Proc. R. Soc. A **238**, 204 (1956); **238**, 215 (1956).
- [2] C. F. Barenghi, R. J. Donnelly, and W. F. Vinen, J. Low Temp. Phys. **52**, 189 (1983).
- [3] K. W. Schwarz, Phys. Rev. B **31**, 5783 (1985); **38**, 2398 (1988).
- [4] R. J. Donnelly, *Quantized Vortices in Helium II* (Cambridge University Press, Cambridge, 1991).
- [5] C. F. Barenghi, R. J. Donnelly, and W. F. Vinen, *Quantized Vortex Dynamics and Superfluid Turbulence* (Springer, Berlin, 2001).
- [6] R. Hänninen and A. W. Baggaley, Proc. Natl. Acad. Sci. U.S.A. **111**, 4667 (2014).
- [7] N. G. Berloff, M. Brachet, and N. P. Proukakis, Proc. Natl. Acad. Sci. U.S.A. **111**, 4675 (2014).
- [8] M. Kobayashi and M. Tsubota, Phys. Rev. Lett. **97**, 145301 (2006).
- [9] N. G. Berloff and A. J. Youd, Phys. Rev. Lett. **99**, 145301 (2007).

- [10] A. C. White, B. P. Andreson, and V. S. Bagnato, Proc. Natl. Acad. Sci. U.S.A. **111**, 4719 (2014).
- [11] P. Rosenbusch, V. Bretin, and J. Dalibard, Phys. Rev. Lett. **89**, 200403 (2002).
- [12] J. R. Abo-Shaeer, C. Raman, and W. Ketterle, Phys. Rev. Lett. **88**, 070409 (2002).
- [13] T. W. Neely, A. S. Bradley, E. C. Samson, S. J. Rooney, E. M. Wright, K. J. H. Law, R. Carretero-González, P. G. Kevrekidis, M. J. Davis, B. P. Anderson, Phys. Rev. Lett. **111**, 235301 (2013).
- [14] W. J. Kwon, G. Moon, J. Choi, S. W. Seo, and Y. Shin, Phys. Rev. A **90**, 063627 (2014).
- [15] P. O. Fedichev and G. V. Shlyapnikov, Phys. Rev. A **60**, R1779(R) (1999).
- [16] H. Schmidt, K. Góral, F. Floegel, M. Gajda, and K. Rzażewski, J. Opt. B: Quantum Semiclass. Opt. **5**, S96 (2003).
- [17] R. A. Duine, B. W. A. Leurs, and H. T. C. Stoof, Phys. Rev. A **69**, 053623 (2004).
- [18] E. J. M. Madarassy and C. F. Barenghi, J. Low Temp. Phys. **152**, 122 (2008).
- [19] B. Jackson, N. P. Proukakis, C. F. Barenghi, and E. Zaremba, Phys. Rev. A **79**, 053615 (2009).
- [20] T. M. Wright, A. S. Bradley, and R. J. Ballagh, Phys. Rev. A **81**, 013610 (2010).

- [21] S. J. Rooney, A. S. Bradley, and P. B. Blakie, Phys. Rev. A **81**, 023630 (2010).
- [22] A. J. Allen, E. Zaremba, C. F. Barenghi, and N. P. Proukakis, Phys. Rev. A **87**, 013630 (2013).
- [23] S. Gautam, A. Roy, and S. Mukerjee, Phys. Rev. A **89**, 013612 (2014).
- [24] D. Yan, R. Carretero-González, D. J. Frantzeskakis, P. G. Kevrekidis, N. P. Proukakis, and D. Spirn, Phys Rev A **89**, 043613 (2014).
- [25] T. W. Neely, E. C. Samson, A. S. Bradley, M. J. Davis, and B. P. Anderson, Phys. Rev. Lett. **104**, 160401 (2010).
- [26] J. A. Seman, E. A. L. Henn, M. Haque, R. F. Shiozaki, E. R. F. Ramos, M. Caracanhas, P. Castilho, C. C. Branco, P. E. S. Tavares, F. J. Poveda-Cuevas, G. Roati, K. M. F. Magalhães, and V. S. Bagnato, Phys. Rev. A **82**, 033616 (2010).
- [27] W. J. Kwon, S. W. Seo, and Y. Shin, Phys. Rev. A **92**, 033613 (2015).
- [28] D. V. Freilich, D. M. Bianchi, A. M. Kaufman, T. K. Langin, D. S. Hall, Science **329**, 1182 (2010).
- [29] S. Middelkamp, P. J. Torres, P. G. Kevrekidis, D. J. Frantzeskakis, R. Carretero-González, P. Schmelcher, D. V. Freilich, and D. S. Hall, Phys. Rev. A **84**, 011605(R) (2011)
- [30] R. Navarro, R. Carretero-González, P. J. Torres, P. G. Kevrekidis, D. J. Frantzeskakis, M. W. Ray, E. Altuntas, and D. S. Hall, Phys. Rev. Lett. **110**, 225301 (2013).

- [31] T. Isoshima, M. Nakahara, T. Ohmi, and K. Machida, Phys. Rev. A **61**, 063610 (2000).
- [32] A. E. Leanhardt, A. Görlitz, A. P. Chikkatur, D. Kielpinski, Y. Shin, D. E. Pritchard, and W. Ketterle, Phys. Rev. Lett. **89**, 190403 (2002).
- [33] Y. Shin, M. Saba, M. Vengalattore, T. A. Pasquini, C. Sanner, A. E. Leanhardt, M. Prentiss, D. E. Pritchard, and W. Ketterle, Phys. Rev. Lett. **93**, 160406 (2004).
- [34] J. A. M. Huhtamäki, M. Möttönen, T. Isoshima, V. Pietilä, and S. M. M. Virtanen, Phys. Rev. Lett. **97**, 110406 (2006).
- [35] T. Isoshima, M. Okano, H. Yasuda, K. Kasa, J. A. M. Huhtamäki, M. Ku-makura, and Y. Takahashi, Phys. Rev. Lett. **99**, 200403 (2007).
- [36] J. Choi, W. J. Kwon, M. Lee, H. Jeong, K. An, and Y. Shin, New J. Phys. **14**, 053013 (2012).
- [37] J. Choi, S. Kang, S. W. Seo, W. J. Kwon, and Y. Shin, Phys. Rev. Lett. **111**, 245301 (2013).
- [38] M. Berry, Proc. R. Soc. A **392**, 45 (1984).
- [39] S. J. Rooney, P. B. Blakie, B. P. Anderson, and A. S. Bradley, Phys. Rev. A **84**, 023637 (2011).
- [40] M. Naraschewski and D. M. Stamper-Kurn, Phys. Rev. A **58**, 2423 (1998).
- [41] F. Gerbier, J. H. Thywissen, S. Richard, M. Hugbart, P. Bouyer, and A. Aspect, Phys. Rev. A **70**, 013607 (2004).

- [42] At  $t = 0.5$  s, the amplitude of the breathing mode oscillations was measured to be about 5% of the condensate radius and its damping rate was about  $2.5 \text{ s}^{-1}$ .
- [43] S. Middelkamp, P. G. Kevrekidis, D. J. Frantzeskakis, R. Carretero-González, and P. Schmelcher, Phys. Rev. A **82**, 013646 (2010).
- [44] P. J. Torres, P. G. Kevrekidis, D. J. Frantzeskakis, R. Carretero-González, P. Schmelcher, D. S. Hall, Phys. Lett. A **375**, 3044 (2011).
- [45] A. L. Fetter and A. A. Svidzinsky, J. Phys. Condens. Matter **13**, R135 (2001).
- [46] E. Lundh and P. Ao, Phys. Rev. A **61**, 063612 (2000).
- [47] N. G. Parker, N. P. Proukakis, C. F. Barenghi, and C. S. Adams, Phys. Rev. Lett. **92**, 160403 (2004).
- [48] C. F. Barenghi, N. G. Parkder, N. P. Proukakis and C. S. Adams, J. Low Temp. Phys. **138**, 629 (2005).
- [49] T. P. Billam, M. T. Reeves, and A. S. Bradley, Phys. Rev. A **91**, 023615 (2015).
- [50] C. F. Barenghi, R. J. Donnelly, and W. F. Vinen, *Quantized Vortex Dynamics and Superfluid Turbulence*, (Springer, 2001). (See Introduction part.)
- [51] A. A. Penckwitt, R. J. Ballagh, and C. W. Gardiner, Phys. Rev. Lett. **89**, 260402 (2002).
- [52] T. Isoshima, J. Huhtamäki, and M. M. Salomaa, Phys. Rev. A **69**, 063601 (2004).

[53] B. G. Wild and D. A. W. Hutchinson, Phys. Rev. A **80**, 035603 (2009).

# Chapter 4

## Critical velocity for vortex shedding in a BEC

Previous chapters 1 and 2 focus on the experiments on superfluid turbulence and mutual friction. From now on, I am going to handle with vortex shedding dynamics in a Bose condensed superfluid. As a first step, this chapter describes critical velocity for creating a vortex dipole in a highly oblate BEC with a moving repulsive Gaussian beam. The issues on critical velocity in a BEC have long been dealt with both theoretists and experimentalists since the first generation of BEC, but not yet settled. Therefore, we revisit and do systematic studies on this problem.

The main contents and results are contained in the following paper.

- W. J. Kwon, G. Moon, S. W. Seo, and Y. Shin, “*Critical velocity for vortex shedding in a Bose-Einstein condensate*”, Physical Review A **91**, 053615 (2015).

## 4.1 Introduction

A superfluid flows without friction but it becomes dissipative above a certain critical velocity  $v_c$  via generating its elementary excitations such as phonons and vortices. The Landau criterion provides a conventional energetic consideration to determine the critical velocity, stating  $v_c = \min[\epsilon(p)/p]$  [1], where  $\epsilon(p)$  is the energy of an elementary excitation of momentum  $p$ . For a homogeneous system, the Landau critical velocity is equal to the speed of sound  $c_s$ . However, dynamic response of a superfluid flow is significantly sensitive to the boundary condition (boundary of the obstacle) of the system, and hence, quantitative understanding of the critical velocity has been a challenging task in the study of superfluidity.

One of the paradigmatic situations considered in fluid mechanics is a two-dimensional (2D) flow past a circular cylinder. For an incompressible flow, the local velocity is increased by a factor of 2 at the lateral sides of the cylinder [2] and the local Landau supersonic criterion suggests a critical velocity of  $v_c = 0.5c_s$  that is independent of the radius  $R$  of the cylinder. Theoretical studies showed that the onset of dissipation involves generating a counter-rotating vortex pair [3, 4]. More rigorous calculations, taking into account the compressibility of superfluid and quantum pressure near the boundary of the cylinder, predicted that the critical velocity converges to  $v_c = 0.37c_s$  in the large cylinder limit  $R \gg \xi$  [5–9], where  $\xi$  is the superfluid healing length. Experimental verification of the predictions on  $v_c/c_s$  is highly desirable.

In previous ultracold atom experiments, a similar situation was investigated by stirring superfluid samples with a repulsive laser beam [10–15]. The existence of finite critical velocities [10, 11, 14] and generation of vortex dipoles [12,

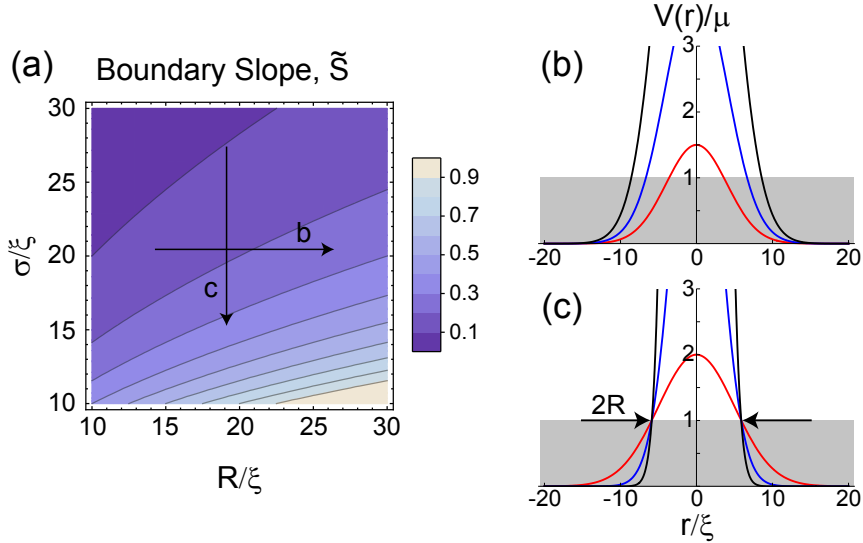


Figure 4.1: Soft boundary of the optical obstacle formed by a repulsive Gaussian potential  $V(r) = V_0 \exp(-2r^2/\sigma^2)$ . (a) Normalized potential slope at the obstacle boundary  $\tilde{S} = (\xi/\mu)|dV/dr|_{r=R}$  as a function of  $\sigma/\xi$  and  $R/\xi$ , where  $\mu$  and  $\xi$  is the chemical potential and the healing length of the condensate, respectively, and  $R$  is the obstacle radius such that  $V(R) = \mu$ . The boundary becomes stiffer as (b)  $R/\xi$  becomes larger or (c)  $\sigma/\xi$  decreases. The corresponding trajectories are indicated by the arrow lines in (a).

[13, 15] were successfully demonstrated<sup>1</sup>. However, the measured values of  $v_c/c_s$  widely ranged from 0.1 to 0.45, which did not allow a quantitative study of the homogeneous 2D problem. Theoretical investigations showed that the inhomogeneous density distribution of a trapped sample [16–18], three-dimensional (3D) vortex dynamics [19–21], or the manner of stirring [13, 16, 21–23] should be critical in the measurements. Recently, the vortex shedding dynamics was also investigated experimentally with polariton superfluids flowing past stationary defects [24, 25].

---

<sup>1</sup>It is natural to ask why the generation of vortices were only clearly detected at some specific experimental conditions. Actually, this does not seem to be simply solved. I guess that the oblate trap geometry would've been important to detect long-lived and clear vortices.

Here, we systematically study the critical velocity for vortex shedding in a Bose-Einstein condensate with a repulsive Gaussian potential. We measure the critical velocity as a function of the barrier height  $V_0$  of the potential over a wide range of the beam width,  $10 < \sigma/\xi < 55$ . In particular, in order to address the 2D homogeneous regime, we employ spatially large and highly oblate condensates, ensuring vortex dynamics in 2D.

The key difference of a Gaussian potential from a hard cylinder is its soft boundary. A Gaussian potential,  $V(r) = V_0 \exp(-2r^2/\sigma^2)$ , produces a density-depleted hole in the condensate when  $V_0 > \mu$ , where  $\mu$  is the chemical potential of the condensate. The radius of the hole and the potential slope at the hole boundary are given as

$$R = \sigma \sqrt{\ln(V_0/\mu)/2} \quad (4.1)$$

$$S = -\frac{dV}{dr} \Big|_{r=R} = 4\mu R/\sigma^2, \quad (4.2)$$

respectively. In comparison to the case with a hard cylinder, the soft boundary reduces the density in the proximity of the obstacle and consequently lowers the local speed of sound. Then, from the local Landau criterion it is naturally suggested that the critical velocity of the hard cylinder defines an upper bound for that of the obstacle formed by the Gaussian potential. When the hole radius  $R$  becomes larger with higher  $V_0$  [Fig. 4.1(b)] and/or the beam width  $\sigma$  decreases for fixed  $R$  [Fig. 4.1(c)], the obstacle would converge to the hard cylinder with stiffening its boundary.

The main result of our measurements is that in the deep non-penetrable regime (i.e.,  $V_0 \gg \mu$ ), the critical velocity  $v_c$  increases with decreasing  $\sigma/\xi$  for fixed  $V_0/\mu$  and approaches about  $0.4c_s$ . This observation is consistent with the expectation from the aforementioned discussion based on the local Landau

criterion. Furthermore, the measured value of  $v_c/c_s$  with our stiffest obstacle is in good agreement with theoretical predictions for a 2D superfluid flow past a hard cylinder.

## 4.2 Experiment

Our experiment starts with a Bose-Einstein condensate of  $^{23}\text{Na}$  atoms in a harmonic trap formed by combining optical and magnetic potentials [15]. The condensate fraction of the sample is over 90%. In a typical sample condition, where the trapping frequencies are  $\omega_{r,z} = 2\pi \times (9.0, 400)$  Hz and the atom number of the condensate is  $N_0 = 3.2(2) \times 10^6$ , the condensate healing length is  $\xi = \hbar/\sqrt{2m\mu} \approx 0.46$   $\mu\text{m}$  and the speed of sound is  $c_s = \sqrt{\mu/m} \approx 4.3$  mm/s at the trap center, where  $\hbar$  is the Planck constant divided by  $2\pi$  and  $m$  is the atomic mass. By adjusting the trapping frequencies or the atom number of the condensate,  $\xi$  is varied up to 0.9  $\mu\text{m}$ . The Thomas-Fermi radius and thickness of the condensate are  $R_{\text{TF}}/\xi \geq 240$  and  $Z_{\text{TF}}/\xi \leq 6$ , respectively. In this highly oblate condensate, vortex line excitations are strongly suppressed [26, 27] and the vortex dynamics is expected to be 2D.

We adiabatically ramp up the power of a repulsive Gaussian laser beam in 1 s and hold it for 0.2 s to ensure that the condensate is stationary. Then, we translate the laser beam horizontally by 24  $\mu\text{m}$  by using a piezo-driven mirror<sup>23</sup>

---

<sup>2</sup>Now, we finally got piezo actuator and mirror mount (Newport) that can be combined nicely. Translating the obstacle rather than the trap would be better to clearly measure  $v_c$  without any subsidiary effect like sloshing mode of the condensate within the trap during the movement of the trap. It really comes out that when all the experimental conditions are same, moving the trap gives smaller  $v_c$ .

<sup>3</sup>To confirm immediate response of piezo to input analogue control voltage, we align the beam to photodiode and then check how much quickly the intensity changes due to the movement of the beam.

[Fig. 4.2(a)]. The beam power is kept constant during the translation with PID circuit which controls the AOM before the input of a fiber. A photodiode detects output beam power of the fiber, after filtering the beam polarization with wave plate and PBS.

The velocity  $v$  of the laser beam is kept constant during the translation and controlled by adjusting the traveling time. The sweeping region of the laser beam is centered in the condensate [Fig 4.2(b)]. The density variation over the region is less than 10% and the speed of sound can be well approximated to be spatially constant. After completing the sweeping, we slowly ramp down the laser beam power for 0.5 s and take an absorption image of the condensate after time-of-flight to detect vortices.

For our vortex generation and detection sequence, a vortex dipole is identified with two density-depleted holes that are symmetrically located in the condensate with respect to the sweeping line of the laser beam [Fig. 4.2(c) inset]. After generated in the center region of the condensate, the vortex dipole moves toward the edge of the condensate and split into two individual vortices that subsequently travel along the boundary of the condensate in opposite direction. This peculiar orbit motion of the vortices were studied in Ref. [13]. A single vortex was observed occasionally at low  $v$  with probability < 4%. Because the vortex lifetime is over 10 s [15], we attribute the single vortex to uncontrolled perturbations in sample preparation and we do not count it as a vortex dipole. (The probability for having a vortex in the condensate even without any beam translation varies day by day. We find that sample prepartion sequence is very important, especially for loading atoms from magnetic trap to the hybrid trap composed of magentic and attractive optical trap.)

The critical velocity  $v_c$  for vortex shedding is determined from the prob-

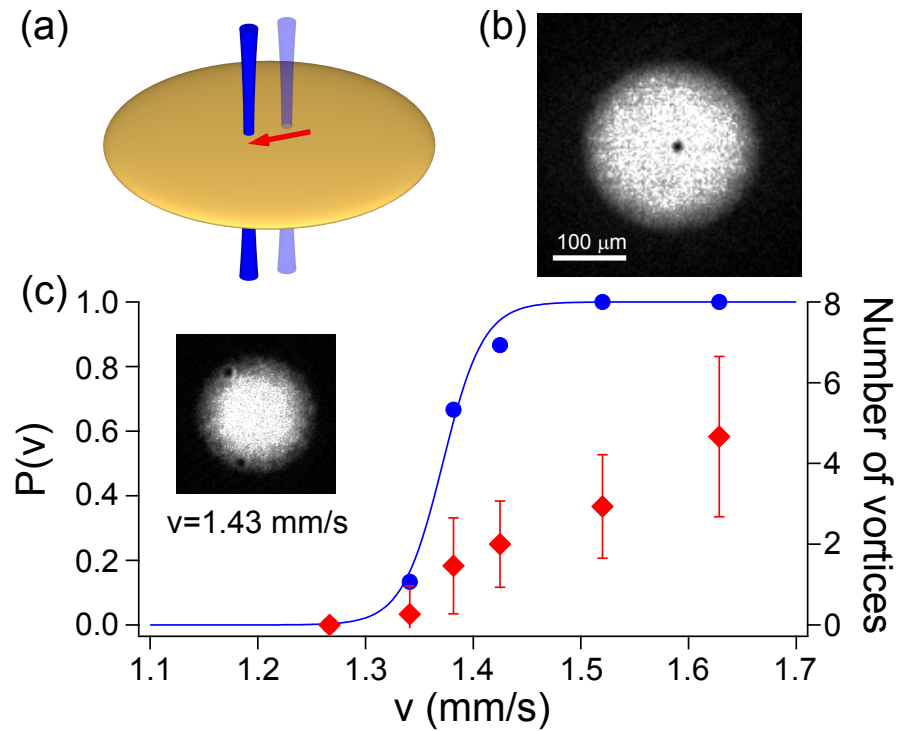


Figure 4.2: Vortex shedding in a highly oblate Bose-Einstein condensate. (a) Schematic of the experiment. An optical obstacle is formed by a repulsive Gaussian laser beam penetrating through the condensate and moves horizontally at a constant velocity in the center region. (b) in-situ image of the condensate with the optical obstacle at the initial position. (c) Probability  $P(v)$  of having vortex dipoles (blue circles) and the number of vortices (red diamonds) as a function of the velocity  $v$  of the optical obstacle. The barrier height  $V_0 \approx 2.1\mu$  and the Gaussian width  $\sigma \approx 20\xi$ . The solid line is a sigmoidal function fit to  $P(v)$ . The inset shows an image of a condensate containing a vortex dipole. Each data point was obtained from 15 realizations of the same experiment and the error bars indicate the standard deviations of the measurements.

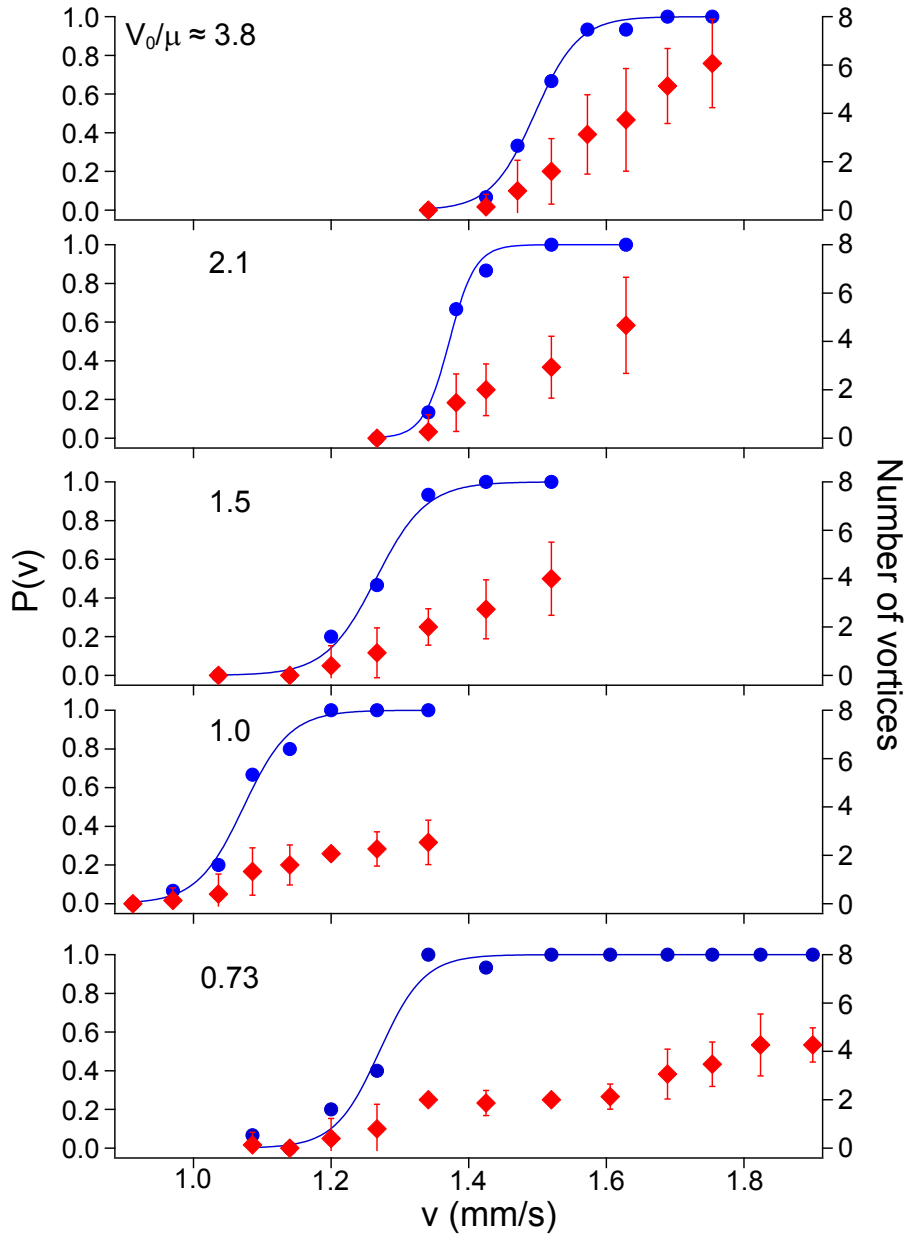


Figure 4.3: Five different example results for different  $V_0$ . Blue circles and red diamonds represent  $P(v)$  and number of vortices, respectively. Functional form of the number of vortices changes dramatically depending on  $V_0$ . Therefore, we use sigmoidal function fitting to  $P(v)$  to obtain  $v_c$ , which seems to be much better method.

ability distribution  $P(v)$  for having vortex dipoles after sweeping with the laser beam.  $P(v)$  is obtained from 15 realizations of the same experiment with a given sweeping velocity  $v$ , i.e.,  $P(v)$  is the ratio of the number of images showing vortex dipoles to the total number of measurements. The critical velocity  $v_c$  is determined by fitting a sigmoidal function to the probability distribution as  $P(v) = 1/(1 + e^{-(v-v_c)/\gamma})$  [Fig. 4.2(c)]. We use the value of  $1.5\gamma$  as the measurement uncertainty of  $v_c$ , corresponding to the range of  $0.2 \leq P \leq 0.8$ .

The reason why we use  $P(v)$  rather than the number of vortices to extract  $v_c$  is well represented in Fig. 4.3. One can find that the functional shape of the number of vortices depends strongly on  $V_0$ , in particular, near  $V_0 \approx \mu$ , whereas there is no ambiguity on  $P(v)$ . (Such shaporal differences were a bit strange and we did not concentrate on its origins at that time. We figure out the physical reason for stepwise shape of the number of vortices for  $V_0 < \mu$  cases is periodic shedding from penetrable beam. This will be discussed in the next chapter.)

#### 4.2.1 Calibration of Gaussian beam

A point is imaged as an Airy function when the imaging system has finite optical resolution. And the Airy pattern can be approximated to Gaussian shape (Here, I assume Gaussian function as  $V(r) = V_0 \exp(-2r^2/\sigma^2)$ ). The waist  $\sigma$  is slightly smaller than the radius of Airy disk (first zero) but nearly have same value. Taking into account this fact, it is natural to assume that finite imaging resolution just means Gaussian blur of the original object. Gaussian blur to a Gaussian object is nothing but a convolution of two Gaussian functions that have waists of  $\sigma_1$  and  $\sigma_2$ , which results in a new Gaussian function having waist  $\sqrt{\sigma_1^2 + \sigma_2^2}$ .

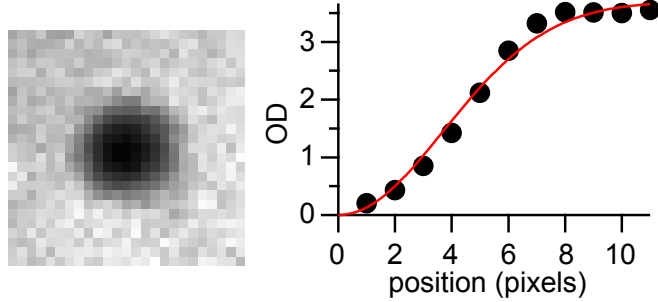


Figure 4.4: Gaussian beam calibration. The left image is averaged over 10 images taken with same beam conditions. The graph on the right shows radially averaged data of the left image.

The width  $\sigma$  of the laser beam is calibrated from the in-situ images of very dilute samples which are nearly penetrated through by the beam ( $V_0 \approx \mu$ ), where OD (optical density) at the center of the beam is approximately zero and no OD saturation effect occurs at the laser beam region. We take 10 images for the given beam conditions and obtain Gaussian waist after radially averaging the images Fig. 4.4. We estimate the actual beam waist by subtracting Gaussian blur due to finite imaging resolution ( $\approx 5 \mu\text{m}$ ) from measured beam waist, using the relation  $\sigma_{\text{meas}}^2 = \sigma_{\text{real}}^2 + \sigma_{\text{res}}^2$ , where  $\sigma_{\text{meas}}$ ,  $\sigma_{\text{real}}$  and  $\sigma_{\text{res}}$  indicate Gaussian waist of measured one, real one and imaging resolution, respectively. This simple in-situ method gives us reasonable value which is consistent with the value estimated from beam power and the condition  $V_0 \approx \mu$  which makes minimum OD nearly zero.

The beam waist of the laser beam is  $9.1(12) \mu\text{m}$  at the focal plane and the Gaussian width  $\sigma$  of the optical obstacle is controlled by defocusing the laser beam at the sample plane. The sample thickness ( $< 3 \mu\text{m}$ ) is much shorter than the Rayleigh length of the laser beam and we ignore the beam divergence. The beam width is much smaller than the condensate radius and the chemical

potential of the condensate is negligibly affected by the presence of the laser beam.

### 4.3 Results and Discussion

Figure 4.5(a) displays the results of the critical velocity as a function of the barrier height  $V_0$  for various beam widths. The critical velocity shows a dip structure having a minimum at  $V_0 \approx \mu$ , clearly distinguishing the two regimes: a penetrable regime with  $V_0 < \mu$  and a non-penetrable regime with  $V_0 > \mu$ . The dip structure of the critical velocity can be accounted for by a consideration based on the local Landau criterion. For  $V_0 < \mu$ , the density minimum is located at the top of the Gaussian potential and decreases for higher  $V_0$ , and thus, lowering the local speed of sound. On the other hand, when  $V_0 > \mu$ , as described before, the potential slope becomes steeper with higher  $V_0$  and the density in the proximity of the obstacle boundary is gradually restored back to the bulk density, leading to higher critical velocity. The dip structure around  $V_0 = \mu$  becomes more pronounced with larger  $\sigma/\xi$  by lowering the minimum value [Fig. 4.5(a) inset].

In terms of the vortex shedding mechanism, the penetrable regime is different because there is no density-depleted region in the fluid. It has been anticipated that vortex nucleation would be initiated by generation of rarefaction pulses [8,9,28,29]. Recently, the critical velocity of penetrable obstacles for dissipation has been investigated in effective one-dimensional (1D) systems [30–33]. In 1D, the critical velocity is predicted to vanish as  $V_0/\mu \rightarrow 1$  [31], which is not the case in our 2D situation. Moreover, the critical velocity shows a quite intriguing dependence on  $\sigma/\xi$  [Fig. 4.5(a) inset]. We find that the minimum

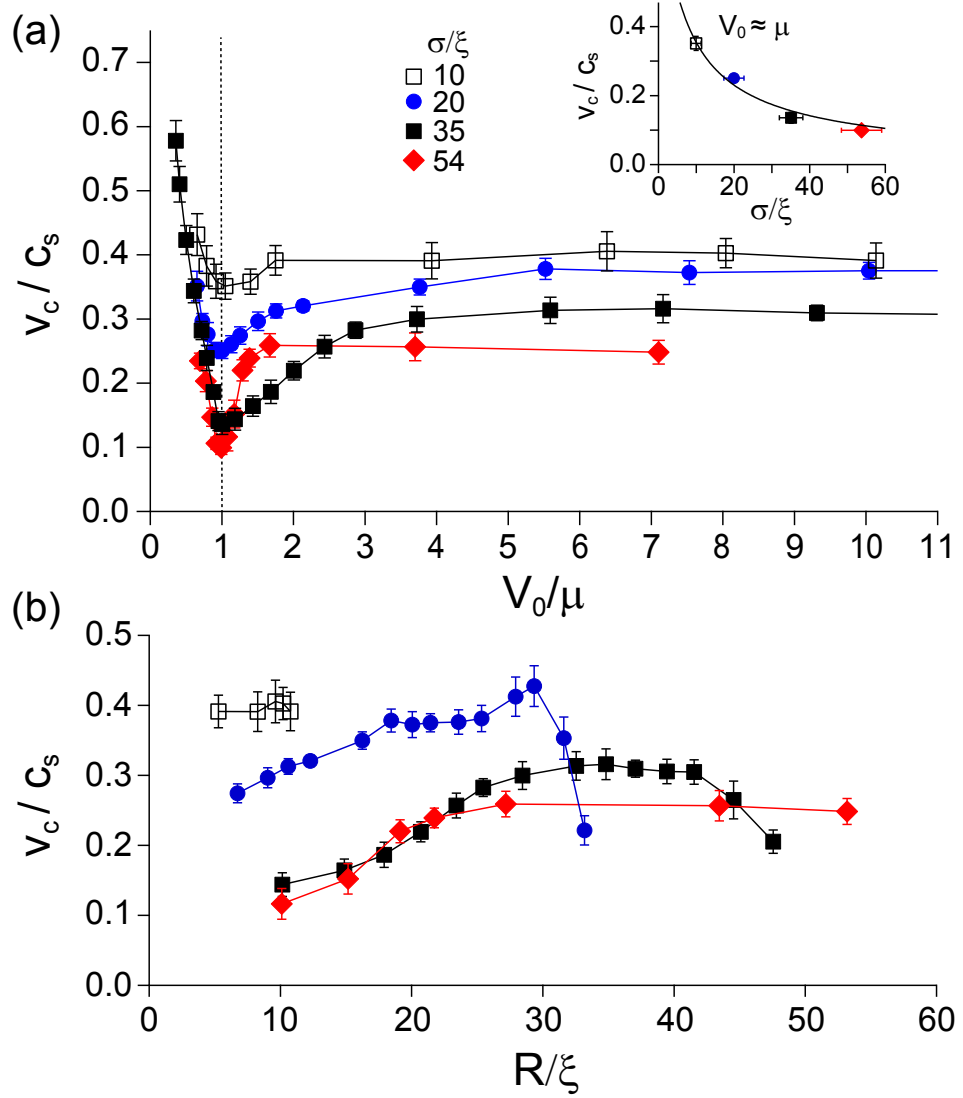


Figure 4.5: (a) Normalized critical velocity  $v_c/c_s$  versus the relative barrier height  $V_0/\mu$  for various beam widths  $\sigma/\xi$ .  $(\sigma, \xi) = (24.5(24), 0.46)$  (red diamonds),  $(16.0(14), 0.46)$  (black squares),  $(9.1(12), 0.46)$  (blue circles), and  $(9.1(12), 0.9) \mu\text{m}$  (open squares). The inset displays  $v_c/c_s$  at  $V_0 \approx \mu$  as a function of  $\sigma/\xi$  and the solid line is a guide line. (b) The same data in the non-penetrable regime ( $V_0 > \mu$ ) as a function of the hole radius  $R/\xi$ , together with additional data points for  $V_0/\mu > 10$ .

values of  $v_c/c_s$  for each  $\sigma/\xi$  is well followed by the guide line of the inset in fig. 4.5(a), which has a functional form of  $1/\sigma \ln(\sigma/\xi)$ , i.e., Feynman's critical velocity. But yet, it is difficult to understand the reason why it has similar form of Feynman's critical velocity. Further investigation on the functional form of  $v_c(V_0/\mu; \sigma/\xi)$  in the penetrable regime is warranted. However, in this work, we focus on the non-penetrable regime to address the 2D hard cylinder situation.

In Fig. 4.5(b), we recast the data for the non-penetrable regime ( $V_0 > \mu$ ) as a function of the hole radius  $R$ , together with additional data obtained for  $V_0 > 10\mu$  with  $\sigma = 20\xi$  and  $35\xi$ . Note that the hole radius is weakly dependent on the barrier height as  $R \propto \sqrt{\ln(V_0/\mu)}$ . From the previous discussion on the boundary stiffness effect and  $S \propto R/\sigma^2$  [Fig. 4.1(b)], one may expect that  $v_c/c_s$  would be saturated to a certain value with increasing hole radius and also that the saturation behavior would be faster with smaller beam width. We see that the experiment data roughly follows the expectation in a small  $R$  region. However, when  $R$  increases further, the growth rate of the critical velocity becomes negative. At  $R/\xi \sim 35$ , the critical velocity with small  $\sigma/\xi = 20$  is even lower than that with large  $\sigma/\xi = 54$ .

One possible explanation for such climbing-over behavior of the critical velocity is the imperfection of the laser beam profile. If the beam profile is not perfectly Gaussian, for example, the intensity profile in the outer part of the laser beam decays slower than exponential, then the potential slope  $S$  at the obstacle boundary would decrease with increasing  $R$ . We see that the climbing-over of  $v_c$  occurs at  $R \sim \sigma$  in both of the data sets with  $\sigma/\xi = 20$  and  $35$ . This seems to support the beam profile effect because in our experiment  $\sigma$  is varied by defocusing the same laser beam. The  $M^2$  factor of the laser beam is measured to be 1.2.

To further investigate the soft boundary effect on the critical velocity, we take a different scanning trajectory in the parameter space of the Gaussian obstacle: decreasing  $\sigma/\xi$  for fixed  $V_0/\mu$ . In this setting, the hole radius  $R$  is also varied proportionally with  $\sigma$  [Eq. (1)] and the trajectory corresponds to a diagonal line in Fig. 1(a). A scanning with fixed  $R/\xi$ , as depicted in Fig. 1(c), might be more ideal in terms of isolating the finite- $R/\xi$  effect [5, 8, 9], but this would require exponentially high  $V_0/\mu$  for small  $\sigma/\xi$  as  $V_0/\mu = e^{2(R/\sigma)^2}$ , necessarily recalling the outer part of the laser beam. We set  $V_0/\mu \approx 7$ , around which  $v_c(V_0/\mu)$  shows a maximum in the previous measurements.  $R \approx \sigma$  and the normalized boundary slope  $\tilde{S} = (\xi/\mu)S \approx 4(\sigma/\xi)^{-1}$ .

In Fig. 4, we see that the critical velocity monotonically increases as  $\sigma/\xi$  decreases, which is consistent with our expectation from the boundary stiffness. It is worth noting that although the data are obtained from various samples with different healing lengths, they agree with each other in the plane of the dimensionless parameters  $\sigma/\xi$  and  $v_c/c_s$ . This demonstrates the 2D character of our system because the healing length is the only relevant length scale in 2D superfluid hydrodynamics.

For our stiffest obstacle,  $v_c/c_s$  is measured to be about 0.40, which is slightly higher than the predicted value of 0.37 for a 2D hard cylinder in the large  $R/\xi$  limit. In our measurement,  $R \geq 10\xi$  marginally satisfies the large obstacle condition, and we attribute the deviation of the measured value to the finite- $R/\xi$  effect. The dependence of the critical velocity on  $R/\xi$  was theoretically investigated [5, 8, 9] and it was shown that  $v_c/c_s$  gradually increases from the value of 0.37 as  $R/\xi \rightarrow 0$ . For comparison, in Fig. 4.6 we display the theoretical results for a 2D hard cylinder of radius  $R = \sigma\sqrt{\ln(V_0/\mu)/2}$  from Ref. [8] (blue open circles). It is clearly observed that our measurement results

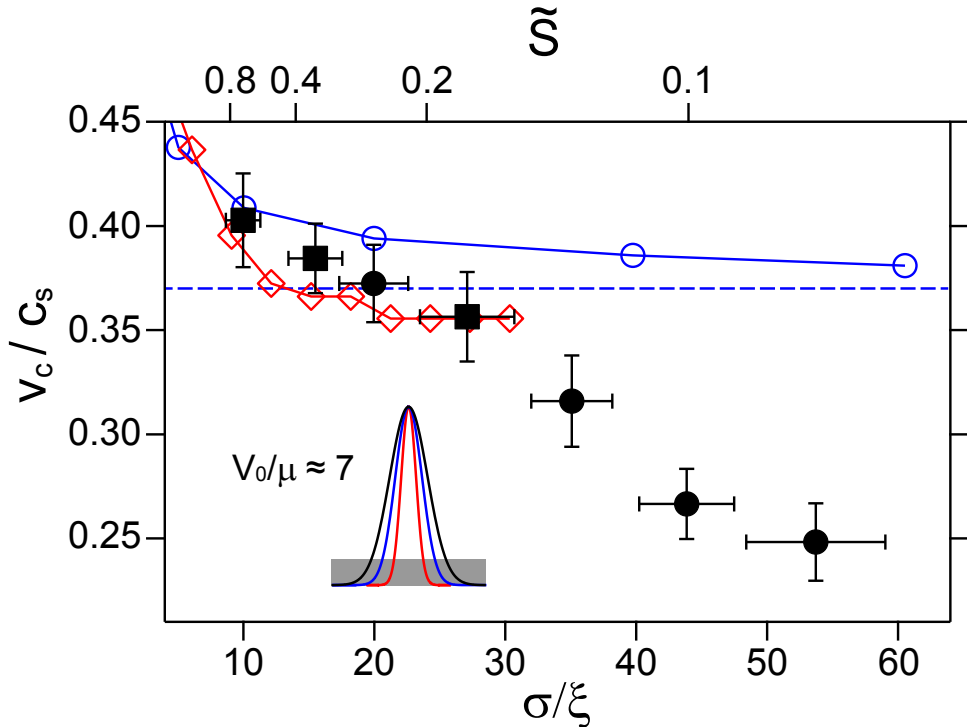


Figure 4.6:  $v_c/c_s$  versus  $\sigma/\xi$  for fixed  $V_0/\mu \approx 7$ .  $\sigma = 9.1(12) \mu\text{m}$  is for black solid squares and  $\xi = 0.46 \mu\text{m}$  is for black solid circles. The blue open circles show the theoretical calculation results for a 2D hard cylinder of radius  $R = \sigma\sqrt{\ln(V_0/\mu)/2}$  from Ref. [8]. The red open diamonds indicate the numerical results for a Gaussian potential with  $V_0/\mu = 100$  from Ref. [35], where the potential slope  $\tilde{S}$  would be about two times higher than ours. The dashed line denotes the theoretically predicted value,  $v_c/c_s = 0.37$  for a 2D homogeneous case with a hard cylinder in the large obstacle limit [7–9].

converges to the theoretical predictions when  $\sigma/\xi$  decreases, i.e., the obstacle boundary becomes stiffer. We also display in Fig. 4.6 the result of numerical simulations performed with a Gaussian potential with  $V_0/\mu = 100$  in Ref. [35] (red open diamonds). The experimental results converge to the theoretical predictions when  $\sigma/\xi$  decreases, i.e., the optical obstacle becomes similar to a hard cylinder by stiffening its boundary.

Our results are inconsistent with the  $1/R$  dependence of  $v_c$  that was predicted from analytic analyses on the stability of a superfluid flow [18, 34]. It is clearly seen in Fig. 4 that when  $\sigma/\xi$  ( $\approx R/\xi$ ) increases by a factor of 5, the  $v_c/c_s$  decreases less than a factor of 2. Even without including the additional reduction effect due to the soft boundary of the obstacle, the critical velocity decreases much smaller than what is expected from the  $1/R$  dependence.

Finally, we want to recall a few aspects of the experimental conditions that should be considered for the quantitative comparison of the measurement results to theoretical predictions for a 2D homogeneous case. First one is that, the critical velocity was not measured for a steady flow condition but by sweeping a finite section of a trapped condensate. The measurement can be affected by the sweeping manner. For example, if vortex nucleation requires a finite time, which might be longer than the sweeping time near the critical velocity [6, 22], it would result in a systematic upward shift of the measured value of  $v_c$  (further studies on this subject is handled in next chapter and indeed we find the importance of vortex nucleation time which affects the measurements on  $v_c$ .). Second, although we expect suppression of 3D vortex dynamics in a highly oblate condensate, it is an inevitable fact that the condensate has an inhomogeneous density distribution along the axial direction. Thus, one cannot completely ignore 3D responses of the condensate, in particular, at the moment of vortex

nucleation. It might be necessary or sufficient to introduce an effective speed of sound that would be lower than the peak value  $c_s$  of the condensate [36].

## 4.4 Summary

In summary, we have presented the measurements of the critical velocity for vortex shedding in highly oblate Bose-Einstein condensates and investigated the soft boundary effect of the moving obstacle formed by a Gaussian potential. Our results are consistent with a picture based on the local Landau criterion and the measured value of  $v_c/c_s$  with the stiffest obstacle is in good agreement with the theoretical predictions for a homogeneous 2D superflow past a cylindrical object.

This work has established a reliable experimental method to measure the critical velocity of a trapped condensate and its intriguing extension is to investigate the temperature dependence of the critical velocity, which might provide a new setting to study the role of thermal atoms in vortex nucleation [37–39]. In particular, for 2D geometry where the superfluidity originates from BKT physics, thermal gas could change the situation a little different from simple vortex shedding in a superfluid since thermal vortices and antivortices inherently exist in 2D geometry. In 3D finite temperature BECs, however, a recent numerical study [40] shows that critical velocity is simply given by some fixed fraction of sound velocity (based on BEC density for given temperature) of the system for a given obstacle.

# Bibliography

- [1] L. D. Landau, J. Phys. USSR **5**, 71 (1941).
- [2] L. D. Landau and E. M. Lifshitz, *Fluid Mechanics* (Pergamon Press, Oxford, 1987).
- [3] T. Frisch, Y. Pomeau, and S. Rica, Phys. Rev. Lett. **69**, 1644 (1992).
- [4] B. Jackson, J. F. McCann, and C. S. Adams, Phys. Rev. Lett. **80**, 3903 (1998).
- [5] C. Huepe and M. E. Brachet, Physica D **140** 126 (2000).
- [6] N. G. Berloff and P. H. Roberts, J. Phys. A: Math. Gen. **33**, 4025 (2000).
- [7] S. Rica, Physica D **148** 221 (2001).
- [8] C.-T. Pham, C. Nore, and M. E. Brachet, Physica D **210**, 203 (2005).
- [9] F. Pinsker and N. G. Berloff, Phys. Rev. A **89**, 053605 (2014).
- [10] C. Raman, M. Köhl, R. Onofrio, D. S Durfee, C. E. Kuklewicz, Z. Hadzibabic, and W. Ketterle, Phys. Rev. Lett. **83**, 2502 (1999).
- [11] R. Onofrio, C. Raman, J. M. Vogels, J. R. Abo-Shaeer, A. P. Chikkatur, and W. Ketterle, Phys. Rev. Lett. **85**, 2228 (2000).

- [12] S. Inouye, S. Gupta, T. Rosenband, A. P. Chikkatur, A. Görlitz, T. L. Gustavson, A. E Leanhardt, D. E. Pritchard, and W. Ketterle, Phys. Rev. Lett. **87**, 080402 (2001).
- [13] T. W. Neely, E. C. Samson, A. S. Bradley, M. J. Davis, and B. P. Anderson, Phys. Rev. Lett. **104**, 160401 (2010).
- [14] R. Desbuquois, L. Chomaz, T. Yefsah, J. Léonard, J. Beugnon, C. Weitenberg, and J. Dalibard, Nat. Phys. **8**, 645 (2012).
- [15] W. J. Kwon, M. Geol, J. Choi, S. W. Seo, and Y. Shin, Phys. Rev. A **90**, 063627 (2014).
- [16] T. Winiecki, B. Jackson, J. F. McCann, and C. S. Adams, J. Phys. B: At. Mol. Opt. Phys. **33**, 4069 (2000).
- [17] P. O. Fedichev and G. V. Shlyapnikov, Phys. Rev. A **63**, 045601 (2001).
- [18] M. Crescimanno, C. G. Koay, R. Peterson, and R. Walsworth, Phys. Rev. A **62**, 063612 (2000).
- [19] C. Nore, C. Huepe, and M. E. Brachet, Phys. Rev. Lett. **84**, 2191 (2000).
- [20] B. Jackson, J. F. McCann, and C. S. Adams, Phys. Rev. A **61**, 051603(R) (2000).
- [21] A. Aftalion, Q. Du, and Y. Pomeau, Phys. Rev. Lett. **91**, 090407 (2003).
- [22] K. Fujimoto and M. Tsubota, Phys. Rev. A **83**, 053609 (2011).
- [23] G. W. Stagg, A. J. Allen, N. G. Parker, and C. F. Barenghi, Phys. Rev. A **91**, 013612 (2015).

- [24] G. Nardin, G. Grosso, Y. Léger, B. Pietka, F. Morier-Genoud, and B. Deveaud-Plédran, Nat. Phys. **7**, 635 (2011).
- [25] A. Amo, S. Pegeon, D. Sanvitto, V. G. Sala, R. Hivet, I. Carusotto, F. Pisanello, G. Leménager, R. Houdré, E. Giacobino, C. Ciuti, and A. Bramati, Science **332**, 1167 (2011).
- [26] B. Jackson, N. P. Proukakis, C. F. Barenghi, and E. Zaremba, Phys. Rev. A **79**, 053615 (2009).
- [27] S. J. Rooney, P. B. Blakie, B. P. Anderson, and A. S. Bradley, Phys. Rev. A **84**, 023637 (2011).
- [28] T. Aioi, T. Kadokura, T. Kishimoto, and H. Saito, Phys. Rev X **1**, 021003 (2011).
- [29] B. Jackson, Ph.D. thesis, Durham University, 2000.
- [30] P. Engels and C. Atherton, Phys. Rev. Lett. **99**, 160405 (2007).
- [31] M. Albert, T. Paul, N. Pavloff, and P. Leboeuf, Phys. Rev. Lett. **100**, 250405 (2008).
- [32] D. Dries, S. E. Pollack, J. M. Hitchcock, and R. G. Hulet, Phys. Rev. A **82**, 033603 (2010).
- [33] K. C. Wright, R. B Blakestad, C. J. Lobb, W. D. Phillips, and G. K. Campbell, Phys. Rev. A **88**, 063633 (2013).
- [34] J. S. Stießberger and W. Zwerger, Phys. Rev. A **62**, 061601(R) (2000).

- [35] G. W. Stagg, N. G. Parker, and C. F. Barenghi, J. Phys. B: At. Mol. Opt. Phys. **47**, 095304 (2014).
- [36] G. Huang, V. A. Makarov, and M. G. Velarde, Phys. Rev. A **67**, 023604 (2003).
- [37] J. E. Williams, E. Zaremba, B. Jackson, T. Nikuni, and A. Griffin, Phys. Rev. Lett. **88**, 070401 (2002).
- [38] A. A. Penckwitt, R. J. Ballagh, and C. W. Gardiner, Phys. Rev. Lett. **89**, 260402 (2002).
- [39] K. Kasamatsu, M. Tsubota, and M. Ueda, Phys. Rev. A **67**, 033610 (2003).
- [40] G. W. Stagg, R. W. Pattinson, C. F. Barenghi, and N. G. Parker, arxiv:1510.01895 (2015).

# Chapter 5

## Periodic vortex shedding from a moving Gaussian obstacle

In the previous chapter, the moment of generation of a vortex dipole, i.e., critical velocity  $v_c$  is explored. In this chapter, I will introduce our experiments on characteristics of vortex shedding dynamics in a BEC, including periodic vortex dipole shedding from penetrable beam and observed interesting shedding patterns. Due to periodic shedding of vortex dipoles from penetrable beam ( $V_0 < \mu$ ), we are able to achieve deterministic generation of a single votex dipole which can be practically applied to demonstrate a vortex dipole-dipole collision experiment. In addition, preliminary results on distinct feature of vortex shedding from impenetrable beam ( $V_0 > \mu$ ) will be presented.

The most contents of this chapter can be found on the following paper.

- W. J. Kwon, S. W. Seo, and Y. Shin, “*Periodic shedding of vortex dipoles from a moving penetrable obstacle in a Bose-Einstein condensate*”, Physical Review A **92**, 033613 (2015).

## 5.1 Introduction

Since the first realization of atomic Bose-Einstein condensates (BECs), vortex dynamics has been one of the major focuses of BEC research [1]. In recent experiments, many efforts were made to study the dynamics of vortex dipoles. A vortex dipole is a pair of vortices of opposite circulations and its creation and annihilation are at the heart of many two-dimensional (2D) superfluid phenomena such as Berezinskii-Kosterlitz-Thouless superfluids [2, 3], phase transition dynamics [4, 5], and superfluid turbulence [6, 7]. Quantized vortex dipoles were created in BECs by moving optical obstacles [8–10] and via quenching dynamics [11, 12], and also observed in quasi-2D degenerate Bose gases [13]. Orbital motions of a single vortex dipole in a trapped BEC were investigated [9, 12, 14] and annihilation of vortex dipoles was indirectly probed in relaxation of superfluid turbulence in highly oblate BECs [15].

Here, we present an experimental study of vortex shedding from a moving repulsive Gaussian laser beam in a highly oblate BEC. The primary result of this work is that when the optical obstacle is penetrable (i.e., the potential barrier height  $V_0$  of the laser beam is smaller than the chemical potential  $\mu$  of the condensate), vortex dipoles are periodically shed from the moving obstacle. Furthermore, we find that the vortex shedding frequency linearly increases with the obstacle velocity as it exceeds a critical velocity. The periodic vortex shedding behavior is so pronounced that we demonstrate that a single vortex dipole can be deterministically generated by applying a short linear sweep of a penetrable laser beam.

A fluid flowing past an obstacle is a textbook situation in fluid dynamics. In the case of a superfluid, it is well known that when the flow velocity exceeds a

critical velocity, the superfluid becomes dissipative via vortex generation [16,17]. Early theoretical works for 2D geometry anticipated periodic shedding of vortex dipoles from a moving circular obstacle [16–20], where the periodic shedding was depicted as a cycling process where the work done by a drag force from the moving obstacle accumulates to generate a quantized vortex dipole of a finite energy. However, in previous BEC experiments [8–10], periodic vortex shedding has never been observed, although the existence of a critical velocity was clearly demonstrated.

In generating a vortex dipole, a penetrable obstacle with  $V_0/\mu < 1$  has a clear advantage over an impenetrable obstacle. Because there is no zero-density region in the condensate, it is ensured that a vortex and an antivortex would be created at the same time into the condensate. On the other hand, in the impenetrable case, there is a zero-density region occupied by the obstacle such that a vortex can be individually emitted into the condensate, while the other vortex that is created as a partner of the emitted vortex still remains in the zero-density region [21, 22]. The individual vortex emission might be induced by small fluctuations in superfluid flow, breaking the mirror symmetry of the system with respect to the obstacle moving direction. Recent numerical studies on vortex shedding from an impenetrable obstacle showed that vortex shedding is mostly irregular and regular shedding of vortex dipoles occurs only in a stringent condition of the obstacle [21, 23, 24], which is practically difficult to satisfy in current experiments. Indeed, we find that dipole shedding from impenetrable obstacle is prone to irregular shedding. In this work, we observe that a moving *penetrable* obstacle sheds vortex dipoles in a periodic and stable manner.

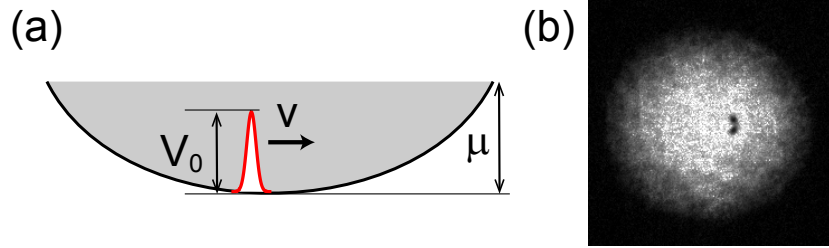


Figure 5.1: (a) Schematic of the experiment. A penetrable obstacle is formed by a repulsive Gaussian laser beam and it moves with velocity  $v$  in the center region of a highly oblate Bose-Einstein condensate (BEC). The barrier height  $V_0$  of the optical potential is lower than the chemical potential  $\mu$  of the BEC. (b) Time-of-flight absorption image of a BEC. A vortex dipole is generated by the moving obstacle and it is identified with its pair of density-depleted cores.

## 5.2 Experiment

The experimental setup is similar to that in our previous work [10]. A highly oblate BEC of  $^{23}\text{Na}$  atoms is prepared in a hybrid trap composed of a pancake-shaped optical trap and a magnetic quadrupole trap. The trapping frequencies are  $\omega_{r,z} = 2\pi \times (9.0, 400)$  Hz and the atom number in the condensate is  $N_0 = 3.3(2) \times 10^6$ , giving the chemical potential  $\mu \approx h \times 1.0$  kHz, where  $h$  is the Planck constant. The condensate fraction of the sample is over 80%. At the trap center, the healing length is  $\xi = \hbar/\sqrt{2m\mu} \approx 0.45$   $\mu\text{m}$  and the speed of sound is  $c_s = \sqrt{\mu/m} \approx 4.3$  mm/s, where  $\hbar = h/2\pi$  and  $m$  is the atomic mass. The Thomas-Fermi radius of the trapped condensate is  $R = \sqrt{2\mu/m\omega_r^2} \approx 110$   $\mu\text{m}$ .

An optical obstacle is formed by a repulsive Gaussian laser beam whose  $1/e^2$  width is  $\sigma = 9.1(12)$   $\mu\text{m} \approx 20\xi$ . We initially locate the laser beam 11.5  $\mu\text{m}$  away from the condensate center and horizontally translate it through the center region of the condensate using a piezo-driven mirror [Fig. 5.1(a)]. The moving velocity  $v$  of the laser beam is kept constant during the translation. After the

laser beam sweep, we linearly ramp down the beam power within 20 ms and then take an absorption image of the condensate to detect vortices [Fig. 5.1(b)]. When we release the trapping potential, we turn off the magnetic trap 13 ms earlier than the optical trap and place 24 ms free expansion before taking the image.

## 5.3 Periodic vortex shedding

### 5.3.1 Penetrable obstacle

We first investigate the case of a penetrable obstacle with  $V_0/\mu \approx 0.74$  by measuring the number of vortex dipoles generated from the obstacle as a function of the sweeping time  $t$  for various moving velocities  $v$ . The measurements results are displayed in Fig. 5.2(a). We see that the vortex dipole number  $N_d$  shows stepwise increasing behavior as a function of  $t$ . There is a certain amount of an inert time  $\tau_v$  before generating the first vortex dipole and another sweeping time almost equal to  $\tau_v$  is required to generate the second vortex dipole. This regular stepping-up feature clearly indicates that the inert time is not due to the transient response of the condensate to the perturbations of the laser beam but an intrinsic activation time for generating a vortex dipole from the moving obstacle. The periodic vortex generation might be understood as a cycling process where the moving obstacle exerts a drag force during the activation time and the accumulated energy is released as a vortex dipole at a certain threshold condition [19].

It was theoretically anticipated that the vortex shedding frequency  $f_v$  linearly increases with the moving velocity  $v$  of the obstacle as  $f_v = a(v - v_c)$ ,

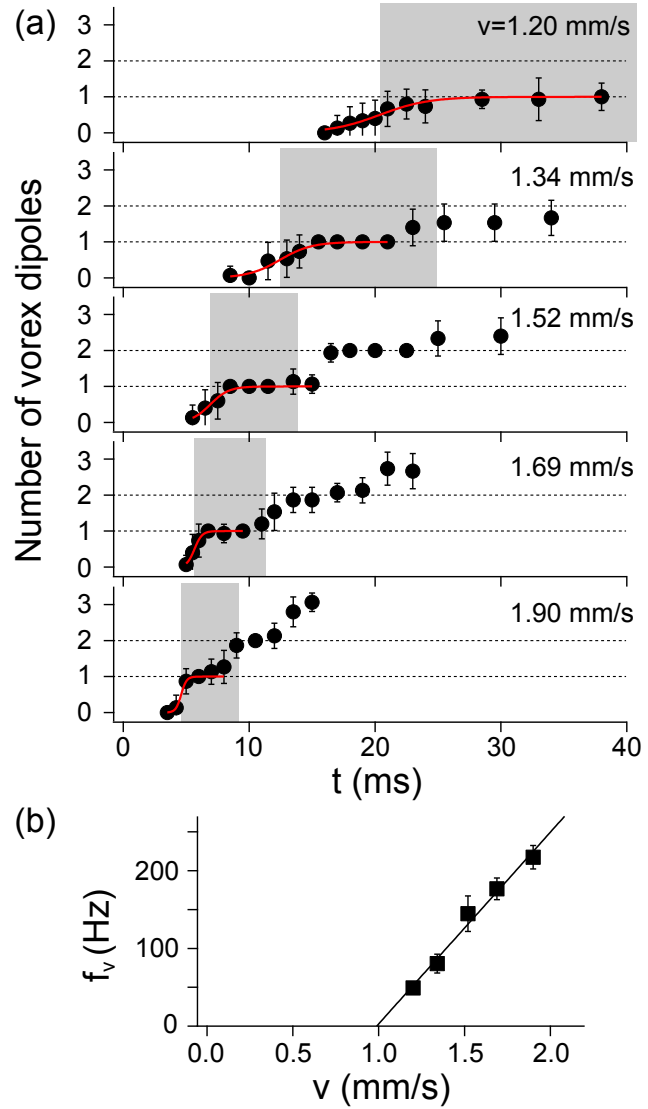


Figure 5.2: Periodic shedding of vortex dipoles from a moving penetrable obstacle of  $V_0/\mu \approx 0.74$ . (a) Number of generated vortex dipoles,  $N_d$  as a function of the sweeping time  $t$  for various moving velocities  $v$  of the obstacle. Each data point consists of 15 realizations of the same experiment and the error bar indicates the standard deviation of the measurements. The activation time  $\tau_v$  for generating the first vortex dipole was determined from a sigmoidal function fit (red solid lines, see the text for detail) to the data up to the  $N_d=1$  plateau region. The shaded area indicates the region of  $\tau_v < t < 2\tau_v$ . (b) Vortex shedding frequency  $f_v = 1/\tau_v$  as a function of  $v$ . The solid line is a linear fit to the data.

where  $v_c$  is a critical velocity [16, 18–20, 25, 26]. Interpreting the activation time  $\tau_v$  as the inverse of  $f_v$ , we find that our experimental data support the theoretical prediction [Fig. 5.2(b)].  $\tau_v$  was determined by fitting a sigmoidal function  $N_d = [1 + e^{-(t-\tau_v)/\gamma}]^{-1}$  to the data up to the  $N_d=1$  plateau region. Here  $\gamma$  represents the jittering of the vortex emission event and we used the value of  $1.5\gamma$  as the measurement uncertainty of  $\tau_v$ . Fig. 5.2(b) shows  $f_v = 1/\tau_v$  as a function of  $v$  and the result is well described with the functional form of  $f_v = a(v - v_c)$ , giving  $v_c = 0.99(4)$  mm/s and  $a = 0.25(2)$   $\mu\text{m}^{-1}$ .

We present another set of measurements in Fig. 5.3(a), where  $N_d$  is measured as a function of  $v$  for fixed sweep lengths  $L = vt$  of the laser beam. This is a typical situation addressed in previous experiments to measure the critical velocity  $v_c$  for vortex shedding [9, 10, 15]. Our motivation is to examine the effect of the finite activation time  $\tau_v$  on the determination of  $v_c$ . In order to generate vortices, the sweeping time  $t = L/v$  should be longer than  $\tau_v$ , which requires  $v < aL(v - v_c)$  from the relation  $f_v = a(v - v_c) = 1/\tau_v$ . Therefore, in the fixed  $L$  setting, the critical velocity would be measured with a systematic error of  $\delta v_c = v_c/(aL - 1)$ . Indeed, we observe that the measured critical velocity  $\tilde{v}_c$  increases with decreasing  $L$  [Fig. 5.3(b)] (similar result is obtained with impenetrable beam too).  $\tilde{v}_c$  was determined using the data analysis method described in our previous work [10]. The inhomogeneous density effect is negligible because the variation of the local speed of sound  $c_s$  is less than 5% even for the longest  $L = 46$   $\mu\text{m}$ . The linear extrapolation of the experiment data to  $1/L = 0$  gives a velocity of  $0.97(3)$  mm/s [Fig. 5.3(b)], which is remarkable in that this value is consistent with the critical velocity  $v_c$  obtained from the vortex shedding frequency data in Fig. 5.2(b).

The blue solid lines in Fig. 5.3(a) indicate the model predictions assuming

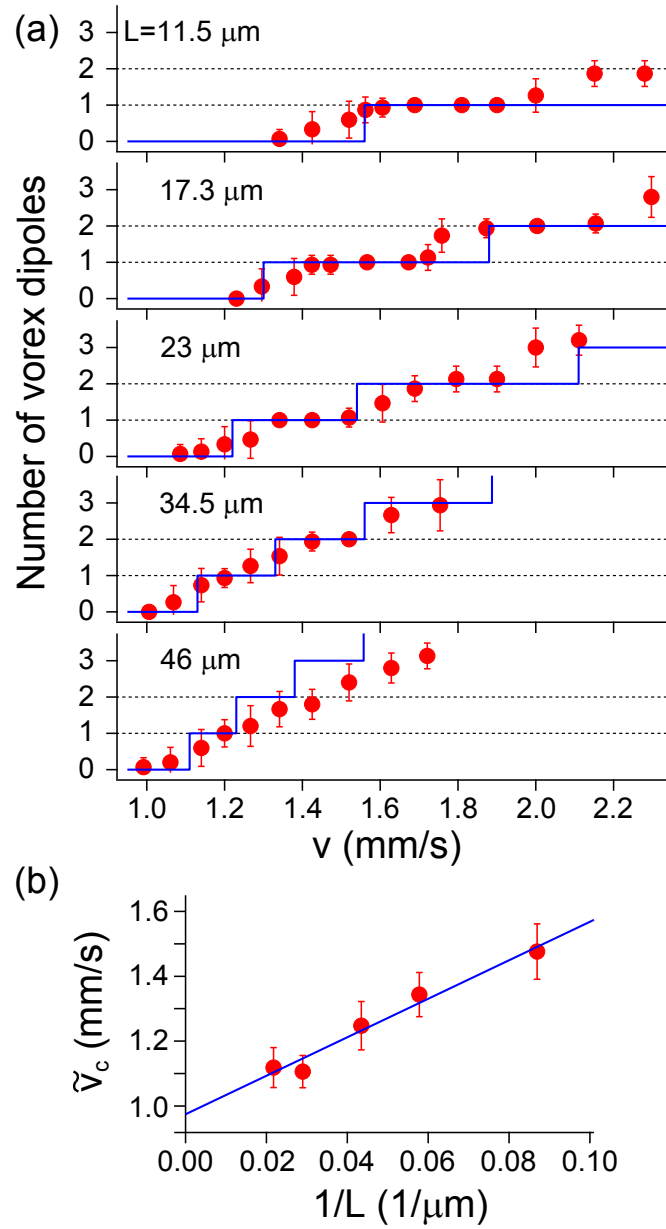


Figure 5.3: (a) Vortex dipole number  $N_d$  as a function of  $v$  for fixed sweep length  $L = vt$ .  $V_0/\mu \approx 0.74$ . The blue solid lines are the theoretical predictions obtained from a model assuming perfect periodic vortex shedding with  $f_v = a(v - v_c)$ ,  $a = 0.25 \mu\text{m}^{-1}$ , and  $v_c = 1.0 \text{ mm/s}$  [Fig. 5.2(b)]. (b) Critical velocity  $\tilde{v}_c$  measured for fixed  $L$ .  $\tilde{v}_c$  was determined from the data in (a), using the data analysis method described in Ref. [10]. The solid line is a linear fit to the data.

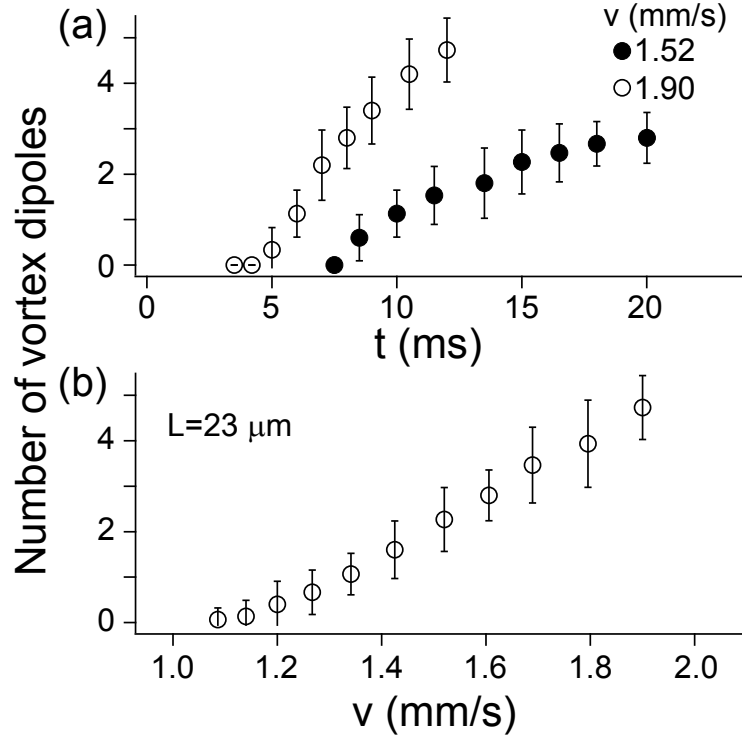


Figure 5.4: Vortex shedding from a moving impenetrable obstacle of  $V_0/\mu \approx 1.5$ . (a) Vortex dipole number  $N_d$  versus sweeping time  $t$ . (b)  $N_d$  as a function of the moving velocity  $v$  for sweep length  $L = 23 \mu\text{m}$ .

perfect periodic generation with  $f_v = a(v - v_c)$ ,  $a = 0.25 \mu\text{m}^{-1}$  and  $v_c = 1 \text{ mm/s}$ . Most of the qualitative features of the experimental data are explained with the model, including the reduction of the  $N_d=1$  plateau region with increasing  $L$ . This observation corroborates the periodic shedding of vortex dipoles from the moving penetrable obstacle.

### 5.3.2 Impenetrable obstacle

We perform the same measurements with an impenetrable laser beam of  $V_0/\mu \approx 1.5$  (Fig. 5.4). Interestingly, the activation time is still necessary for generating

the first vortex dipole and reduces with higher moving velocity as observed with the penetrable obstacle. This seems to be consistent with our description that the activation time is required to accumulate a certain amount of energy with the drag force to form a vortex dipole. However, no periodic vortex shedding is observed within the given conditions, which supports the fact that periodic shedding of vortex dipoles is only allowed for specific obstacle conditions [21, 23, 24]. And the number of vortex dipoles grows monotonically once the first vortex dipole is emitted. This means that the subsequent vortex generations are significantly affected by the presence of the first vortex dipole [22, 27]. It is noted that for  $v = 1.90$  mm/s in Fig. 5.4(a), the increasing rate of  $N_d$  is almost four times higher than the inverse of the activation time, which implies that vortex shedding can be accelerated in the presence of other vortices near the obstacle.

The distinctive difference of the impenetrable case from the penetrable case is that there is a zero-density region occupied by the obstacle. Hence, it is possible for vortices to be emitted individually into the condensate. The individually emitted vortices would disturb the superfluid velocity field around the obstacle more strongly than a vortex dipole, leading to irregular vortex shedding or possibly more intriguing shedding patterns such as the Bénard-von Kármán vortex street [21, 24].

In Fig. 5.5, we present several vortex images containing a few vortex dipoles. It is clearly seen that the vortex shedding pattern is irregular in the impenetrable case and was often observed that the propagation direction of the first vortex dipole largely deviated from the moving direction of the obstacle [Fig. 5.5(a)], implying that the two vortices were emitted at different times from the obstacle. Furthermore, vortex clusters having larger density-depleted

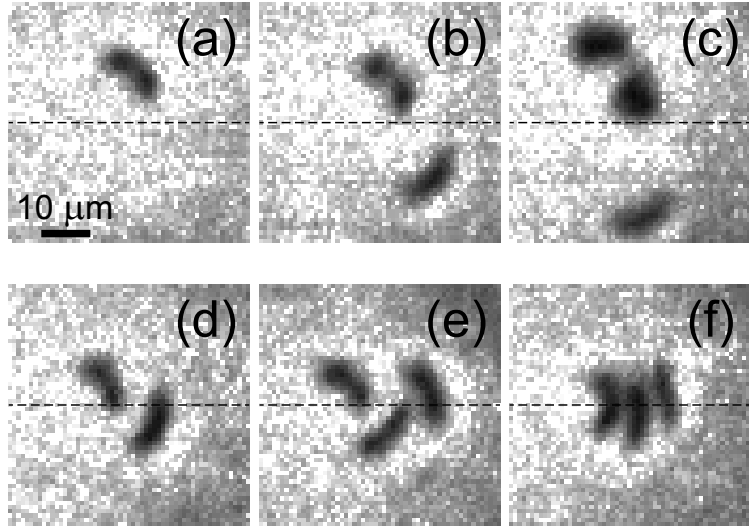


Figure 5.5: Various patterns of vortex shedding from (a)-(c) impenetrable and (d)-(f) penetrable obstacles. In the impenetrable case, the first vortex dipole was often observed to propagate in a direction largely deviated from the  $+x$  moving direction of the obstacle. The dashed lines indicate the moving line of the obstacle. (c) Vortex clusters having larger density-depleted regions were also observed. In the penetrable case, staggered configurations of multiple vortex dipoles were typically observed. (f) Occasionally, symmetric trains of vortex dipoles also appeared.

cores were sometimes observed [Fig. 5.5(c)] [9, 23]. On the other hand, the first vortex dipole from a penetrable obstacle usually propagates along the moving direction of the obstacle. Symmetric periodic array of vortex dipoles are known to be unstable towards staggered configurations of vortex dipoles [21, 22, 28], which were typically observed in the experiment when multiple vortex dipoles were generated [Figs. 5.5(d) and (e)]. Occasionally, symmetric trains of vortex dipoles were observed [Fig. 5.5(f)].

## 5.4 Deterministic generation of a single vortex dipole

In the experiment data for the penetrable obstacle in Fig. 5.2(a), it is evident that fluctuations of the vortex dipole number  $N_d$  are strongly suppressed for  $\tau_v < t < 2\tau_v$  and even vanish for some conditions. This is an outstanding feature of the periodic vortex shedding, suggesting that deterministic generation of a single vortex dipole is possible when applying a short sweep of the penetrable laser beam. In this section, we characterize this short sweep method by examining the stability of the propagation velocity of the generated vortex dipole.

In Figs. 5.6(a) and (b), we show two exemplary images for  $v = 1.52 \text{ mm/s}$  with  $t = 11.5 \text{ ms}$  and  $7.5 \text{ ms}$ , respectively. In the first image, a vortex dipole is located near the center region and clearly identified with its two distinctive density-depleted cores. On the other hand, in the second image that is taken with a short sweeping time  $t \sim \tau_v$ , a small crescent-shaped density dimple is observed with low visibility in the boundary region of the condensate. We interpret this density dimple as an incipient vortex dipole with a short intervortex distance  $d$ , which cannot be fully developed because of the short sweeping time. The incipient vortex dipole moves further away from the sweeping region because of higher propagation speed  $v_d = \hbar/m d$  for smaller  $d$  and its low visibility might be attributed to the blurring effect during the expansion before imaging.<sup>1</sup>

Compiling all the images containing a single vortex dipole for  $v = 1.52 \text{ mm/s}$ , in Fig. 5.6(c) we display the distribution of the vortex dipoles in the plane of ra-

---

<sup>1</sup>I would like to mention that it's just our speculation that the low visibility could originate from too short intervortex distance where the flow inside the vortex dipole region would affect the time of flight image. Exact numerical simulations on TOF image for a short vortex dipole should be needed, or in-situ imaging will be necessary.

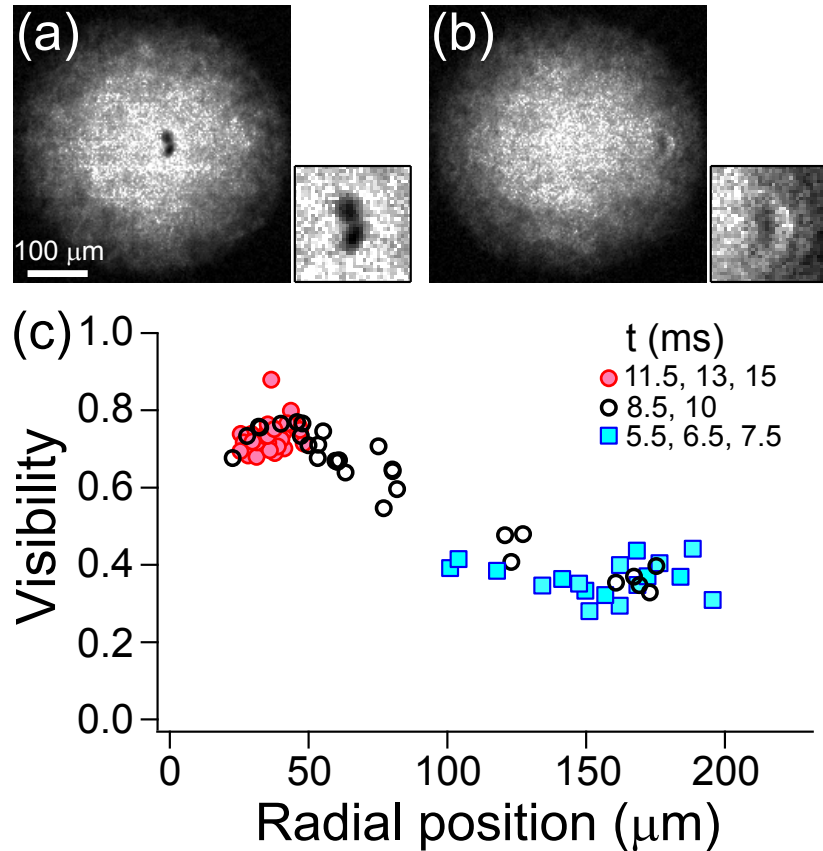


Figure 5.6: Formation of a vortex dipole. Images of BECs containing a vortex dipole, where  $V_0/\mu \approx 0.74$  and the sweeping times were (a)  $t = 11.5$  ms and (b)  $7.5$  ms at  $v = 1.52$  mm/s, respectively. For long  $t$ , the vortex dipole is clearly identified with its two vortex cores near the center region. For short  $t$ , it appears as a small density dimple with low visibility in the boundary region. The enlarged images of the vortex dipoles are presented on the right side of each image. (c) Vortex distribution in the plane of radial position and visibility, obtained from all the images containing a single vortex dipole in the experiment for  $v = 1.52$  mm/s [Fig. 5.2(a)].

dial position and visibility. The visibility was determined as  $1 - n_m/\bar{n}$ , where  $n_m$  is the density minimum value in the core region and  $\bar{n}$  is the average density in the surrounding area of the vortex dipole. The distribution shows a strong correlation between the visibility of the vortex dipole and its radial position, i.e., propagation speed, revealing the temporal development of the vortex dipole. From a rough estimation, taking into account the expansion time in the imaging sequence, we find that the propagation speed of the most incipient vortex dipole is comparable to the moving velocity of the obstacle, which is expected from the fact that the vortex dipole is shed from the moving obstacle. The condition of  $v_d = v$  gives the intervortex distance  $d = \hbar/mv \approx 4\xi$ .

When the sweeping time is not sufficiently long, although long enough to ensure generation of a vortex dipole, the speed of the generated vortex dipole is not reproducible. For example, when  $t = 8.5$  or  $10$  ms, the vortex generation probability is almost unity but the vortex dipole velocity widely scatters [open circles in Fig. 5.6(c)]. This is partially due to the uncertainty of the vortex emission time and also probably due to the finite dwelling time of the vortex dipole in the proximity of the laser beam, which might be estimated to be  $\Delta t = \sigma/2v$ . Therefore, for deterministic generation of a single vortex dipole, the sweeping time needs to be optimally chosen to have better stability in the vortex dipole velocity  $v_d$ . We examined the stability of  $v_d$  by putting an additional 100 ms hold time before releasing the trapping potential and measuring the change in the vortex position. In our experiment, the propagation speed of the vortex dipole was stable within 10% and its propagation direction was parallel within 15 degrees to the sweeping direction of the laser beam.

It needs to be mentioned that we cannot exclude the possibility that the crescent-shaped density dimple is a rarefaction pulse or a gray soliton, which

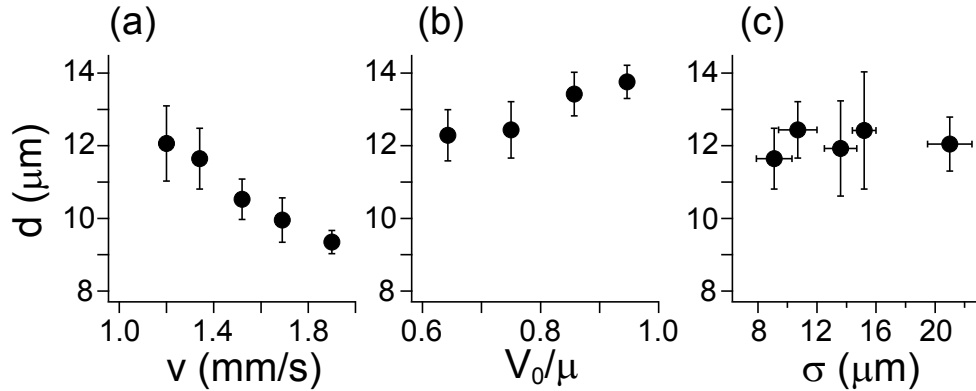


Figure 5.7: Dependence of the intervortex distance  $d$  on various sweeping parameters of the penetrable obstacle. (a)  $d$  versus  $v$ , where  $\sigma = 9.1(12) \mu\text{m}$  and  $V_0/\mu \approx 0.74$ . (b)  $d$  versus  $V_0/\mu$ , where  $\sigma = 10.7(13) \mu\text{m}$  and  $v = 1.25 \text{ mm/s}$ . (c)  $d$  versus  $\sigma$ , where  $V_0/\mu \approx 0.74$ . In (c),  $v$  was controlled to range from 1.08  $\text{mm/s}$  to 1.34  $\text{mm/s}$  due to the change of the critical velocity [10]. In each measurement, the sweeping time  $t$  was chosen to have  $d$  stable (see the text for detail).  $d$  was measured in the image and divided by the scaling factor of 2.1 for the expansion in the imaging sequence.

can also propagate with preserving its density profile with a nonzero density minimum [25, 29–32]. When the energy accumulated by the moving obstacle is not sufficient to generate a vortex dipole, it can possibly transform into lower energy excitation. The sudden stop of the moving obstacle might play a role in forming and stabilizing the excitation.

Finally, with a motivation to find a way to control the velocity of the vortex dipole, which will be very important for vortex-vortex interaction experiments, we investigate the dependence of the intervortex distance  $d$  on various parameters of the moving obstacle. Fig. 5.7 displays the measurement results of  $d$  as functions of the moving velocity  $v$ , the barrier height  $V_0/\mu$ , and the beam waist  $\sigma$  of the laser beam. We obtain  $d$  from the images assuming that relative positions of vortices are conserved after the imaging sequence. To check

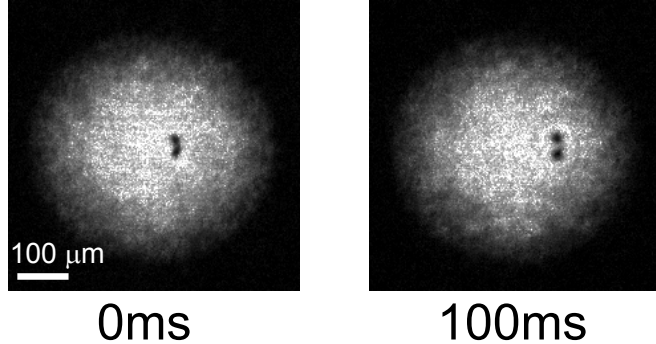


Figure 5.8: Propagation of a vortex dipole which is generated at  $v = 1.34 \text{ mm/s}$ ,  $V/\mu \approx 0.74$  and  $\sigma = 9.1(12) \mu\text{m}$ . We measure the velocity of the dipole from how long it moves during  $100 \text{ ms}$  and compare it with velocity calculated from  $\hbar/md$ , which comes out to be very similar.

whether the observed  $d$  is matched with real velocity of the vortex dipole, we let the vortex dipole to propagate for  $100 \text{ ms}$  after the generation of a vortex dipole [Fig. 5.8]. The experimental condition is  $v = 1.34 \text{ mm/s}$ ,  $\sigma = 9.1(12) \mu\text{m}$  and  $V/\mu \approx 0.74$ . We estimate the velocity of the dipole from how much distance it moves forward during  $100 \text{ ms}$ , which comes out to be  $0.21(3) \text{ mm/s}$ . A linear velocity of generated vortex dipole is calculated using  $\hbar/md = 0.24(2) \text{ mm/s}$ , where  $m$  is mass of the atom. There's a little underestimation on velocity estimated from the direct propagation of a vortex dipole and it is natural since the  $d$  becomes larger as the dipole goes towards the boundary of the condensate in harmonic trap. The result indicates that the measured  $d$  from images is quite accurate, compared to the real one.

We see that  $d$  slightly decreases with increasing  $v$ , suggesting one way to control  $v_d$  but in a limited range. Intriguingly,  $d$  is almost insensitive to  $V_0/\mu$  and  $\sigma$ . Considering the fact that the critical velocity  $v_c$  is significantly affected by the potential parameters of the obstacle [10], the observed weak dependence of  $d$  on

them is quite unexpected. In Ref. [30], vortex shedding from a moving attractive obstacle of  $V_0/\mu < 0$  was numerically studied, showing that  $d$  increases with higher  $v$ , which is opposite to our observation. Further theoretical studies are warranted to understand what determines the size of the vortex dipole when it is generated from a moving penetrable obstacle.

## 5.5 Demonstration of a vortex dipole-dipole collision

Due to periodic generation of vortex dipoles from a moving penetrable beam, by which exactly a single vortex dipole can be produced, we are able to generate a vortex dipole-dipole collision event employing two penetrable beams. We installed another Gaussian beam of almost same beam size and we translate both beams at the same time from the opposite side of the condensate by controlling two piezo-driven mirrors.

Fig. 5.9 shows the experimental images of head-on collisions of two vortex dipoles. After the collision each vortex changes its partner and new vortex pairs are formed which move orthogonal to initial directions. This new setup makes us possible to study vortex-phonon interaction by measuring the change between initial and final  $d$  after the collision, where  $d$  is an intervortex distance between a vortex and an antivortex, since the energy of vortices would be decreased and transformed into acoustic energy (sound wave) in the condensate after the collision [46]. Furthermore, By controlling the initial  $d$  one will eventually be able to figure out the condition at which two colliding vortex dipoles may disappear, i.e., vortex annihilation condition.

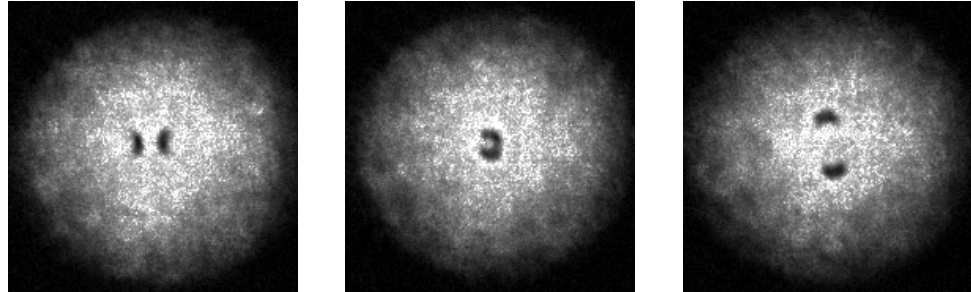


Figure 5.9: Collisions of two vortex dipoles heading towards each other. Each vortex dipole is generated from penetrable beams moving from the left and right side of the condensate. After the collision, new vortex dipoles are formed and propagate perpendicular to the original directions.

However, it comes out that a small stochastic deviation angle between beam movement direction and the vortex propagation direction hinders the deterministic occurrence of dipole-dipole collisions. Such deviation would be due to jittering of the moving obstacles or the optical dipole trap. These technical imperfections should be fixed first to systematically study vortex-phonon interaction. One more thing is that we should find a way to freely control the intervortex distance  $d$  (to make it much smaller) which might require beam size comparable to a few healing length  $\xi$ .

## 5.6 Possibility of a self-annihilation of a single vortex dipole?

Different from the above case of two colliding vortex dipoles, there is another simple but serious question on a vortex pair annihilation; ‘can a single vortex itself annihilate in a certain condition?’ To explore this question, using the deterministic generation method, we create a vortex dipole far away from the center

of the condensate, which results in a much tighter vortex dipole as it propagates to the center in a harmonic trap [Fig. 5.10(a)]. Interestingly, we observe very low visibility excitation which might indicate that a generated vortex dipole already would evolve into a grey soliton (rarefaction pulse). As it propagates to the left boundary, however, it clearly separates into a vortex and antivortex which are orbiting the condensate very near the boundary [Fig. 5.10(b)]. One interesting interpretation on this observation is that the vortex dipole probably be annihilated at the center so its visibility becomes lowered, and revives as it goes to the boundary [29]. Nevertheless, such scenario is hard to be firmly confirmed since it might simply be a very tight vortex dipole.

Varying the initial intervortex distance and watching the change of lifetime of the vortex dipole will give useful information on the self-annihilation of the dipole [33]. If a lifetime of single vortex dipole is mainly determined by pair annihilation event inside the condensate [33], one might observe abrupt change in decay time of a vortex dipole. Or increasing the temperature of the system will show similar feature. A trajectory of the vortex dipole changes as it orbits around the condensate at nonzero temperature due to the dissipation (mutual friction acting on the vortices) [Figs. 5.10(c),(d)]. When the intervortex distance becomes comparable to  $\xi$  at the center of the condensate, it would be annihilated. It means that for a given initial vortex dipole configuration, the vortex dipole lifetime could be very sensitive to the temperature. Though one may wonders about the possibility for a vortex and an antivortex to disappear at the boundary rather than by self-annihilation, which should be checked, such experiment will be helpful to understand decay of a vortex dipole which is somewhat different from the case of ch. 3.

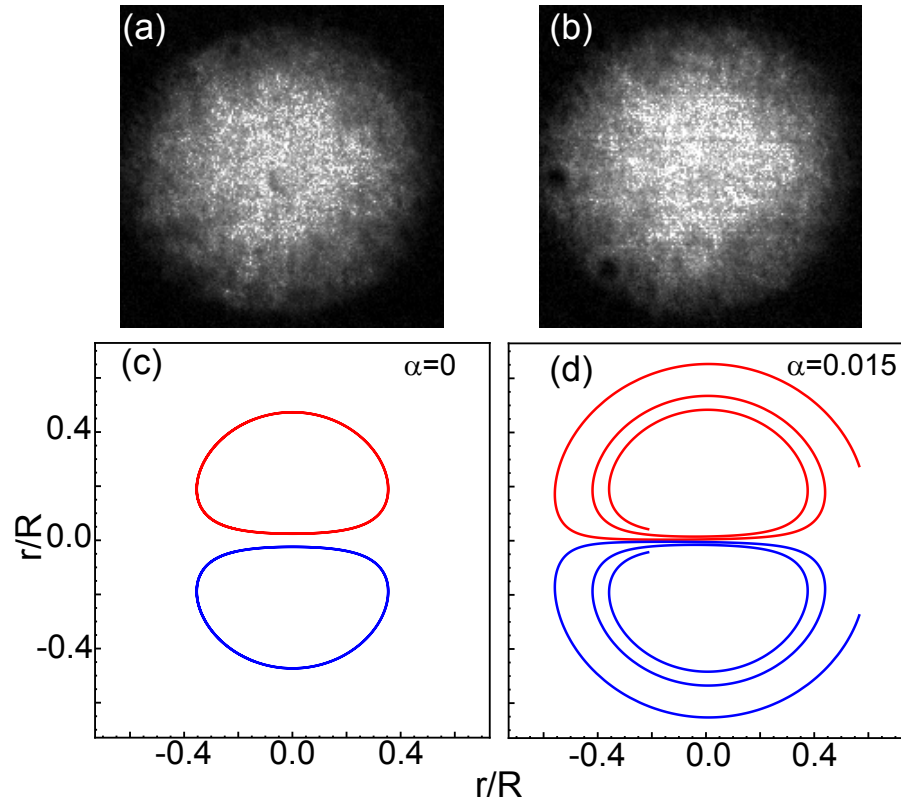


Figure 5.10: (a) A low visible excitation observed in the condensate center. We cannot distinguish it from a vortex dipole of very short distance to a rarefaction pulse. In this case, the Gaussian obstacle is translated from near the right side boundary of the condensate. (b) A vortex dipole is observed which is very close to the boundary. (c),(d) each indicates a simulation result of trajectories of a vortex dipole for mutual friction coefficient  $\alpha = 0$  and  $\alpha = 0.015$ , respectively.  $R$  is radius of the condensate. Details of the simulations are as same as that represented in ch. 3. For a same initial vortex dipole configuration, its decay time may show abrupt behavior on temperature of the system because of annihilation condition.

## 5.7 Vortex dipoles vs clustered vortex street

Motivated by the findings that vortex shedding patterns seem to be very different depending on the nature of the obstacles [Fig. 5.5], I change the optical setup and piezo actuator to increase the moving distance of the obstacle beam  $L$  to be  $115 \mu\text{m}^2$ , which is almost half the size of the condensate. Fig. 5.11 represents the results of vortex shedding for such long movement  $L$ . As already informed in the above text (see introduction part), since topologies of impenetrable and penetrable beam are totally different, the vortex creation and emission procedure could also be different. As shown in the left image of Fig. 5.11, moving penetrable beam generates vortex dipoles periodically. In stark contrast, we observe the 6 clustered vortices of charge-2 from impenetrable beam (right image of Fig. 5.11), which is hardly observable from penetrable beam case.

Unfortunately, such a beautiful and clear image of von Kármán street like Fig. 5.11 is rarely observed. The reason might be experimental imperfections from beam jittering, including both an optical trapping and a shedding beam, combined with the nature of shedding dynamics itself. One may expect that small instability of the beams would induce a relative motion between the condensate which will immediately change the patterns of generated vortices. Moreover, as theoretical calculation predicts that experimental parameter spaces for such charge-2 von Kármán street may not be broad [24] enough, small perturbations to experiments would make it impossible to detect von Kármán

---

<sup>2</sup>Mad city labs, PZT3, max displacement:  $17.5 \mu\text{m}$ . Translation distance  $L$  is determined by a total amount of ‘angle’ changed, due to piezo actuator, before the final lens which focuses the beam on the BEC plane. Since we use final lens of  $f = 100 \text{ mm}$  and the changed angle is roughly  $17.5 \mu\text{m}/30 \text{ mm} \times 5/3$ , where  $30 \text{ mm}$  is the mirror mount size and  $5/3$  corresponds to inverse number of magnification of telescope, we can approximately estimate  $L \approx 17.5 \times 50/9 \approx 97 \mu\text{m}$ . This is quite similar to real one.

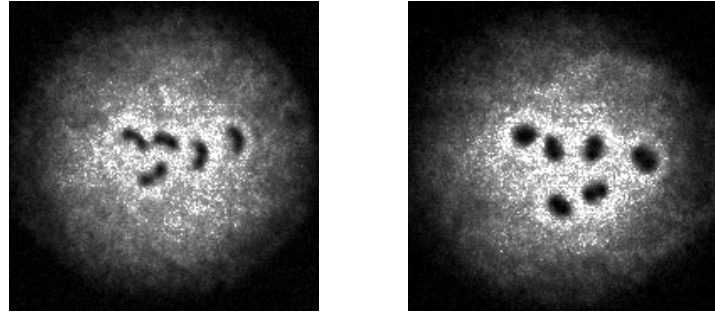


Figure 5.11: Two distinct vortex shedding patterns depending on whether the obstacle beam is penetrable ( $V_0 < \mu$ , left) or impenetrable ( $V_0 > \mu$ , right). As noticed in the text, vortex dipoles are periodically released from penetrable beam. However, for impenetrable beam, we confirmed that vortex streets of charge-2, i.e., pairs of corotating vortices, could be generated for some experimental parameters within our setup.

street repeatedly.

When the velocity  $v$  becomes larger, turbulent shedding seems to occur which is very similar to that of classical turbulence pattern (Fig. 5.12). Clusters of like-signed vortices (more than 3 or 4) are often observed when  $v$  is sufficiently high. These experimental results may indicate that vortex shedding patterns would be sensitive to the conditions of moving impenetrable obstacle, like its velocity  $v$  and size, which is predicted from recent numerical simulation [24]. These preliminary experimental results from impenetrable beam are very interesting and seemingly show similar behavior of classical fluid past a hard cylinder. It will be wonderful to study shedding dynamics from impenetrable beam which may possess “Superfluid Reynolds number” as predicted by ref. [24].

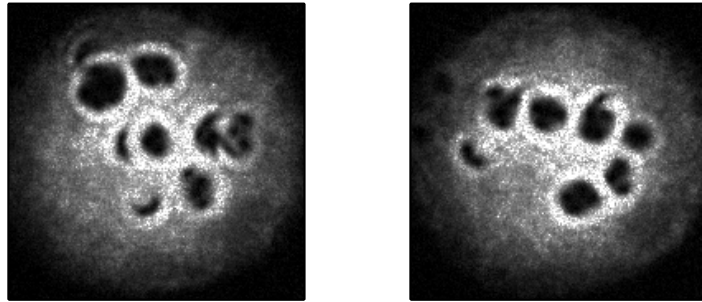


Figure 5.12: Clustered vortices are highly producible at higher  $v$  for impenetrable beam.  $v$  is larger than that of Fig 5.11. Two images are obtained at the same experimental conditions. These images are very similar to classical turbulent wake where very large and aggregated vortices are generated. Such patterns are hardly detected with penetrable beam.

## 5.8 Summary and Outlook

We investigated vortex shedding dynamics with a moving penetrable obstacle in a highly oblate BEC. We observed periodic shedding of vortex dipoles and found the linear dependence of the vortex shedding frequency on the moving velocity of the obstacle above the critical velocity. In addition, we demonstrated deterministic generation of a single vortex dipole by applying a short linear sweep of the penetrable laser beam. This vortex generation method is expected to provide new opportunities for further controlled experiments on vortex dynamics. For example, as suggested in Ref. [30], if two laser beams are employed to generate two vortex dipoles separately at different positions in a condensate, it would be possible to investigate collision dynamics of vortex dipoles in a controlled manner. Dipole-dipole collisions [32] are particularly interesting in that vortex pair annihilation may occur during the collision. Vortex pair annihilation is one of the key issues in the study of 2D quantum turbulence [34–43]. Many aspects of the pair annihilation process [44,45], such as the roles of vortex-phonon inter-

actions [46–48], and thermal dissipation [49], have never been directly addressed in experiments.

Besides, our introductory experimental results with larger  $L$  reveal very interesting shedding dynamics from impenetrable beam. Deeper experimental investigations on von Kármán street and turbulence vortex shedding will provide useful informations on this paradigmatic problem in a superfluid.

# Bibliography

- [1] A. L. Fetter, Rev. Mod. Phys. **81**, 647 (2009).
- [2] V. L. Berezinskii, Sov. Phys. JETP. **34**, 610 (1972).
- [3] J. M. Kosterlitz and D. J. Thouless, J. Phys. C **6**, 1181 (1973); J. M. Kosterlitz *ibid* **7**, 1046 (1974).
- [4] T. W. B. Kibble, J. Phys. A **9**, 1387 (1976).
- [5] W. H. Zurek, Nature (London) **317**, 505 (1985).
- [6] M. Tsubota, M. Kobayashi, and H. Takeuchi, Phys. Rep. **522**, 191 (2013).
- [7] A. C. White, B. P. Anderson, and V. S. Bagnato, Proc. Natl. Acad. Sci. U.S.A. **111**, 4719 (2014).
- [8] S. Inouye, S. Gupta, T. Rosenband, A. P. Chikkatur, A. Görlitz, T. L. Gustavson, A. E Leanhardt, D. E. Pritchard and W. Ketterle, Phys. Rev. Lett. **87**, 080402 (2001).
- [9] T. W. Neely, E. C. Samson, A. S. Bradley, M. J. Davis, and B. P. Anderson, Phys. Rev. Lett. **104**, 160401 (2010).

- [10] W. J. Kwon, G. Moon, S. W. Seo, and Y. Shin, Phys. Rev. A **91**, 053615 (2015).
- [11] C. N. Weiler, T. W. Neely, D. R. Scherer, A. S. Bradley, M. J. Davis, and B. P. Anderson, Nature **455**, 948 (2008).
- [12] D. V. Freilich, D. M. Bianchi, A. M. Kaufman, T. K. Langin, and D. S. Hall, Science **329**, 1182 (2010).
- [13] J. Choi, S. W. Seo, and Y. Shin, Phys. Rev. Lett. **110**, 175302 (2013).
- [14] S. Middelkamp, P. J. Torres, P. G. Kevrekidis, D. J. Frantzeskakis, R. Carretero-González, P. Schmelcher, D.V. Freilich, and D. S. Hall, Phys. Rev. A **84**, 011605(R) (2011).
- [15] W. J. Kwon, G. Moon, J. Choi, S. W. Seo, and Y. Shin, Phys. Rev. A **90**, 063627 (2014).
- [16] T. Frisch, Y. Pomeau, and S. Rica, Phys. Rev. Lett. **69**, 1644 (1992).
- [17] B. Jackson, J. F. McCann, and C. S. Adams, Phys. Rev. Lett. **80**, 3903 (1998).
- [18] T. Winiecki, B. Jackson, J. F. McCann, and C. S. Adams, J. Phys. B: At. Mol. Opt. Phys. **33**, 4069 (2000).
- [19] T. Winiecki, J. F. McCann, and C. S. Adams, Phys. Rev. Lett. **82**, 5186 (1999).
- [20] B. Jackson, J. F. McCann, and C. S. Adams, Phys. Rev. A **61**, 051603(R) (2000).

- [21] K. Sasaki, N. Suzuki, and H. Saito, Phys. Rev. Lett. **104**, 150404 (2010).
- [22] T. Kadokura, J. Yoshida, and H. Saito, Phys. Rev. A **90**, 013612 (2014).
- [23] M. T. Reeves, B. P. Anderson, and A. S. Bradley, Phys. Rev. A **86**, 053621 (2012).
- [24] M. T. Reeves, T. P. Billam, B. P. Anderson, and A. S. Bradley, Phys. Rev. Lett. **114**, 155302 (2015).
- [25] K. Fujimoto and M. Tsubota, Phys. Rev. A **83**, 053609 (2011).
- [26] There is a theoretically subtle issue on whether the vortex nucleation period is finite [19] or diverges [25] as  $v$  converges to  $v_c$ .
- [27] N. G. Berloff and P. H. Roberts, J. Phys. A: Math. Gen. **33**, 4025 (2000).
- [28] C. Nore, M. E. Brachet, and S. Fauve, Physica D **65**, 154 (1993).
- [29] G. Huang, V. A. Makarov, and M. G. Velarde, Phys. Rev. A **67**, 023604 (2003).
- [30] T. Aioi, T. Kadokura, T. Kishimoto and H. Saito, Phys. Rev X **1**, 021003 (2011).
- [31] F. Pinsker and N. G. Berloff, Phys. Rev. A **89**, 053605 (2014).
- [32] L. A. Smirnov and A. I. Smirnov, Phys. Rev. A **92**, 013636 (2015).
- [33] S. J. Rooney, P. B. Blakie, B. P. Anderson, and A. S. Bradley, Phys. Rev. A **84**, 023637 (2011).
- [34] S. Nazarenko, and M. Onorato, J. Low Temp. Phys. **146**, 31 (2007).

- [35] T.-L. Horng, C.-H. Hsueh, S.-W. Su, Y.-M. Kao, and S.-C. Gou, Phys. Rev. A **80**, 023618 (2009).
- [36] R. Numasato, M. Tsubota, and V. S. L'vov, Phys. Rev. A **81**, 063630 (2010).
- [37] J. Schole, B. Nowak, and T. Gasenzer, Phys. Rev. A **86**, 013624 (2012).
- [38] P. M. Chesler, H. Liu, and A. Adams, Science **341**, 368 (2013).
- [39] T. Simula, M. J. Davis, and K. Helmerson, Phys. Rev. Lett. **113**, 165302 (2014).
- [40] G. W. Stagg, A. J. Allen, N. G. Parker, and C. F. Barenghi, Phys. Rev. A **91**, 013612 (2015).
- [41] P. M. Chesler and A. Lucas, arXiv:1411.2610.
- [42] Y. Du, C. Niu, Y. Tian, and H. Zhang, arXiv:1412.8417.
- [43] T. P. Billam, M. T. Reeves, and A. S. Bradley, Phys. Rev. A **91**, 023615 (2015).
- [44] C. Rorai, K. R. Sreenivasan, and M. E. Fisher, Phys. Rev. B **88**, 134522 (2013).
- [45] S. Prabhakar, R. P. Singh, S. Gautam, and D. Angom, J. Phys. B: At. Mol. Opt. Phys. **46**, 125302 (2013).
- [46] J. Ruostekoski, and Z. Dutton, Phys. Rev. A **72**, 063626 (2005).
- [47] K. Suthar, A. Roy and D. Angom, J. Phys. B: At. Mol. Opt. Phys. **47**, 135301 (2014).

- [48] A. Lucas, and P. Surówka, Phys. Rev. A **90**, 053617 (2014).
- [49] A. J. Allen, S. Zuccher, M. Caliari, N. P. Proukakis, N. G. Parker, and C. F. Barenghi, Phys. Rev. A **90**, 013601 (2014).

# Chapter 6

## Conclusions and Outlooks

This dissertation describes our works on quantized vortex dynamics in highly oblate geometry. Our study on decaying turbulence suggests the possibility of vortex pair annihilation in a BEC. Even our interpretation is not exact due to lack of any theoretical backgrounds on such experimental conditions at that time, I believe that our work could be a nice testbed to be compared with newly proposed theoretical (or experimental) studies on 2D superfluid turbulence. Moreover, experiments on vortex shedding dynamics including measurements on critical velocity for creating vortices will fill up the missing part in vortex studies, which has long been awaited.

Through the studies on vortex shedding and quantum turbulence, we are able to contribute a little to the areas of 2D quantum vortex and quantum turbulence. What will be the next goal? What are remained in vortex dynamics?

Vortex dipole-dipole collision experiment will help us to understand more deeply on vortex-phonon interaction and vortex pair annihilation, which are fundamental elements in quantum vortex phenomena in a BEC. Extension to 3D case, where kelvin wave excitations and vortex reconnection are favorable,

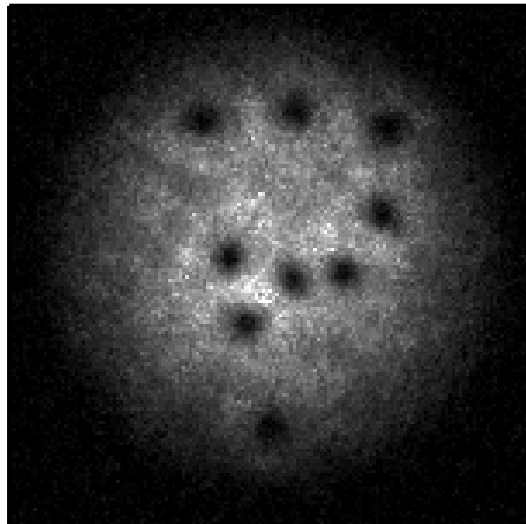


Figure 6.1: Question mark made by vortices during relaxation of turbulence.

will also be very important though it needs some experimental breakthroughs. In addition, experiments on vortex shedding with moving “impenetrable beam” will give us new insight, especially on shedding patterns depending on velocity of the moving obstacle. Experimental verifications on Von Kármán vortex street and cluttered vortex emission for turbulent regime, which is totally different from our previous report on periodic shedding of vortex dipoles from a penetrable beam, will be invaluable. Lastly, revisiting the issues on 2D quantum turbulence and inverse energy cascade with more rigorous experimental setups, like uniform potential or real time imaging technique, should be worthy. In particular, real time observation of how vortices disappear in the condensate will substantiate the issues of vortex pair annihilation.

# Appendices

# Appendix A

## Li 교체 진공작업

1. 모든 것을 시작하기에 앞서 모든 진공 압력을 읽는 기기(gauge)를 꾌도록 한다.
2. turbo pump와 oven쪽 angle valve사이의 flange를 연결한 후 roughing pump 와 turbo pump를 가동시켜서 vacuum이 잘 내려가는지 확인. (roughing을 먼저 가동하고 곧바로 turbo를 킨다. 그리고는 turbo와 roughing 사이의 valve를 열어주자. turbo가 꺼져있으면 turbo venting line은 open상태임에 주의.)
3. Li 세척 (mineral oil에 담궈져 있던 Li을 사용할 때)  
airbag에 Li이 담긴 mineral oil 용기와 pentane 용액을 담은 비커를 준비 한다. 비커는 2개를 준비해서 각 리튬 고체를 2번 이상 씻을 수 있게 하자. airbag에는 argon기체로 차 있도록 한다. 비커안에 몇 번 담갔다가 빼면 곧 바로 자연적으로 마르는 것이 보인다. 그 다음 Li을 가위로 잘라준다. Li의 표면은 산화, 또는 질소와 반응한 상태이기 때문에 Li을 잘라줘서 깨끗한 단면이 보이는 게 중요하다. (우리 경험에 따르면 단면이 보이도록 자르는 과정을 거치지 않고 그냥 oven에 넣으면 300 ~ 400도로 가열해도 리튬

원자빔이 전혀 나오지 않았다.) 그 다음 이 것을 cup에 넣는다.

4. argon gas에 연결된 호스를 turbo pump venting line에 연결. – > regulator 를 1bar로 설정.
5. turbo와 roughing pump 연결 부위를 잠근 다음 turbo pump off. – > 2,3 분 후에 슈우웅 하는 소리와 함께 venting 시작됨. argon의 angle valve 부분까지를 채우게 될 것임.
6. oven angle valve를 서서히 열어준다. argon의 oven을 채우게 됨.
7. Li cup에 쪼여진 볼트를 풀어준다. – > 다 풀고 나면 argon의 새어나오는 바람이 느껴짐.
8. 새 cup에 세척한 Li을 넣고 장착 (Lithium의 너무 오래동안 공기중에 노출 되어 있으면 가위로 잘른 단면의 색이 변하므로 머뭇거리지 않도록). 장착이 완료되면 turbo venting line으로 유입되는 argon을 차단시킨다.
9. turbo와 roughing 사이의 연결부분을 열어준다. turbo를 켜 준다. turbo를 켜면 venting line은 자동으로 닫힌다. (roughing은 지금 이 모든 과정에서 끄지 않았었음에 유의.)

\*\* 현재 실험실에 보관하고 있는 lithium은 아주 깨끗이 정제과정을 거친 것이다. Cambridge Isotope사의 mineral oil에 담긴 리튬을 공급받은 후 이를 Ames Lab에서 표면을 깨끗이하고 argon ampule로 만들어주었다. (Cambridge Isotope 사의 한국 대리점 (주)티엔제이테크: tnjtech.co.kr에 의뢰하였다). 그리고 sigma aldrich사의 atmosbag 사용. mineral oil에 담긴 lithium 덩어리는 aldrich사에서도 판매하며 연구실에 남아있다.

## **Appendix B**

### **Offset lock for ${}^6\text{Li}$ imaging laser**

The following represents schematic of offset lock for  ${}^6\text{Li}$  imaging laser which is necessary to image the atomic cloud when strong magnetic field is applied so that the detuning should be as large as  $\sim \text{GHz}$ .

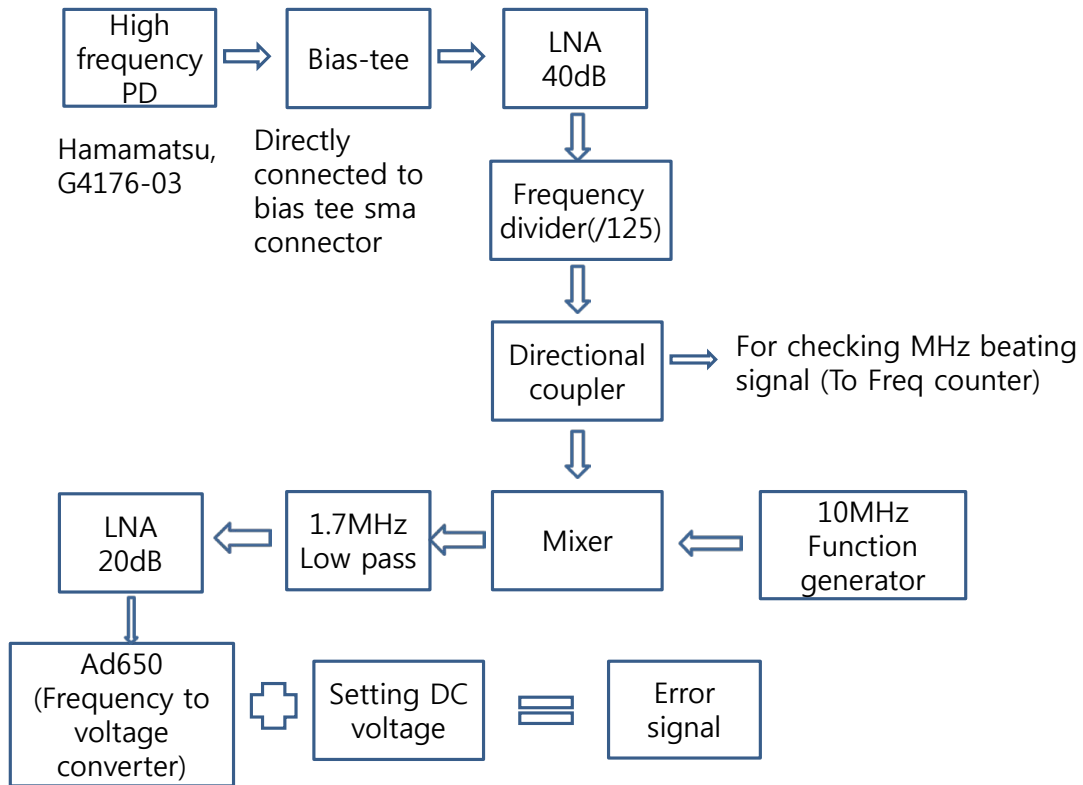


Figure B.1: Offset lock scheme for  ${}^6\text{Li}$  imaging laser. Locking frequency is controlled by 10 MHz function generator. In my experience, beam alignment to highfrequency PD, whose detector size is very small, is critical to quality of locking of the laser. If the error signal is not that good, redoing the beam alignment will help you.

## Appendix C

# Measuring trapping frequency with parametric resonance

We use parametric resonance heating phenomenon to measure a trapping frequency of an optical dipole trap, especially for obtaining z-direction trap frequency which makes a condensate very oblate. Whereas radial trap frequencies of x and y direction are measured by dipole oscillation of a condensate.

A harmonic oscillator, whose frequency  $\omega_0$  is sinusoidally modulated with frequency  $\omega_{mod}$ , i.e.,  $\omega(t) = \omega_0^2(1 + \epsilon \sin(\omega_{mod}t))$ , exhibits resonance at

$$\omega_{mod} = 2\omega_0/n, \quad (\text{C.1})$$

where  $n$  is a positive integer. Since trapping frequency of optical dipole trap  $w_0^2 \propto P$ , where  $P$  is beam power, we can easily parametrically drive the dipole trap by oscillating the beam power  $P$ .

Experimental results for obtaining axial trapping frequency of optical trap is represented in fig. C.1. At resonance frequency, a condensate is heated so that condensate atom number is reduced. We extract  $2\omega_0$  from Gaussian

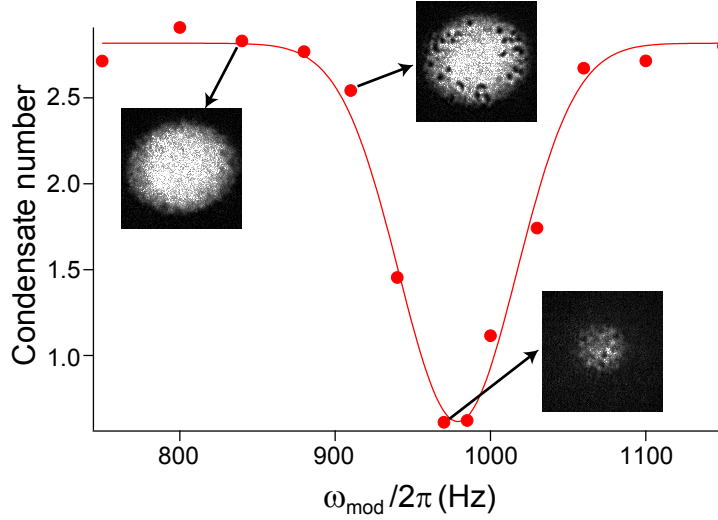


Figure C.1: Measurement of axial trapping frequency of an oblate trap with parametric resonance. The resonance frequency in the figure is at twice the trapping frequency of the trap.

fitting (red solid line). One very interesting observation is that vortices are generated by this parametric resonance phenomenon. That is, by generating vortices (including both signs) at the boundary of the condensate, the condensate is heated. We find that by reducing the time duration or the amplitude for parametric driving, one can observe vortices near the boundary around the resonance frequency, without the atom loss. And the number of created vortices is the largest at resonance frequency. This is another method to measure trap frequency precisely.

It is amazing that axial oscillation of trap generates vortices in the radial plane. However, we do not have any clue on this issue yet. Is this related to vortex-antivortex pair in two dimensional system? or just characteristics of highly oblate condensate? Further experimental verification on this issue will be invaluable.

## 초 록

양자 소용돌이는 (quantized vortex) 초유체에서 가장 근원적인 여기 현상의 하나로 보즈-아인슈타인 응집체가 (Bose-Einstein condensate) 처음으로 만들어진 직후부터 아주 오랫동안 연구되어 왔다. 1998년도에 처음으로 BEC에서의 소용돌이가 관측되었고 소용돌이의 형성과정, 소용돌이 격자구조 등등이 지속적으로 관심을 끌어왔다. 한편으로는 이러한 오랜 연구 역사덕분에 양자 소용돌이에 대한 관심도는 2000년대 초중반에 비해 많이 줄어든 점도 사실이다. 하지만 아직도 흥미롭고도 미지의 영역으로 남아있는 부분이 상당히 있으며 그것 중의 하나가 바로 양자 난류(turbulence)이다.

양자 난류는 헬륨 초유체가 발견된 이후부터 줄곧 물리학자들이 매진해온 연구 분야이다. 특히 이론적으로 많은 연구가 진행되었는데, 양자 소용돌이 선들(vortex lines)의 엉킴(tangle)과 그 붕괴과정에서 수반되는 소용돌이 재결합(reconnection)은 양자 유체에서 일어나는 흥미로운 현상으로써 아직도 열려있는 문제이다. BEC 초유체는 헬륨에 비해서 훨씬 더 조절성이 좋고 또 2차원 동역학을 다루기에 쉬운 장점등이 있기 때문에 최근들어서 난류 연구의 좋은 수단으로 인식되기 시작했다. 우리는 납작한 BEC를 통해 2차원 양자 난류 현상을 구현하고 그 붕괴과정을 실험적으로 살펴보았으며 그 과정을 소용돌이 쌍소멸로 해석하였다. 또한 양자 난류 붕괴는 온도에 크게 영향을 받는다는 사실을 발견하였다.

이러한 발견은 자연스럽게 온도에 따른 양자 소용돌이의 움직임에 대한 연구로 이어지게 되었다. 유한한 온도를 갖는 초유체에서 양자 소용돌이는 마찰력을 느끼게 되는데 이는 초유체와 비초유체 성분간의(thermal component) 상호작용에 의한 것이다. 이를 상호 마찰력(mutual friction)이라고 말한다. 우리는 BEC에서 두개의 같은 방향으로 회전하는 소용돌이를 생성한 다음, 그것들의 시간에 따른 운동을 측정함으로써 상호 마찰력의 계수  $\alpha$ 를 처음으로 제시할 수

있었다. 또한  $\alpha$ 가 온도에 지속적으로 증가한다는 사실도 밝혀낼 수 있었다.

끝으로, 우리는 초유체에서의 소용돌이 방출 (vortex shedding) 현상에 대한 연구를 진행하게 된다. BEC에 척력을 갖는 Gaussian 빔을 장애물로 설치를 하고 이를 임계속도 이상으로 움직이면 소용돌이가 방출되기 시작한다. 이는 초유체에서 가능한 아주 교과서적인 실험의 하나이지만 체계적인 실험 결과가 부족한 상태였다. 이에 우리는 임계속도와 장애물 사이의 관계, 방출되는 소용돌이의 특성에 집중해서 실험을 진행하였다. 장애물의 높이  $V_0$ 와 빔 크기  $\sigma$ 를 변화시켜 가면서 임계속도  $v_c$ 를 측정하였으며  $V_0 \gg \mu$ 일 때 ( $\mu$ 는 BEC의 chemical potential)  $\sigma$ 가 커짐에 따라  $v_c$ 가 점점 작아짐을 알아냈다. 모든 실험 결과는 Gaussian 빔의 경계 모양새를 고려하면 정성적으로 이해 할 수 있음을 제시하였다. 나아가서, 우리는 소용돌이가 생겨나는 특성이 빔의 특성에 따라 다름을 발견하였다.  $V_0$ 의 크기가  $\mu$ 보다 크면 소용돌이 방출 패턴이 불규칙하고 작으면 소용돌이 쌍(vortex dipole)이 주기적으로 방출됨을 관측하였다. 그리고 이 주기성을 활용하면 소용돌이 쌍을 정확히 하나만 만들어낼 수 있다. 이를 응용하면 소용돌이 쌍과 쌍의 충돌이 실험이 가능해지는데 이는 소용돌이 쌍소멸과 소용돌이-포논(phonon) 상호작용 등을 연구할 수 있는 굉장히 흥미로운 실험 셋업이 될 수 있을 것이다.

**주요어 :** 보즈-아인슈타인 응집현상, 초유체, 양자 소용돌이 , 양자 난류,  
소용돌이 쌍소멸, 상호 마찰, 소용돌이 방출, 임계 속도.

**학 번 :** 2010-20357